High-resolution Finite Volume Methods for Extracorporeal Shock Wave Therapy

Kirsten Meri Fagnan

A dissertation submitted in partial fulfillment
of the requirements for the degree of

Doctor of Philosophy

University of Washington

2010

Program Authorized to Offer Degree: Applied Mathematics

University of Washington
Graduate School

This is to certify that I have examined this copy of a doctoral dissertation by

Kirsten Meri Fagnan

and have found that it is complete and satisfactory in all respects,
and that any and all revisions required by the final
examining committee have been made.

Chair of the Supervisory Committee:

_____

Randall J. LeVeque

Reading Committee:

_____

J. Nathan Kutz

_____

Thomas J. Matula

Date: _____

In presenting this dissertation in partial fulfillment of the requirements for the doctoral degree at the University of Washington, I agree that the Library shall make its copies freely available for inspection. I further agree that extensive copying of this dissertation is allowable only for scholarly purposes, consistent with "fair use" as prescribed in the U.S. Copyright Law. Requests for copying or reproduction of this dissertation may be referred to Proquest Information and Learning, 300 North Zeeb Road, Ann Arbor, MI 48106-1346, 1-800-521-0600, or to the author.

Signature_____

Date_____

University of Washington

Abstract

High-resolution Finite Volume Methods for Extracorporeal Shock Wave Therapy

Kirsten Meri Fagnan

Chair of the Supervisory Committee:
Professor Randall J. LeVeque
Applied Mathematics

Extracorporeal Shock Wave Therapy (ESWT) is a noninvasive treatment for bone fractures that fail to heal, necrotic wounds and strained tendons. It is similar to lithotripsy, a non-surgical treatment for kidney stones. In this treatment a shock wave is generated in water and then focused using an acoustic lens or reflector so the energy of the wave is concentrated in a small region. This technique has been used since the 1980's, but the underlying biological mechanisms are not well understood. In this thesis we have computationally investigated shock wave propagation in ESWT by solving a Lagrangian form of the isentropic Euler equations in the fluid and linear elasticity in the bone using high-resolution finite volume methods. We have also incorporated tissue-like materials into the model through variation of the parameters in the Tait equation of state.

This work differs from prior modeling of ESWT in that we are solving a full three-dimensional system of equations so we can handle complex bone geometries, and our formulation of the equations enables us to consider shear stresses generated within the bone. In this thesis I provide background information on shock wave therapy and prior modeling efforts. I have given details on the set of equations we use to model the wave propagation, as well as results validating this approach.

TABLE OF CONTENTS

LIST OF FIGURES

GLOSSARY

ESWT: Extracorporeal shock wave therapy - noninvasive treatment for tendinopathies, nonunions and calcifications.

ESWL: Extracorporeal shock wave lithotripsy - noninvasive treatment for the pulverization of kidney stones.

F1: The first focus of the ellipsoid in a model of an electrohydraulic lithotripter where the spark plug source sets off the explosion.

F2: The second focus of the ellipsoid in a model of an electrohydraulic lithotripter where the object being treated is placed in order to maximize energy deposition in the desired location.

HO: Heterotopic ossification, growth of bone-like material in soft tissue.

NONUNION: Bone fracture that fails to heal in six months and will not heal without surgical or other intervention.

BIREFRINGENCE: is the decomposition of a ray of light into two rays.

PHOTOELASTIC: Property of some materials where the propagation path of light is altered by stresses that make the material birefringent.

ISOCHROMATIC FRINGES: Lines of maximum principal stress difference in a photoelastic image, isolated when a circular polariscope is used.

ISOCLINIC FRINGES: A loci of points of constant inclination of the principal axes of refraction, visible when birefringent materials are studied with a linear polariscope.

AMR: Adaptive mesh refinement - algorithm where multiple grids with different levels of refinement are used in the same computational domain allowing for the use of a fine grid only in locations where it is necessary.

ACKNOWLEDGMENTS

First, I wish to express my sincere thanks to my advisor, Randy LeVeque, as well as my committee members Thomas J. Matula, Kenneth Bube, Randall Ching and Nathan Kutz. Their encouragement and guidance was invaluable in the completion of this work. I am also appreciative of the work done by Michael Bailey, Brian MacConaghy and Juan Tu of the Center for Industrial and Medical Ultrasound at the University of Washington, for generating the laboratory data used for validation of this work. I would also like to thank Mark Ganter for helping us build numerical and physical models of the same CT scan data for the validation of our results. Also, the work on heterotopic ossifications would not have been possible without the help and data provided by Michael Chang.

Finally, I am grateful to the University of Washington, the Applied Mathematics Department, the ARCS Foundation, National Science Foundation, the Marie Curie Research Training Network and the National Institutes of Health for their support during my graduate school career. This research was supported in part by NIH Grant 5R01AR53652-2, DOE grant DE-FC02-01ER25474, and NSF Grants DMS-9810726, DMS-0106511, and DMS-0609661.

DEDICATION

To my family and friends.

Chapter 1

INTRODUCTION

The work presented in this thesis arose from discussions with Dr. Thomas J. Matula and Dr. Michael Bailey from the Applied Physics Laboratory at the University of Washington. Extracorporeal shock wave lithotripsy (ESWL) was introduced in the the 1980's for the treatment of urinary stones, and was soon followed by extracorporeal shock wave therapy (ESWT) for musculoskeletal conditions. Dr. Matula and Dr. Bailey had been conducting experiments in order to better understand the mechanisms involved in stone comminution during ESWL, as well as exploring the role of cavitation, the formation and bursting of gas bubbles, in both treatments. In lithotripsy, or shock wave therapy, a shock wave is generated, for example by an explosion in water, focused through the use of an ellipsoid reflector and it then propagates into the body where, ideally, maximal energy is deposited at the treatment site. In order to better understand the treatment, it is important to develop a methodology for studying the propagation of the shock wave through water and biological materials, as well as how the shock wave interacts with objects at the focus (F2). This has been the focus of much research over the past 30 years, and our recent work contributes to that knowledge base.

What is clear from experimentation is the importance of shear stress in the comminution of kidney stones[72], growth of endothelial cells necessary for angiogenesis[62], and osteogenesis [41]. It has also been hypothesized that there is a cumulative shearing mechanism responsible for tissue damage in ESWL [31]. It is therefore extremely important that shear stresses be included in any mathematical modeling where we hope to better understand the interaction of the pressure wave with bone or soft tissue. Most prior modeling efforts have been limited to the Euler equations with various equations of state[7, 43] or the KZK equation [3], which do not include shear stresses. We have utilized the fact that displacements of the fluid and solid are small, in order to write the equations for the fluid and solid dynamics in a Lagrangian frame. This has enabled us to investigate not only the propagation of the pressure wave, but the generation of shear stress within and at the surface of the bone.

The numerical methods used in this thesis are implemented with the high resolution wave propagation algorithm as formulated by LeVeque [51]. These methods are Godunov-type finite volume methods that utilize the solution of Riemann problems to determine the numerical update at each time step. Instead of using the solution of the Riemann problem to determine the cell interface fluxes directly, in the wave propagation algorithm, the numerical solution is updated by direct re-averaging of the waves arising in the solution to the Riemann problem onto adjacent grid cells. This method is applicable to hyperbolic systems of equations including linear elasticity, nonlinear elasticity and the Euler equations, i.e. the components of our model for ESWT. In order to solve the equations in a reasonable amount of time while capturing the steepening of the shock and interaction with complex bone geometries, we utilize the adaptive mesh refinement routines available in the AMRCLAW and ChomboClaw software packages [27, 48, 10]. Chombo was written to be run in parallel and scales up to 10,000 processors [19]. In our testing of ChomboClaw we have determined that it scales to at least 128 processors, but further testing must be done on larger super computers.

My work has three aims: 1) The development of a mathematical model that captures the nonlinear steepening and propagation of the shock wave in water, as well as the shear stresses created in bone or kidney stone being treated, 2) The development of a numerical method for efficiently and robustly solving the mathematical model, and 3) Utilization of the code developed to elucidate some

of the physical mechanisms involved in shock wave therapy, and to suggest ways to optimize treatment protocols for nonunions and heterotopic ossifications based on criteria suggested by numerical experiments and biology.

The thesis is structured as follows: In Chapter 2, I provide a survey of the treatment protocols, describe the relevant biological components and discuss the physics that governs the efficacy of the treatment as suggested by experiments at APL and the literature.

Prior to presenting the mathematical model, in Chapter 3 I briefly describe the numerical approach that will be used to solve the problem, using an example from linear acoustics with spatially-varying material properties. This motivates the discussion for the equations used in the model. They are all systems of hyperbolic partial differential equations, and are therefore well-suited to being solved by the wave propagation algorithm that is fully described in Chapter 7.

In Chapter 4, I introduce the incompressible Euler equations. These equations have been studied extensively and with the appropriate equation of state, generate the correct pressure wave measured in ESWL and ESWT. I describe the eigenstructure of the linearized system as well as typical solutions to the one-dimensional Riemann problem. In this chapter I also discuss the difference between Tait and Tamman equations of state that are commonly used for modeling shock wave therapy. This chapter concludes with computational results demonstrating the accurate capture of the pressure wave as compared with experiments, and justifies the use of the Tammann equation of state in our model.

The next component of the model is linear elasticity. This model has been shown to be valid on a macroscopic scale for bone [33], and allows us to investigate the shear stress generated at the fluid-solid interface. In Chapter 5 I describe the eigenstructure of the three-dimensional system and show results from calculations where we demonstrate that our numerical approach can handle spatially varying material properties.

In Chapter 6 I develop a combined system that models the Lagrangian form of the incompressible Euler equations and elasticity. This is done using a slightly modified version of the nonlinear elasticity equations, where different materials are modeled using a different equations of state. In this section I demonstrate how our model captures the behavior of the Euler equations in a lagrangian framework for ESWT, as well as demonstrating the validity of the Tait equation of state.

Chapter 7 is devoted to computation. I explain the numerical methods for solving hyperbolic systems of PDEs using the f-wave approach, as well as the approximate Riemann solver developed to solve the nonlinear elasticity equations. In this chapter I discuss how we are able to efficiently solve three-dimensional problems using ChomboClaw, a parallel code with adaptive mesh refinement for hyperbolic systems of partial differential equations. I have been able to run large calculations on the TeraGrid system, making use of hundreds of processors and in order to perform scaling tests of the ChomboClaw system.

The laboratory experiments that motivated this investigation are described in Chapter 8. I describe how the experimental results are obtained and the relevance to *in vivo* behavior of shock wave therapy. In this chapter I will also discuss the property of birefringence and how we utilize equations for photoelasticity to more accurately compare our results with the images obtained during the laboratory experiments.

In Chapters 9 and 10 I discuss the results we have obtained up to this point with our code, and the implications for improved treatment of muskuloskeletal pathologies. Finally, I explore future work and experiments that can be performed with the code we have developed, as well as avenues for improvement.

Chapter 2

BACKGROUND

In both lithotripsy and shock wave therapy, a shock wave is generated in a liquid bath, focused through the use of an ellipsoid reflector and then propagates into the body where, ideally, maximal energy is deposited at the treatment site. A characteristic wave form measured at the focus F2 of an HM3 Dornier lithotripter can be seen in figure 2.1. The reflector used in the HM3 Dornier lithotripter is an ellipsoid and therefore has 2 foci. We refer to these foci as F1 and F2. The relevant terms are also listed in the glossary at the beginning of this document. The total duration of the pulse is approximately $5\mu s$. There is a rapid rise to pressures that can range from 40-100 MPa, followed by a longer, smoother region that has a peak pressure between -5 and -15 MPa. The fast transition from ambient pressure to tens of MPa is referred to as a shock. The physics and behavior of shock waves is explored later in this chapter.

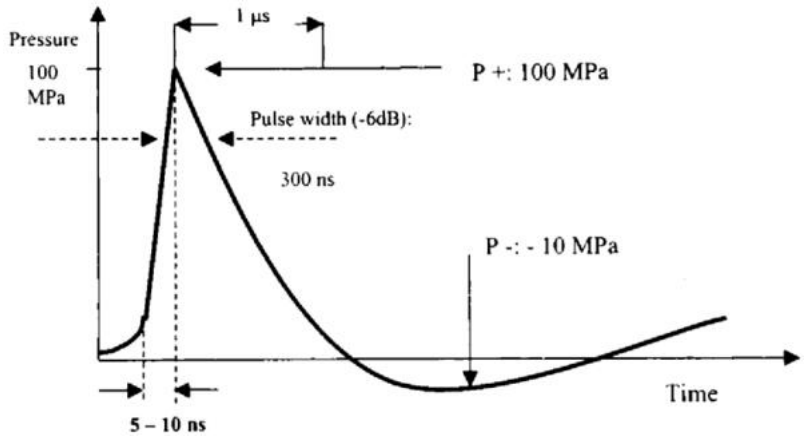

Figure 2.1: A typical pressure waveform used in medical extracorporeal shock wave therapy [4].

We first consider the development and uses of extracoporeal shock wave lithotripsy and therapy (ESWL and ESWT), then the physics and geometry pertinent to these treatments and finally we discuss some of the biological considerations for our modeling effort.

2.1 ESWL

The first clinical application of extracorporeal shock wave lithotripsy (ESWL), was on February 2, 1980 in Munich, Germany [45, 15]. In 1969, researchers first conceived of the pulverization of kidney stones with shock waves. At that time the only medical use for shock waves was the Russian "Urat" apparatus that was used for endoscopic destruction of bladder stones. In this case, there was direct contact between the shock wave source and the stone. At that time, much of the research involving shock waves was related to air and space travel, the discovery of the effect of shock waves on tissue

was accidental. In 1966, an engineer at Dornier Systems, Ltd felt something similar to an electrical shock when touching a shock wave target at the exact moment of the shock wave action. Upon further investigation, it was determined that the shock waves entering the body had caused that sensation. Subsequent studies of soft tissue damage due to shock waves were conducted in animals. It was demonstrated that shock waves generated in water were transmitted into the body without significant energy loss and measuring probes placed in the tissue were easily destroyed by the shock waves [45]. This led to the development of ESWL for the treatment of kidney stones.

ESWL has been considered a revolutionary treatment and it has been estimated that in the United States approximately 70% of kidney stones are treated using ESWL [47, 25]. The characteristic pressure pulse used in ESWL has a range of effects on the body. The shock wave pulverizes kidney stones making it possible for a patient to pass the stones in their urine; however, it also causes, in some cases significant, collateral damage in the surrounding soft tissue [53, 25].

This damage to the soft tissue has inspired some changes to the lithotripter design over the years, but the acoustic wave form has remained essentially the same. Some studies indicate that when design changes increase the amplitude and shrink the focal regions of the devices, that more soft tissue damage and higher re-treatment rates occur [15]. One of the primary goals of the lithotripsy community to design new systems that are safer and more effective. Urologists and physicists have worked together in order to determine the best treatment protocols with current technology. In order to optimally make use of the current generation of machines, it is important to understand both how they work, and how the pressure wave interacts with biological tissues.

The two primary mechanical forces generated by the ESWL acoustic field are direct stress from the high-pressure shock wave and microjets associated with the collapse of cavitation bubbles. It has been demonstrated by Sapozhinkov, et. al. [72] that the shear stresses generated by the shock wave hitting the stone plays a large role in determining the break up of the stone.

2.2 ESWT

Due to the success of ESWL at noninvasively breaking up kidney stones, clinicians decided to try using the same wave forms to break up calcium deposits that develop in soft tissue in other parts of the body, particularly in the shoulder[58]. During these treatments, and in ESWL, it was clear that one biological response that occurred was angiogenesis, or the development of new blood vessels in the region being treated. Some have hypothesized that the mechanical stimulation of the soft tissue leads to the release of growth factors such as VEGF, that lead to re-vascularization of the area [64]. After these discoveries, ESWT was then used to treat necrosis of the humeral head, a condition where the ball at the end of the humerus that inserts into the glenoid, has developed a dead region where no blood flow can get through. If left untreated, the bone will eventually break leading to shoulder replacement surgery. Clinicians had some success with ESWT for this issue, but it seems to be highly dependent upon insuring the focal region of the device is in the correct location [54]. An additional observation from these studies was that in the region treated with ESWT, there was noticeable thickening of the bone, or bone growth. Somehow, in addition to stimulating blood flow, the mechanical forces imparted by ESWT also generate osteogenesis. As a result, the same treatment was then applied to non-unions, or bone fractures that fail to heal. If a bone fracture has failed to heal in 6 months or less, but eventually does heal without treatment, it is called a delayed union. ESWT has been highly effective in treating those injuries, but the underlying biological mechanisms that lead to healing are still not well understood [64].

2.3 Physics of ESWT

In order for ESWL and ESWT to be viable treatments, a shock wave of sufficient strength must be created and transmitted to the target area safely and efficiently. This requires that the shock wave

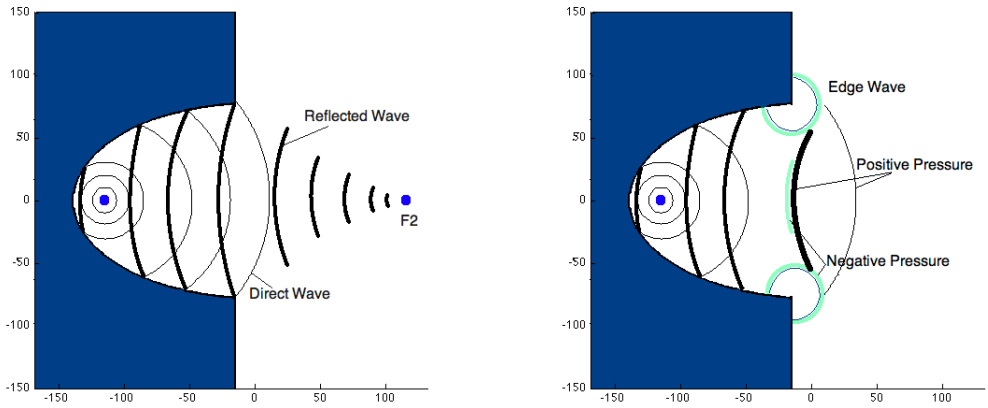

Figure 2.2: Cartoon of the HM3 Dornier Lithotripter. In a) the spherical wave is generated at F1, reflects off the ellipsoid and the reflected wave focuses at F2. In b) the diagram illustrates the creation of the edge waves at the corner of the ellipsoid and the contribution of negative pressure to the tail of the ESWT pressure wave.

be generated in a medium, such as water, that has an acoustical impedance very close to that of human tissue. To accomplish this, clinicians use a coupling gel between the water-filled bladder of the device and the patient's skin. Also, the energy of the shock wave must be concentrated so that the appropriate compressive and tensile stresses are maximized in the treatment region to cause the desired biological effects with minimal collateral damage. This is done through the use of reflectors or acoustic lenses that focus the energy of, for example, an underwater explosion. The physics that describes the steepening of the waves is similar for all focusing methodologies.

2.3.1 Models for ESWT

Our modeling effort focused on the HM3 Dornier lithotripter device because our colleagues at the Applied Physics lab were using this type of device for their experiments. The Dornier lithotripter uses a truncated ellipsoid reflector with a shock plug positioned at one focus of the ellipse, F1. The major and minor axes of the ellipsoid in the HM3 are $a = 140$mm and $b = 79.8$mm, respectively. The foci of this ellipse are at $(\pm 115, 0, 0)$ and the reflector is truncated at 100mm from F1, or $(-10, 0, 0)$. It was initially thought that the direct wave did not contribute much to the treatment [45], however Matula, et al. [56] have determined that the direct wave can play a role in excitation of cavitation bubbles. The majority of the energy is contained in the reflected wave that emerges from the reflector in the shape of a crescent. As the wave propagates, the crescent converges and the energy is concentrated in a focal area within $10 - 20$mm of F2. Ideally, the focusing of the shock wave spares the surrounding tissue and is only strong enough to damage, or treat, biological tissue at the focus.

The initial shock wave generated by the explosion is typically approximated by a positive triangular pulse [77, 18, 14, 39]. As the spherical wave expands and reflects at the ellipsoidal surface, a negative tail develops behind the shock. As the shock wave reaches the edge of the reflector, the edge wave is generated and provides the largest contribution to the negative pressure tail of the ESWT pressure waveform, this can be seen schematically in Figure (2.2).

Coleman, et al [20] made measurements of the pressure field for the Dornier HM3 lithotripter. The device used in the Applied Physics Lab at the University of Washington was designed after the HM3 and its pressure wave is similar. Pressure profiles can vary significantly depending upon the device that is being used, but the basic shape remains the same. The peak over pressure of the shock can range from $10 - 100$ MPa for the treatments of interest and the maximum negative pressure can range from $5 - 20$ MPa.

Previous researchers have modeled the pressure field using linear and nonlinear acoustics as well as the Euler equations with the Tait equation of state. Hamilton [39] used linear geometrical acoustics, which holds under the assumption of weak shock strength, to calculate the reflection of the spherical wave. The diffraction of the wave at the corner of the reflector was calculated using the Kirchoff integral method. Christopher's [14] model of the HM3 lithotripter used Hamilton's result as a starting point and considered non planar sources. Coleman et al [20], Averkiou and Cleveland [3] used models based on the KZK equation. Tanguay [77] solved the full Euler equations and incorporated cavitation effects as well as the edge wave.

Our approach differs from these in that we consider the wave propagation in both the fluid and solid by solving a single set of equations that can model both materials. This approach allows us to investigate not only compression and tension effects of ESWT, but also the propagation of shear waves in the solid. Sapozhnikov and Cleveland [16] have investigated the effect of shear waves on spherical and cylindrical stones using linear elasticity with a plane wave initial condition. This initial condition is an unfocused wave, which yields good results for small objects, but would fail to capture the full ESWT pressure wave interaction with three-dimensional bone geometries. Another benefit of our model is that we can vary the material properties for the Tait equation of state obtained from the literature, to incorporate potentially nonlinear behavior due to wave propagation in tissue.

2.3.2 Shock wave steepening

The acoustic waves generated in shock wave therapy are nonlinear and the wave speed is not constant, but depends on local properties of the fluid. In the models we are using, the sound speed is given by

$$c^2 = \frac{\gamma(p + p_\infty)}{\rho}.$$

If we consider an initial pressure profile in the shape of a Gaussian, then the wave speed at the peak of the Gaussian will be higher than the wave speed at the base causing the wave to steepen as it propagates. This is illustrated in Figure 2.3. When the wave develops a discontinuity, a shock has formed.

2.3.3 Shock wave reflection and transmission, generation of shear stress

When an acoustic wave encounters a medium with a different impedance, then part of the wave will continue to propagate into the new medium, and part will be reflected back into the original medium. In the case of normal incidence, where the propagation direction is perpendicular to the surface, the amplitude of the transmitted and reflected waves depend only on the change in impedance between the two media. In Figure 2.4, as a shock wave hits an interface, part of the wave is reflected, but since part of the wave has yet to hit the interface, there will be an interaction of the incoming and reflected waves. This leads to a larger region of negative pressure near the interface of the two materials. It has been suggested that this phenomena is the reason cavitation bubbles are prevalent near the surface of the stones in ESWL [45], and in principle, the same would be true for the interface between tissue and bone.

The intensity transmission and reflection coefficients measure the intensity or energy of the transmitted and reflected components of the shock wave. Cleveland and McAteer [15] calculated

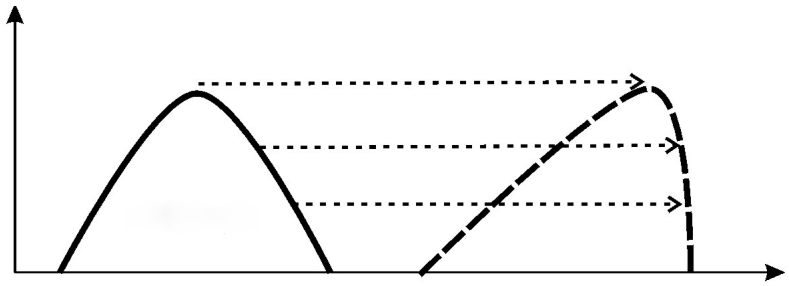

Figure 2.3: Wave steepening as it propagates to the right, components with higher pressure travel at a greater speed leading to the formation of a shock front.

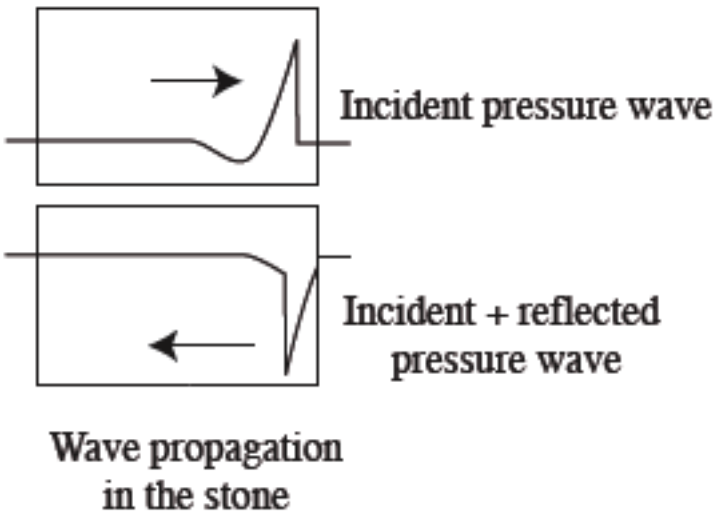

Figure 2.4: Behavior of the pressure wave at an interface.

the intensity transmission coefficient for an acoustic wave propagating with normal incidence from water into soft tissue, kidney stones, bone and air. The transmission from water to soft tissue is nearly 100% and from water to bone was around 60%. In the case of a water-air interface, 0.1% of the energy is transmitted from water to air. This is why shock waves for ESWL and ESWT are generated in water and patients are either submerged in a water bath or a coupling gel is used to insure maximum energy transmission.

The shear modulus of tissue is very close to zero, and within water it is zero. A zero shear modulus means these materials do not support shear stresses. However, a wave propagating through the fluid that then hits a solid can generate shear stresses within the solid. Sapozhnikov, et. al. [72] investigated the role of compression, tensile and shear stresses on cylindrical kidney stones. They found that greater tensile stresses in lithotripsy led to break up of the idealized stones with fewer shocks. Tensile stresses in the stone were maximized when shear stresses were generated at the corners of the stone. In the absence of this shear stress, the stone required thousands more shocks before breaking. In ESWT the shear stress generated at the interface between the two materials is thought to in part lead to bone growth and angiogenesis. It is therefore important to understand and model the shear stresses generated by the shock wave in ESWL and ESWT.

2.3.4 Shock wave interaction with tissue

The acoustic field of the a lithotripter or shock wave therapy device is typically measured using a hydrophone, which converts pressure into an electrical signal. Most reference measurements obtained using a hydrophone have been done through *in vitro* experiments. There have been few attempts to collect pressure data from within animals [15]. From experiments done using the HM3 Dornier lithotripter and a PVDF Hydrophone implanted in a pig, experimentalists have determined that the resultant wave form is similar in shape to that of an *in vitro* waveform. The biggest difference is the positive peak pressure was decreased by 30% and the shock rise time was longer [15]. These effects are consistent with the higher attenuation that would be associated with a viscoelastic material like soft tissue.

2.3.5 Cavitation

Cavitation is the formation of bubbles in a liquid that occurs when the pressure in the liquid falls below a certain threshold. In ESWT, the tensile component of the pressure wave has negative pressures that are on the order of -15 MPa. These tensile stresses lead to the generation of cavitation bubbles in soft tissue during treatment, particularly in lithotripsy as the shock wave must travel through a larger amount of soft tissue.

We do not model cavitation effects with our code. However, we have been able to compare the results from our calculations with the cavitation fields photographed in laboratory experiments [30]. In order to perform the comparison, we calculate the maximum tensile stresses over the course of the calculation. This is considered to be a reasonable predictor for where cavitation bubbles are likely to occur.

In ESWT, the soft tissue component surrounding a broken bone or tendon is significantly smaller than what is considered in lithotripsy. While cavitation effects probably play a role in the break up of heterotopic ossifications, it is less clear that it plays a strong part in the healing of non-unions. Delius et al [64] found that treatment of non-unions in rabbits and sheep with high energy shock waves led to the generation of microcracks and detatchment of the periosteum from the bone. Further, they found that the bone marrow content and fat were pressed out of the marrow canal underneath the periosteum. This suggests compression of the bone as well as shearing at the bone-tissue interface.

2.3.6 Applications of Shock Wave Therapy

Nonunions

If a bone fracture fails to unite or heal over a period of six months or longer, it is classified as a nonunion. Some causes of nonunions are insufficient immobilization, infection or inadequate blood supply. The normal bone healing process has been interrupted and fails to complete. In a few cases, nonunions will go on to heal, but these fractures are then classified as delayed unions.

Typical treatment for nonunions involves orthopedic surgery where either a bone graft or hardware is used to encourage closure of the fracture. The type of treatment depends on the type of nonunion. In cases where the gap between the two bones is within a few millimeters, ESWT has proven to be an effective noninvasive alternative to surgery [64].

Tendonitis and Tendinopathies

Tendons are the anatomic structures that connect muscle to bone and make joint movement possible. A tendon is composed of bundles of collagen fibers, and when a joint is overused the collagen weakens and the tendon degenerates leading to pain. If the region is also inflamed, the injury is classified as tendonitis.

Treatment has traditionally focused on providing anti-inflammatory measures. This has included nonsteroidal anti-inflammatory drugs (NSAIDs), steroid injections, and physical therapy. Many clinical trials have been performed to evaluate the efficacy of ESWT for the treatment of tendinitis in the knee, shoulder and plantar fascia, but the results to date are not conclusive [74]. In some cases ESWT was found to be effective, in others it performed no better than placebo. ESWT has been shown to be more effective when patients provide feedback that enables focusing of the shock wave on the most painful areas, as opposed to using image-guided focusing to direct the wave toward anatomical structures. This indicates that ESWT is responsible for more of an analgesic effect where nerves are possibly being damaged leading to the reduction in pain [68].

Heterotopic Ossifications

Heterotopic ossification (HO) is the abnormal formation of true bone within extraskeletal soft tissues. HO originates from osteoprogenitor stem cells lying dormant within the affected soft tissues [8]. With the proper stimulus, the stem cells differentiate into osteoblasts and begin the process of osteoid formation, eventually leading to mature heterotopic bone. Most patients are encouraged to continue using the joint in an effort to continue having full range of motion. Once the HO has grown to the point of limiting the patient's ability to move their limb, doctors use either surgery or radiation therapy. Surgery can only be undergone once no new bone is forming, otherwise there is a recurrence rate of nearly 100 percent [76].

ESWT has been used to treat heterotopic ossifications [57]. It is believed that by generating large shear stresses at the interface between the bone and ossification, the ossification can be dislodged, causing the patient to regain range of motion in the joint.

2.4 Biology

We are interested not only in how the pressure wave is generated and propagates within an idealized laboratory setting, but also in wave propagation through biological materials such as bone and soft tissue. Therefore, it is important that our modeling of these materials be as accurate as possible. The mechanical properties of materials are specified by constitutive equations. There are a great many constitutive equations describing an almost infinite variety of materials. According to Fung [33], three simple, idealized stress-strain relationships describe the mechanical properties of many

materials. These three models are the Hookean elastic solid, the nonviscous fluid and the Newtonian viscous fluid. however, most biological materials cannot be described so simply. Here we focus on the Hookean and viscoelastic models.

2.4.1 Hookean models

If the stress in a material can be linearly related to the strain, or the strains are infinitesimal, that material is said to obey Hooke's law. In one-dimension Hooke's law can be stated as,

$$\sigma = K\epsilon,$$

where σ is the stress, K is the bulk modulus and ϵ is the strain. In general, σ is a stress tensor that is linearly related to the strain tensor ϵ,

$$\begin{aligned}
\sigma_1 &= C_{11}\epsilon_1 + C_{12}\epsilon_2 + C_{13}\epsilon_3 + C_{14}\epsilon_4 + C_{15}\epsilon_5 + C_{16}\epsilon_6 \\
\sigma_2 &= C_{21}\epsilon_1 + C_{22}\epsilon_2 + C_{23}\epsilon_3 + C_{24}\epsilon_4 + C_{25}\epsilon_5 + C_{26}\epsilon_6 \\
\sigma_3 &= C_{31}\epsilon_1 + C_{32}\epsilon_2 + C_{33}\epsilon_3 + C_{34}\epsilon_4 + C_{35}\epsilon_5 + C_{36}\epsilon_6 \\
\sigma_4 &= C_{41}\epsilon_1 + C_{42}\epsilon_2 + C_{43}\epsilon_3 + C_{44}\epsilon_4 + C_{45}\epsilon_5 + C_{46}\epsilon_6 \\
\sigma_5 &= C_{51}\epsilon_1 + C_{52}\epsilon_2 + C_{53}\epsilon_3 + C_{54}\epsilon_4 + C_{55}\epsilon_5 + C_{56}\epsilon_6 \\
\sigma_6 &= C_{61}\epsilon_1 + C_{62}\epsilon_2 + C_{63}\epsilon_3 + C_{64}\epsilon_4 + C_{65}\epsilon_5 + C_{66}\epsilon_6.
\end{aligned}$$

Anisotropic linear coefficients obtained through ultrasound stiffness measurements can be found in Table (2.1). A bone will typically be anisotropic because bone grows in response to applied loads, which in the human body, are highly anisotropic[55]. This anisotropic structure would probably have an effect on the direction of propagation within the bone, but for our modeling efforts we have assumed bone is an isotropic material.

Table 2.1: Elastic coefficients for the anisotropic linear stress tensor (GPa) [55]

Coefficient	plexiform bone (primary bone)	haversian (secondary bone)
C_{11}	22.4 ± 0.6	21.2 ± 0.5
C_{22}	25.0 ± 1.0	21.0 ± 1.4
C_{33}	35.0 ± 2.0	29.0 ± 1.0
C_{44}	8.2 ± 0.4	6.3 ± 0.4
C_{55}	7.1 ± 0.3	6.3 ± 0.2
C_{66}	6.1 ± 0.2	5.4 ± 0.2
C_{12}	14.8 ± 0.8	11.7 ± 0.7
C_{23}	13.6 ± 0.7	11.1 ± 0.8
C_{13}	15.8 ± 0.8	12.7 ± 0.8

In the case of a linear, isotropic solid with averaged material properties, the above system sim-

plifies to

$$\begin{aligned}
\sigma_1 &= C_{11}\epsilon_1 + C_{12}\epsilon_2 + C_{13}\epsilon_3 \\
\sigma_2 &= C_{21}\epsilon_1 + C_{22}\epsilon_2 + C_{23}\epsilon_3 \\
\sigma_3 &= C_{31}\epsilon_1 + C_{32}\epsilon_2 + C_{33}\epsilon_3 \\
\sigma_4 &= C_{44}\epsilon_4 \\
\sigma_5 &= C_{55}\epsilon_5 \\
\sigma_6 &= C_{66}\epsilon_6.
\end{aligned}$$

More information on this form for the stress tensor can be found in Chapter 5.

2.4.2 Viscoelasticity

The most commonly used linear viscoelastic models are the Maxwell, Kelvin-Voigt and Standard Linear Solid. The Maxwell model combines a spring and dashpot in series, which allows for stress relaxation. The Kelvin-Voight model combines a spring and dashpot in parallel, thereby incorporating creep, but losing accuracy in its modeling of stress relaxation. The Standard Linear Solid is more complicated, but by combining a Maxwell and Kelvin-Voigt type model in parallel, it is able to incorporate many of the desired viscoelastic effects like creep and stress relaxation. However, there are more parameters that need to be measured from experiments.

The propagation of shock waves through viscoelastic material in one-dimension was undertaken in [38]. The authors derived some relations for the relaxation of the material behind the shock, as well as formulas for the shock speed.

2.4.3 Skeletal Biology

The primary uses of ESWT to date involve the musculoskeletal system. In order to effectively model the shock wave interaction with the bone, it is important to have a good mathematical characterization of the different bone tissues. Different treatments will necessitate the modeling of different parts of the bone geometry, which are comprised of different tissue types. When focused on a nonunion that has occurred in the long shaft of the bone, the model will consist of primarily cortical bone and bone geometry is well approximated by a cylinder. However, when treating necrotic femoral or humeral head, the shock wave interacts with the ends of the bone, which are rounded and are mostly made up of trabecular bone. In this section I will describe the fundamental differences in the bone types from a mathematical modeling perspective, as well as the role played by the different cell types in the healing process.

While the shapes of our bones are quite variable in terms of curvature and length, the skeletal architecture is fairly stereotypical within a given species [55]. This means that an isolated bone or fragment of a bone can be identified as human and not belonging to, say, one of the other primates. This would seem to indicate that the structure of bone is reasonably static with size and shape being dictated by species. If we examine a bone at the scale of centimeters, then this is true. However, if we focus instead on the scale of milimeters to microns, it becomes clear that bone is an incredibly dynamic tissue that is constantly remodeling in response its mechanical environment [55, 28].

If you were to cut open a variety of bones from the body and wash out the marrow, it would be clear that there are two main types of bone, cortical or compact and trabecular or spongy bone. The porosity of a single bone can vary from zero to 100%, but most bone tissue has either very high or very low porosity, with a small amount of the bone having porosity between 25% and 75% [55]. Trabecular bone is porous bone (75%-95% porosity), found in the vertebrae, flat bones and

in the ends of long bones. The arrangement of the trabeculae, or components of the bone matrix, can sometimes be in orthogonal arrays, but more often are randomly arranged. At the other end of the spectrum, cortical bone is extremely dense and found in the shafts of long bones as well as in the shells surrounding trabecular bone. Within the cortical bone, there are the following structures, Haversian canals that contain capillaries and nerves, Volkmann's canals that connect Haversian canals and contain blood vessels as well as nerves, and resorption cavities that are temporary spaces created by bone cells during remodeling.

Within both cortical and trabecular bone, there are two types of bone tissue, lamellar and woven bone. Lamellar bone has a highly organized structure comprised of parallel layers of anisotropic mineral crystals and collagen fibers. Woven bone is quickly formed and has a poorly organized structure in which the mineral crystals and collagen fibers are randomly arranged. In some cases, woven bone is more highly mineralized than lamellar bone, this may help compensate for its lack of organization [55]. However, woven bone, while more quickly made, is weaker than lamellar bone.

The shape of the bone and location in the body dictates the underlying composition. The long shafts of the bone are reasonably static and have a cylindrical shape, while the ends of the bone (chondyle and epichondyle regions) have more dynamic structures that are primarily composed of trabecular bone. This is due to the fact that the ends of the bone are components of joints that are subject to a wider range of directional forces than the bone shafts as we move.

Another important structure involved with bone remodeling, growth and healing is the periosteum. This thin layer of soft tissue surrounds each bone. When the periosteum is disturbed, due to a fracture or some mechanical stress that is applied to the bone, it responds by sending signals to cells within the bone and within the muscle to draw the necessary blood supply and nutrients.

Bone remodeling

Bones are able to sense changes in the mechanical loads they bear and will modify their structure to better support these loads. This is known as Wolff's law and was originally stated as

" Every change in the form and function of... bone[s] or of their function alone is followed by certain definite changes in their internal architecture, and equally definite secondary alterations in their external conformation, in accordance with mathematical laws." - J. Wolff [55, 28, 32]

The idea that bone not only repairs itself, but also adapts to variations in imposed stresses, is one that has been examined and tested over the years. Three key ideas to arise from studies in this area are that bones optimize strength with respect to the weight they are bearing; the trabeculae align with principal stress directions; and cells respond to mechanical stimulus that leads to regulation and remodeling of the bone structure [55].

In ESWT, we are concerned with the case when bones remodel in response to fracture, an extreme case were enough force is applied to cause the bone to break. Two tissues provide the cells responsible for healing a typical fracture, the periosteum and the bone marrow. Ordinarily, the osteoblasts in an adult periosteum produce lamellar bone at a relatively slow rate. However, even a slight amount of trauma stimulates the periosteum to produce more osteoblasts that quickly manufacture a large amount of woven bone. In the event of a break or fracture to the bone, the woven bone forms what is called the periosteal callus. This is essentially an arch of bone that connects from one side of the break to another, and is the body's way of holding the bone together while more woven bone can be constructed inside the break. The bone lining cells, the same cells that are stimulated to initiate bone remodeling by mechanical factors, also respond to trauma to the bone marrow. The factors released by the bone marrow in response to the break, lead to the formation of the endosteal callus in the gap between the two bones.

It has been demonstrated that mechanical disruption of the marrow, even without the presence of a cortical fracture, activates the cells necessary for the formation of an endosteal callus [2]. This must occur in order for blood cell production to return to normal. The periosteal callus is more

noticeable, but the edosteal callus is thought to be more important in the initial union of the fracture [55]. If this process is interrupted or incorrect chemical signals are sent to the body, this results in a nonunion. It seems reasonable to hypothesize that the applied mechanical stress of ESWT, possible pulsatile flow generated in the bone marrow, and damage done to the bone are some of the mechanisms that lead to the bone regeneration after treatment.

2.4.4 Soft tissue

The viscoelastic behavior of various fibrous tissues (skin, cartilage, blood vessel walls) has been studied in depth by Fung [33]. He found that for many tissues, linear viscoelastic models apply as long as the strains are small. We have assumed (and justified through calculation of the displacements in our model) for ESWT that the tissue is undergoing small displacements near F2 and can therefore be modeled as a linear viscoelastic material. We have completed some one-dimensional models of the pressure wave interacting with a linearly viscoelastic material.

Justification for modeling as water

Though the results from using a viscoelastic stress-strain relationship in our modeling effort yield some idea of what will happen to the pressure wave as it propagates through soft tissue, we have not yet determined how to extend this to a multi-dimensional model. Since the shear modulus for tissue is very nearly zero, we initially used water as the tissue model for all experiments. This has been done by several research groups [43, 70, 72], and has served as good starting point for investigating the interaction of the wave with complicated bone geometries. We then extended the model to include gelatinous tissue using variable parameters for the Tait equation of state.

Tait EOS Parameterization for Tissue

Nakahara, et al [60] measured the Hugoniot data for a series of shock experiments in water, gelatin and saline solutions. They used the Grüneisen equation of state combined with the Hugoniot and Gibbs equation to demonstrate that the change of entropy due to shock compression for the range of pressures applicable to ESWT, only affected the internal energy, not the pressure or sound velocity [60]. They used this as a justification for modeling the pressure with the modified Tait equation of state, that was then used to fit experimental data in order to determine the parameters in Table 2.2.

Since we have demonstrated in Chapter 4 that we can use the isentropic equations near F2 in our calculations, we can utilize the parameters measured by Nakahara, et. al. to model wave propagation in gelatinous tissue surrounding the bone.

Table 2.2: Material dependent parameters for the Tait equation of state [60]

Material	B	n
Water	300 MPa	7.15
Saline (10 %)	248 MPa	7.0
Gelatin (10%)	276 MPa	7.0

Chapter 3

FINITE VOLUME METHODS

In subsequent chapters we provide implementation details for the linear elasticity equations and the Lagrangian form for the isentropic Euler equations. In order to provide the necessary background to discuss each of those systems, we introduce the basic numerical method and CLAWPACK by considering the one-dimensional acoustics equations in this chapter.

3.1 Hyperbolic Systems of Conservation Laws

The general form of a system of m conservation laws in d space dimensions is

$$\frac{\partial}{\partial t}q + \sum_{j=1}^{d} \frac{\partial f_j(q)}{\partial x_j} = 0, \quad x = (x_1, \ldots, x_d)^T \in \mathbb{R}^d, \quad t > 0, \tag{3.1}$$

where $q = (q_1, \ldots, q_m)^T$, $q_p = q_p(x,t)$, $1 \le p \le m$, is the vector of the state variables, and $f_j = (f_{1j}, \ldots, f_{mj})^T$, $1 \le j \le d$, are called flux functions.

We can see that the system 3.1 expresses the conservation of the m quantities $q_1, \ldots, q_p$. In fact, let Ω be an arbitrary domain in $\mathbb{R}^d$, and $n = (n_1, \ldots, n_d)^T$ the outward unit normal to the boundary $\partial\Omega$ of Ω. Then, from 3.1 we have

$$\frac{d}{dt}\int_{\Omega} q dx + \sum_{j=1}^{d} \int_{\partial\Omega} f_j(q) n_j \, dS = 0. \tag{3.2}$$

This balance equation states that the positive time variation of $\int_\Omega q \, dx$ is equal to the inward flux of q through the boundary $\partial\Omega$.

We are interested in studying systems of conservation laws that are hyperbolic,

Definition For $j = 1, \ldots, d$, let

$$A_j(q) = \left(\frac{\partial f_{ij}}{\partial q_p}\right)_{1 \le i,p \le m}$$

be the Jacobian matrix of $f_j(q)$; the system 3.1 is called hyperbolic if for any $q \in \Omega$ and any $\omega = (\omega_1, \ldots, \omega_d)^T \in \mathbb{R}^d$, $|\omega| = 1$, the matrix

$$A(q, \omega) = \sum_{j=1}^{d} \omega_j A_j(q)$$

has m real eigenvalues $\lambda^1(q,\omega) \le \lambda^2(q,\omega) \le \cdots \le \lambda^m(q,\omega)$ and m linearly independent corresponding eigenvectors $r^1(q,\omega), \ldots, r^m(q,\omega)$, that is

$$A(q,\omega)r^p(q,\omega) = \lambda^p(q,\omega)r^p(q,\omega), \quad 1 \le p \le m.$$

If, in addition, the eigenvalues $\lambda^p(q,\omega)$ are all distinct, then the system 3.1 is called strictly hyperbolic.

For hyperbolic systems introduced here we shall consider the initial value problem consisting of the equations (3.1) augmented with the initial condition $q(x,0) = q_0(x)$, where $q_0(x)$ is a given function defined on $\mathbb{R}^d$.

3.1.1 Weak Solutions

A classical solution of (3.1) is a smooth function q that satisfies (3.1). An important feature of the problems of interest is that we must allow for discontinuous solutions. Such functions cannot satisfy the partial differential equations (3.1), but do satisfy the integral form of the conservation laws

$$\int_{\mathcal{T}} \int_{\Omega} q dx dt + \sum_{j=1}^{d} \int_{\mathcal{T}} \int_{\partial\Omega} f_j(q) n_j dS dt = 0, \quad \forall \Omega \subseteq \mathbb{R}^d, \ \forall \mathcal{T} \subseteq [0, +\infty). \tag{3.3}$$

Hence we appeal to the integral form (3.3) to define a solution q in a generalized sense, or weak solutions of (3.1).

If we consider a piecewise smooth function q, then in the regions where q is smooth it is a classical solution, while we can use the integral form of the equations to derive conditions that hold across discontinuities. Specifically, denoting with $q_\pm$ the limits of q on each side of a surface of discontinuity, the following Rankine-Hugoniot condition is satisfied

$$s(q_+ - q_-) = \sum_{j=1}^{d} n_j (f(q_+) - f(q_-)), \tag{3.4}$$

where s represents the speed of propagation of the discontinuity and $n \in \mathbb{R}^d$ is a unit vector indicating the direction of propagation.

A weak solution to a system of conservation laws is not necessarily unique, hence we need to select among the possible weak solutions the unique physically relevant solution of the problem. This is called the entropy solution and can be viewed as the limit of the viscous problem associated to the considered hyperbolic problem as the viscosity parameter goes to zero.

3.1.2 One-Dimensional Riemann Problem

Consider the one-dimensional system

$$\frac{\partial q}{\partial t} + \frac{\partial f(q)}{\partial x} = 0, \quad x \in \mathbb{R}, \quad t > 0. \tag{3.5}$$

Here q is a vector of m conserved quantities and $f(q)$ the corresponding flux function. We will assume that (3.5) is strictly hyperbolic, so the Jacobian matrix $A(q) = f'$ has m distinct real eigenvalues $\lambda^p(q)$ and m linearly independent eigenvectors $r^p(q), 1 \le p \le m$. Most of the results discussed here will also hold for a non-strictly hyperbolic system as long as the eigenvectors form a complete basis.

For (3.5), we shall consider initial data with the particular form

$$q_0(x) = \begin{cases} q_l & \text{if } x < 0 \\ q_r & \text{if } x > 0 \end{cases}. \tag{3.6}$$

In such a case, problem (3.5), (3.6) is called the one-dimensional Riemann problem.

Note that solutions $q(x,t)$ to this problem are self-similar, that is $q(x,t) = q_{Riem}(\frac{x}{t})$.

Linear Systems

For a linear system $\partial q/\partial t + A\partial q/\partial x = 0$, with a constant coefficient matrix A, the solution of the Riemann problem consists of $(m+1)$ constant states $q^{*0} = q_l, q^{*1}, \ldots, q^{*(m-1)}, q^{*m} = q_r$, separated by m discontinuities that propagate at speeds given by the eigenvalues of A. Each constant state can be expressed as $q^{*p} = q_l + \sum_{k=1}^{p} \alpha^k r^k$, there the coefficients α^k are obtained by projecting the jump $q_r - q_l$ onto the eigenvectors of A, i.e., $q_r - q_l = \sum_{p=1}^{m} \alpha^p r^p$.

Nonlinear Systems

Let us consider a single discontinuity connecting two states q_l and q_r and traveling at speed s. In order for this discontinuity to be a weak solution of the Riemann problem, the Rankine-Hugoniot condition must be satisfied

$$s(q_r - q_l) = f(q_r) - f(q_l). \tag{3.7}$$

In a genuinely nonlinear field a discontinuous solution of this type is a shock wave, whereas in a linear degenerate field it is called a contact discontinuity.

Definition The p-th characteristic field is said to be genuinely nonlinear if

$$\nabla \lambda^p(q) \cdot r^p(q), \quad \forall q \in \Omega. \tag{3.8}$$

Definition The p-th characteristic field is said to be linearly degenerate if

$$\nabla \lambda^p(q) \cdot r^p(q) = 0, \quad \forall q \in \Omega. \tag{3.9}$$

In the case of a shock wave, the Lax entropy condition is used to insure that a physically relevant solution is selected. The Lax entropy condition requires that $\lambda^p(q) > s > \lambda^p(q)$, which means that the characteristics impinge on the shock.

In a genuinely nonlinear field with a smoothly varying solution, a rarefaction wave can occur. This solutions has the property of lying on integral curves of the characteristic field, i.e. curves $v(\xi)$ satisfying $v'(\xi) = r^p(v(\xi))$. If the characteristic fields of the system (3.5) are either genuinely nonlinear or linearly degenerate, the Riemann problem has a unique weak solution, assuming $|q_r - q_l|$ is sufficiently small; moreover, this solution consists of at most $(m+1)$ constant states separated by rarefaction waves, shocks, or contact discontinuities.

3.2 Godunov-Type Methods

For the numerical solution of hyperbolic systems of conservation laws we consider Godunov-type schemes that represent a particular class of finite volume methods.

Consider a discretization in space and time with spatial interval Δx and time step Δt. We define the discrete points (x_i, t^n) by $x_i = i\Delta x, i \in \mathbb{Z}$, and $t^n = n\Delta t, n \in \mathbb{N}$. In the finite volume approach, the numerical solution $Q_i^n \in R^m$ at the point (x_i, t^n) is viewed as an approximation of the average of the exact solution $q(x,t)$ at time t^n over the spatial cell $\mathcal{C}^i = (x_{i-1/2}, x_{i+1/2})$,

$$Q_i^n \approx \frac{1}{\Delta x} \int_{\mathcal{C}^i} q(x, t^n)\ dx \equiv \bar{Q}_i^n. \tag{3.10}$$

We shall consider 3-point explicit schemes of the following type:

$$Q_i^{n+1} = Q_i^n - \frac{\Delta t}{\Delta x} \left[F(Q_i^n, Q_{i+1}^n) - F(Q_{i-1}^n, Q_i^n) \right], \tag{3.11}$$

where the function $F : R^m x R^m \rightarrow \mathbb{R}^m$ is called the numerical flux. We know that every weak solution $q(x,t)$ satisfies the integral form of the conservation law,

$$\int_{\mathcal{C}_i} q(x,t^{n+1})dx = \int_{\mathcal{C}_i} q(x,t^n)dx - \left[\int_{t^n}^{t^{n+1}} f(q(x_{i+1/2},t))dt - \int_{t^n}^{t^{n+1}} f(q(x_{i-1/2},t))dt\right]. \quad (3.12)$$

Dividing by Δx and using the cell average (3.10), we have

$$\bar{Q}_i^{n+1} = \bar{Q}_i^n - \frac{1}{\Delta x}\left[\int_{t^n}^{t^{n+1}} f(q(x_{i+1/2},t))dt - \int_{t^n}^{t^{n+1}} f(q(x_{i-1/2},t))dt\right]. \quad (3.13)$$

Comparing this to (3.11), it is clear that the numerical flux function $F(Q_i^n, Q_{i+1}^n)$ plays the role of the average physical flux through $x_{i+1/2}$ over the time interval $[t^n, t^{n+1})$

$$F(Q_i^n, Q_{i+1}^n) \approx \frac{1}{\Delta t}\int_{t^n}^{t^{n+1}} f(q(x_{i+1/2},t))dt. \quad (3.14)$$

In order to insure that the numerical flux is consistent, we will in general require $F(x,x) = f(x)$, for all x and that it is Lipschitz continuous.

Godunov-type methods are based on solving Riemann problems between cell averages Q_i^n, Q_{i+1}^n in order to define the numerical flux $F(Q_{i+1}^n, Q_i^n)$ at the interface $x_{i+1/2}$. We can either compute the exact solution of the Riemann problem at each cell interface, as was originally done by Godunov [35], or we can use an approximate solution. A wide variety of approximate Riemann solvers have been proposed that can be applied with less computational effort than the exact Riemann solvers, and in many cases are equally effective.

3.3 Approximate Riemann Solvers

Approximate Riemann solvers are necessary for nonlinear problems where an exact Riemann solver, while tractable analytically, is too computationally intensive to solve at every grid cell interface. The general structure of approximate Riemann solver we are interested in consists of m waves $W^p \in R^m$ propagating at some speeds $s^p \in R, p = 1, 2, \ldots, m$. Given states q_r and q_l for the right and left state of the Riemann problem, the vectors W^p represent the jump in q across each wave and their sum must recover the total jump

$$q_r - q_l = \sum_{p=1}^{m} \mathcal{W}^p. \quad (3.15)$$

The following conservation condition must also be satisfied

$$f(q_r) - f(q_l) = \sum_{p=1}^{m} s^p \mathcal{W}^p. \quad (3.16)$$

The numerical flux can then be written as

$$F(Q_i, Q_{i+1}) = f(Q_i) + \sum_{p=1}^{m} \left(s_{i+1/2}^p\right)^- \mathcal{W}_{i+1/2}^p \quad (3.17)$$

$$= f(Q_{i+1}) - \sum_{p=1}^{m} \left(s_{i-1/2}^p\right)^+ \mathcal{W}_{i-1/2}^p, \quad (3.18)$$

where $s^+ = \max(s,0)$,$s^- = \min(s,0)$, and the subscript $(i+1/2)$ indicates quantities computed for the Riemann problem at $x_{i+1/2}$. The updating formula (3.11) then takes the form of the following first-order upwind scheme

$$Q_i^{n+1} = Q_i^n - \frac{\Delta t}{\Delta x}\left[\sum_{p=1}^{m}\left(s_{i+1/2}^p\right)^- \mathcal{W}_{i+1/2}^p + \sum_{p=1}^{m}\left(s_{i-1/2}^p\right)^+ \mathcal{W}_{i-1/2}^p\right]. \tag{3.19}$$

For stability the CFL condition [51] must hold

$$\frac{\Delta t}{\Delta x}\max_p |s^p| \le 1, \quad 1 \le p \le m. \tag{3.20}$$

3.3.1 Roe Solver

One of the most extensively used approximate Riemann solvers is due to Roe [67]. The idea is to determine an approximate Riemann solution by solving a linear system with a constant coefficient matrix $\hat{A} = \hat{A}(q_l, q_r)$, in lieu of the original nonlinear system.

Definition 3.3.1 The matrix $\hat{A}(q_l, q_r)$ is called a Roe linearization if it is endowed with the following properties:

- Hyperbolicity of the linearized system, $\hat{A}(q_l, q_r)$ has real eigenvalues and complete set of eigenvectors;

- Consistency,
$$\hat{A}(q_l, q_r) \to f'(\bar{q}) \text{ as } q_l, q_r \to \bar{q}; \tag{3.21}$$

- Conservation condition,
$$f(q_r) - f(q_l) = \hat{A}(q_l, q_r)(q_r - q_l). \tag{3.22}$$

Consider the eigenstructure of $\hat{A}$, with eigenvalues $\hat{\lambda}^p$ and eigenvectors $\hat{r}^p$, and let α^p be the weights of the projection of the jump $(q_r - q_l)$ onto the eigenvectors. Then the waves W^p and corresponding speeds s^p that form the Roe solver are given by

$$W^p = \alpha^p \hat{r}^p \text{ and } s^p = \hat{\lambda}^p, \quad p = 1, \ldots, m. \tag{3.23}$$

Roe [67] suggests that $\hat{A}$ should have the following form

$$\hat{A}(q_l, q_r) = A(\hat{q}), \quad \hat{q} = \hat{q}(q_l, q_r), \tag{3.24}$$

where $A(q) = f'$ is the Jacobian matrix of the original system and $\hat{q} = \hat{q}(q_l, q_r)$ is an average state defined so that the properties of Definition 3.3.1 will hold. In particular, Roe derives $\hat{A}(q_l, q_r)$ for the Euler equations of gas dynamics with the ideal gas law. The main drawback to the Roe solver is that it may compute entropy-violating solutions. This occurs when the true solution of the Riemann problem contains a transonic rarefaction where λ^p changes sign through the rarefaction fan. The failure of the solver is caused by the approximation of the rarefaction by a single discontinuity. This is typically circumvented by the use of an 'entropy fix', see for example [51].

3.4 Linear Acoustics

As a particular example of the type of equations we are interested in, we consider the one-dimensional linear acoustics equations,

$$q_t + A(x)q_x = 0, \tag{3.25}$$

where

$$q = \begin{bmatrix} p \\ u \end{bmatrix}, A(x) = \begin{bmatrix} 0 & k(x) \\ 1/\rho(x) & 0 \end{bmatrix}. \tag{3.26}$$

In a heterogeneous medium, the density ρ and bulk modulus k, vary in space.

Finite volume methods divide the computational domain into cells that are separated by cell interfaces. State variables are typically defined as piecewise constant, so that within a given cell all of the state variables are constant. All variability in the state variables occurs at cell interfaces, so a cell centered at x_i will potentially have jumps in the state variables at the interfaces $x_{i-1/2}$ and $x_{i+1/2}$. In 1D acoustics, the i'th cell has material properties ρ_i and k_i, and the sound speed is given by $c_i = \sqrt{k_i/\rho_i}$.

Ideally, we would have the interface between different materials aligned identically with cell interfaces. While in 1D it is straight-forward to align the material interfaces with the grid, in 2D the material interfaces will likely cut the Cartesian grid at some angle, necessitating greater grid refinement and averaging at the interfaces. In 1D, if the materials do not align with the grid, we use the arithmetic average of the material properties of each material. For acoustics, we could use the arithmetic average of ρ, i.e. the value of ρ in the ith cell is $\rho_i = \bar{\rho}_i$ where

$$\bar{\rho}_i = \frac{1}{\Delta x} \int_{x_{i-1/2}}^{x_{i+1/2}} \rho(x)\, dx. \tag{3.27}$$

For the bulk modulus, k, we use the harmonic average

$$\bar{k_i} = \Delta x \left(\int_{x_{i-1/2}}^{x_{i+1/2}} \frac{1}{k(x)}\, dx \right)^{-1}. \tag{3.28}$$

Similarly, the state variables may not be piecewise constant within a given grid cell, so we also use averaging of these variables to obtain data that vary only at grid cell interfaces. We denote the cell averages for the state variable q at grid cell i, by Q_i. At each cell interface, say $x_{i+1/2}$ there will be a difference in the state variables that is governed by equation (3.25). We are therefore interested in solving the system (3.25) with piecewise constant initial data, with a single discontinuity at $x_{i+1/2}$, this is the definition of a Riemann problem. The numerical solution of all the equations we are interested in, are based on solving Riemann problems.

To solve each Riemann problem at the cell interfaces, we utilize the eigenstructure of the Jacobian of the flux function of the system we are interested in solving. For the 1D acoustics, the eigenvalues and eigenvectors are

$$R = \begin{bmatrix} r^1 & r^2 \end{bmatrix} = \begin{bmatrix} -\rho c & \rho c \\ 1 & 1 \end{bmatrix}, \quad \Lambda = \begin{bmatrix} -c & 0 \\ 0 & c \end{bmatrix}. \tag{3.29}$$

Since the sound speed, c and impedence ρc vary spatially, it is important to use a local evaluation of the flux function to calculate the eigenvalues and eigenvectors. For the ith grid cell, the eigenvalues and eigenvectors would be given by

$$R = \begin{bmatrix} r^1 & r^2 \end{bmatrix} = \begin{bmatrix} -\bar{\rho}_i \bar{c}_i & \bar{\rho}_i \bar{c}_i \\ 1 & 1 \end{bmatrix}, \quad \Lambda = \begin{bmatrix} -\bar{c}_i & 0 \\ 0 & \bar{c}_i \end{bmatrix}. \tag{3.30}$$

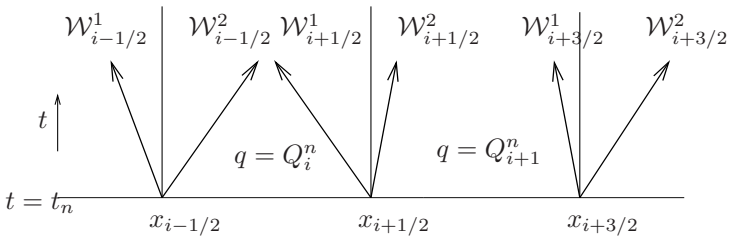

From this point forward, we will assume that we are dealing with piecewise constant averages for the materials in each grid cell and will drop the bar notation.

Consider the interface between the i and $i-1$ cells. We would like to solve the hyperbolic equation $q_t + A(x)q_x = 0$ for 1D acoustics with the following initial data

$$q_0(x) = \begin{cases} q_l & \text{if } x < 0 \\ q_r & \text{if } x > 0 \end{cases} . \tag{3.31}$$

The difference between the averaged state variables at the interface, causes a wave to propagate in each direction. These waves must propagate along the direction of the characteristics in each cell. The right-going wave, or 2-wave, moves in the direction of the right eigenvector of the matrix A_i, while the left-going wave, or 1-wave, moves in the direction of the left eigenvector of the matrix A_{i-1}. This is illustrated in Figure 3.4 for the interface at $x_{i-1/2}$ and $x_{i+1/2}$. Each grid cell has its own material properties and this information is incorporated into the local definition of the flux Jacobian. Therefore, the eigenvalues and eigenvectors are defined using the appropriate values in each grid cell. The difference between q_r and q_l must be the sum of these two waves, so if we can determine the waves, we can calculate the solution q_m.

Since the characteristic directions, or eigenvectors of the system, are known, we need only to determine the amplitude of the waves in order to uniquely determine the solution. Recall that the difference between q_r and q_l is given as the sum of two waves

$$q_r - q_l = \mathcal{W}^1 + \mathcal{W}^2. \tag{3.32}$$

These waves must be eigenvectors of A with some unknown amplitude α,

$$\mathcal{W}^1_{i-1/2} = \alpha^1_{i-1/2} \begin{bmatrix} -\rho_{i-1}c_{i-1} \\ 1 \end{bmatrix} = \alpha^1_{i-1/2} r^1_{i-1}, \tag{3.33}$$

$$\mathcal{W}^2_{i-1/2} = \alpha^2_{i-1/2} \begin{bmatrix} \rho_i c_i \\ 1 \end{bmatrix} = \alpha^2_{i-1/2} r^2_i. \tag{3.34}$$

For the 1D acoustic system, we must solve the following 2×2 system for α

$$\begin{bmatrix} p_i - p_{i-1} \\ u_i - u_{i-1} \end{bmatrix} = \begin{bmatrix} -\rho_{i-1}c_{i-1} & \rho_i c_i \\ 1 & 1 \end{bmatrix} = \begin{bmatrix} \alpha^1_{i-1/2} \\ \alpha^2_{i-1/2} \end{bmatrix}. \tag{3.35}$$

Once the waves are determined, we can find the mid-state q_m of the Riemann problem by solving either

$$q_m \;=\; q_r - \mathcal{W}^2 \quad \text{or} \quad q_m \;=\; q_l + \mathcal{W}^1.$$

These are the basic details for solving a linear hyperbolic system of PDEs and are meant to provide motivation for the eigendecompositions of the model equations in Chapters 4-6. The details of the numerical method and a discussion of the wave propagation algorithm are included in Chapter 7.

Chapter 4

EULER EQUATIONS

The key component in shock wave therapy and lithotripsy is the form of the pressure wave measured at F2 and the focal region. The wave form is highly nonlinear and necessitates the use of a nonlinear system of equations where the sound speed varies with the pressure and density. This allows shocks to develop as illustrated in Figure 2.3. We have followed the example of many other researchers and utilized the Euler equations with either the Tait or Tammann equation of state In order to accurately capture the nonlinear pressure wave at F2. In this chapter we provide an overview of the threee-dimensional form of the equations and the corresponding eigenstructure. As described in Chapter 3, the eigendecomposition of the system is necessary in order to determine the waves and speeds that will update our numerical solution.

The initial condition we used in our calculations consists of a large jump in the pressure and velocity at F1. This can not be accurately modeled by a system derived under the assumption of infinitesimal deformations, so we use the compressible Euler equations to model the initial propagation and steepening of the shock wave. Once it reaches the point in the calculation where both the isentropic and small deformation assumptions are valid, we use the equations of nonlinear elasticity described in the next chapter.

4.1 Compressible Euler Equations

The Euler equations for a compressible inviscid fluid with no thermal conductivity can be written, in the one-dimensional case, as the following system of conservation laws

$$\frac{\partial}{\partial t}q + \frac{\partial}{\partial x}f(q) = 0, \tag{4.1}$$

where

$$q = \begin{bmatrix} \rho \\ \rho u \\ E \end{bmatrix} \text{ and } f(q) = \begin{bmatrix} \rho u \\ \frac{(\rho u)^2}{\rho} + p \\ u(E+p) \end{bmatrix}. \tag{4.2}$$

Here ρ is the fluid density, ρu the linear momentum, with u denoting the velocity along the x axis, $E = \rho e + \frac{1}{2}\rho u^2$ is the total energy per unit volume, e is the internal energy per unit mass and p is the pressure.

4.1.1 Equation of State

In order to solve the system of equations for compressible hydrodynamic flow, we need to close the system with a relation between the pressure and conserved variables. Under the condition of local equilibrium, the pressure can be expressed as a function of two other thermodynamic variables through an appropriate equation of state. We have used the Tait [79] and Tammann [43] equations of state, which are applicable to a wide range of liquids. The Tait equation of state has been more commonly used for shock wave therapy and lithotripsy [70, 60]. This may seem surprising considering the treatment relies upon shock waves to deliver energy and mechanical forces, which are typically non-isentropic processes. The Tammann equation of state is valid for non-isentropic flow and the two equations of state have been shown to be in good agreement in the isentropic flow regime [79].

We thought it important to compare the behavior of the ESWT pressure wave when modeled with both equations of state to insure that we use the correct model.

The Tait equation of state is

$$p = p(\rho) = B\left[\left(\frac{\rho}{\rho_0}\right)^n - 1\right], \tag{4.3}$$

where B is a pressure constant that is a weak function of entropy, but is typically treated as a constant, n is a constant playing a similar role to that of γ in the ideal gas law, ρ is the density, and p the pressure. The values for water at room temperature are $B = 300MPa$ and $n = 7.15$. Table 2.2 contains measured values for different biological type materials and values of the constants for a variety of different fluids can be found in [61].

The Tammann equation of state can be written as

$$p = p(\rho, e) = (\gamma - 1)\rho e - \gamma p_\infty, \tag{4.4}$$

where p,ρ and e are the pressure, density and specific internal energy, respectively. The values in water for the pressure constant, p_c, and polytropic constant, γ, are the same as B and n in the Tait equation of state. This equation is similar to the ideal gas law, and reduces to the ideal gas law in the case where $p_\infty = 0$ and $1 < \gamma < 2$.

Assuming that $(\partial p/\partial\rho)_{s=const} > 0$, as is required for thermodynamic stability, we can introduce the speed of sound c,

$$c = \sqrt{\left.\frac{\partial p}{\partial \rho}\right|_s}, \tag{4.5}$$

where s is the entropy. We will assume the equation of state is convex, which implies the density and pressure of the fluid increase across shock waves. For the Tammann equation of state, the sound speed is $c = \sqrt{\frac{\gamma(p+p_\infty)}{\rho}}$ and for the Tait equation of state, it is $c = \sqrt{\frac{n(p+B)}{\rho}}$.

The Jacobian matrix $A(q) = f'(q)$ of the Euler system is

$$A(q) = \begin{bmatrix} 0 & 1 & 0 \\ \frac{1}{2}(\gamma-3)u^2 & (3-\gamma)u & \gamma - 1 \\ \frac{1}{2}(\gamma-1)u^3 - uH & H - (\gamma-1)u^2 & \gamma u \end{bmatrix}, \tag{4.6}$$

where $H = h + \frac{1}{2}u^2$ is the total specific enthalpy and $h = \frac{e+p}{\rho}$.

This matrix has eigenvalues

$$\lambda^1 = u - c, \quad \lambda^2 = u, \quad \lambda^3 = u + c, \tag{4.7}$$

with right eigenvectors

$$r^1 = \begin{bmatrix} 1 \\ u - c \\ H - uc \end{bmatrix}, \quad r^2 = \begin{bmatrix} 1 \\ u \\ \frac{1}{2}u^2 \end{bmatrix}, \quad r^3 = \begin{bmatrix} 1 \\ u + c \\ H + uc \end{bmatrix}. \tag{4.8}$$

In the case of the Tait equation of state where the pressure can be written as a function of density only, in which case, the energy equation can be eliminated and the above system simplifies to

$$\frac{\partial}{\partial t}\begin{bmatrix} \rho \\ \rho u \end{bmatrix} + \frac{\partial}{\partial x}\begin{bmatrix} \rho u \\ \rho u^2 + p \end{bmatrix} = 0. \tag{4.9}$$

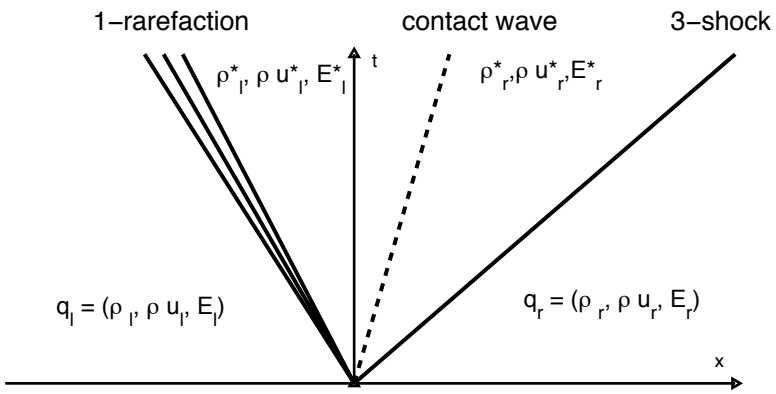

Figure 4.1: Wave diagram showing the structure of a typical solution for the Euler equations.

4.1.2 The Riemann Problem

Recall that the Riemann problem is the initial value problem for a hyperbolic system of conservation laws,

$$q_t + f(q)_x = 0,$$

with special initial data consisting of two constant states separated by a discontinuity

$$q_0(x) = \begin{cases} q_l & \text{if } x < 0 \\ q_r & \text{if } x > 0 \end{cases}.$$

For the eigenstructure of (4.2), we find that the first and third characteristic fields are genuinely nonlinear, while the second field is linearly degenerate. Therefore, the solution of the Riemann problem for the Euler equations will be composed of three waves, where the first and third will either be shocks or rarefactions, and the second will always be a contact discontinuity, see Figure 4.1. Across the contact discontinuity, the pressure and velocity are constant, but there is a jump in the entropy.

The solution to the Riemann problem in 1D for the Tait equation of state consists of two nonlinear waves, corresponding to the two distinct eigenvalues.

4.1.3 Two-Dimensional Euler Equations

In two space dimensions the Euler equations take the form

$$\frac{\partial}{\partial t}q + \frac{\partial}{\partial x}f(q) + \frac{\partial}{\partial y}g(q) = 0, \tag{4.10}$$

with

$$q = \begin{bmatrix} \rho \\ \rho u \\ \rho v \\ E \end{bmatrix}, \quad f(q) = \begin{bmatrix} \rho u \\ \rho u^2 + p \\ \rho uv \\ u(E+p) \end{bmatrix}, \quad g(q) = \begin{bmatrix} \rho v \\ \rho uv \\ \rho u^2 + p \\ v(E+p) \end{bmatrix}. \tag{4.11}$$

Here u and v denote the velocities in the x and y direction, respectively. The total energy is $E = \rho e + \frac{1}{2}(u^2 + v^2)$, and the total enthalpy is $H = h + \frac{1}{2}(u^2 + v^2)$.

The Jacobian $f'(q)$ has four eigenvalues

$$\lambda^1 = u - c, \quad \lambda^{2,3} = u, \quad \lambda^4 = u + c.$$

The sound speed is the same as in one spatial dimension, $c = \sqrt{\gamma p/\rho}$. The eigenvectors in the x direction are

$$r^1 = \begin{bmatrix} 1 \\ u - c \\ v \\ H - uc \end{bmatrix}, \quad r^2 = \begin{bmatrix} 1 \\ u \\ v \\ \frac{1}{2}(u^2 + v^2) \end{bmatrix}, \quad r^3 = \begin{bmatrix} 0 \\ 0 \\ 1 \\ v \end{bmatrix}, \quad r^4 = \begin{bmatrix} 1 \\ u + c \\ v \\ H + uc \end{bmatrix}.$$

The two distinct eigenvalues λ^1 and λ^4 give genuinely nonlinear fields, while the eigenvalue of multiplicity 2, $\lambda^2 = \lambda^3 = u$, correspond to linearly degenerate fields. If we consider a plane-wave Riemann problem in the x-direction, where data only vary along x, then the solution consists of at most four constant states separated by three waves. The waves corresponding to the genuinely nonlinear fields will either be shocks or rarefactions. There will also be a contact discontinuity with speed u that carry a jump in entropy and a shear wave that carries a jump in the tangential velocity v. The pressure and normal velocity will not vary across the contact discontinuity.

The 2D isentropic Euler equations are the same as the 2D Euler equations (4.10) without the energy equation. The solution to the Riemann problem for this system consists of two nonlinear waves, shocks or rarefactions, and a contact discontinuity. The nonlinear waves carry jumps in the normal velocity and density. The contact discontinuity carries a jump in the tangential velocity, but no jump in the entropy since we have assumed the entropy is small enough to be neglected. The 2D case is illustrated in Figure 4.1.3.

4.1.4 Three-Dimensional Euler Equations with Axial Symmetry

Several of the problems we investigated are axially symmetric and this enabled us to reduce the three-dimensional equations to a two-dimensional form. If we first rewrite the equations in cylindrical coordinates (r, θ, z) and then assume no variation and zero velocity in the θ direction, the system we obtain is reduced to two variables, r and z.

$$\frac{\partial}{\partial t}\begin{bmatrix} \rho \\ \rho u_r \\ \rho u_v \\ E \end{bmatrix} + \frac{\partial}{\partial r}\begin{bmatrix} \rho u_r \\ \rho u_r^2 + p \\ \rho u_r w_z \\ u_r(E+p) \end{bmatrix} + \frac{\partial}{\partial z}\begin{bmatrix} \rho w_z \\ \rho u_r w_z \\ \rho w_z^2 + p \\ w_z(E+p) \end{bmatrix} = \begin{bmatrix} -(\rho u_r)/r \\ -(\rho u_r^2)/r \\ -(\rho u_r v_z) \\ u_r(E+p)/r \end{bmatrix},$$

where u_r and w_z denote the velocities in the r and z directions, respectively. These equations are of the same form as (4.10), with the addition of geometric source terms that are a result of the variable transformation.

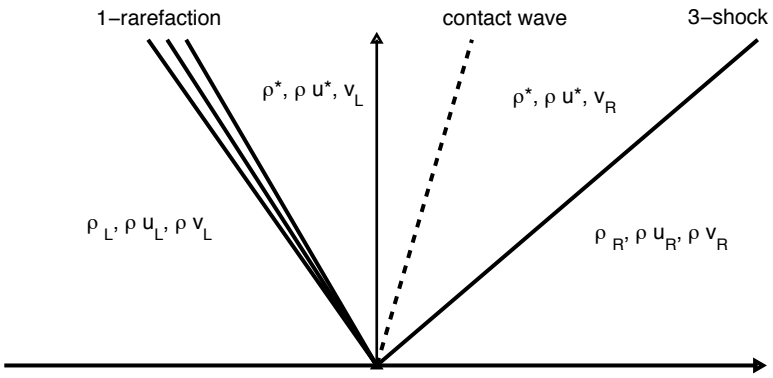

Figure 4.2: Wave diagram showing solution to the Riemann problem for the 2D isentropic Euler equations with the Tait equation of state.

4.2 Validity of Isentropic Flow in ESWT

In the case of Isentropic flow the equations are simpler because the energy can be excluded. This is not usually the case when dealing with shocks because it is well-known that entropy must increase across a shock [79, 51]. However, in the event that the shock is weak, or there is only a very small change in the entropy, an equation of state that only depends on the density, such as the Tait equation of state, can be used. Several studies have indicated that in ESWT, there is no significant change in density or pressure as a result of the change of entropy across the shock [61] for pressures ranging from $1 - 200$ MPa. This indicates that the use of the Tait equation of state should be sufficient for the study of ESWT.

We performed a numerical investigation of the propagation of the pressure wave when modeled by both the Tammann and Tait equation of state, and determined there was no significant difference between the two. Figure 4.3 shows the result from one experiment where a shock wave with peak over pressure of ≈ 180 MPa has propagated through water. The blue wave represents the result from solving with the Tammann equation of state and the red represents the solution with the Tait equation of state, the pressure profiles are nearly identical. This gives us confidence that the calculations we are interested in can be done using the isentropic form of the Euler equations with the Tait equation of state.

4.2.1 Shock Strength

In addition to the numerical investigation of the equivalence of the two equations of state, we also considered the Mach number for the flow and shock strength parameter Π derived by Thompson [79].

The strength of the shock can be investigated by considering the Mach number for different pressures, which is defined as the ratio between the speed of the object propagating through the fluid and the speed of sound in the material at rest, $M = \frac{u}{c_0}$. The strength of the shock increases with M. Figure 4.2.1 shows a plot of the Mach number as a function of the pressures typically seen

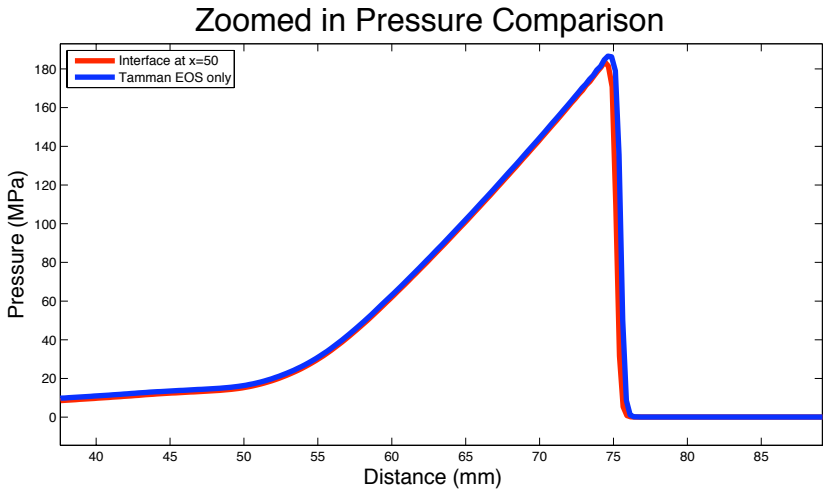

Figure 4.3: Comparison of a pressure wave calculation performed using both the Tait and Tammann equations of state. The results are nearly identical.

in shock wave therapy.

Thompson [79] defines the following quantity, Π as the shock strength

$$\Pi = \frac{[p]}{\rho_1 c_1^2},$$

where $[p]$ is the jump in pressure across the shock. If

$$\Pi \ll 1 \Rightarrow \text{weak shock (essentially isentropic or change in entropy is small)},$$
$$\Pi \gg 1 \Rightarrow \text{strong shock (non-isentropic)}.$$

The entropy across a weak shock is $O(\Pi^3)$, so when $\Pi << 1$, the entropy is also very small. The justification for this depends upon using Taylor expansions of enthalpy and specific volume within the Rankine-Hugoniot condition and can be found in [79].

The typical pressures found in ESWL and ESWT range from 10-100 MPa. We are interested in determining whether or not these pressures are great enough to lead to strong shocks, or a large jump in entropy across the shock. In the case of non-isentropic behavior, we must use the full Euler equations to model the wave propagation in the fluid.

Table 4.1: Shock Strength in Water

Pressure (MPa)	Shock Strength
10	0.007
50	0.033
100	0.068
200	0.136

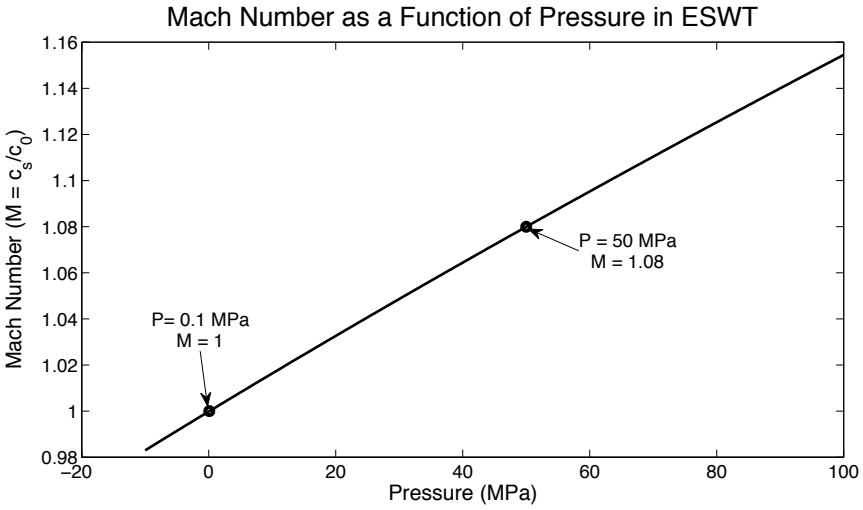

The speed of sound for water under a pressure of 1 atmosphere or 0.1 MPa, is $1,500 m/s$, and has a density of $1,000 kg/m^3$. If we use this in the shock strength criteria above, we find that for a shock wave with a peak pressure of 50 MPa, $\Pi = 0.0034$, which is much less than one. Table 4.1 summarizes the results for the range of values that we are concerned with in our experiments. It is clear that for values up to 100 MPa, the shock strength will be much less than 1, so the change in entropy across the shock is small and our flow can be modeled as isentropic. This is less accurate as the pressure increases even to 200 MPa. It is generally considered that the Tait and Tammann equations of state will agree up to 100 MPa [79]. We have also tested this hypothesis numerically using the Tait and Tammann equations of state which showed good agreement up to 180 MPa, see Figure 4.3.

Chapter 5

LINEAR ELASTICITY

In this chapter we give a brief description of the 3D numerical method and solutions to the Riemann problems for heterogeneous linear elasticity. The equations for linear elasticity are used for validation of the model when comparing the results of laboratory experiments to numerical calculations, as well as for our model of the bone. In particular, the acrylic cylinders described in Chapter 9 were modeled as linear, isotropic elastic solids. As discussed in Chapter 2, bone, especially cortical bone, behaves like a linearly elastic solid [33]. Nonunions typically occur in the long shaft of the bone which is mostly comprised of cortical bone. Therefore, when we investigated the behavior of the shock wave with bone geometries, we modeled them as isotropic, linearly elastic materials.

5.1 Three-Dimensional Elasticity Equations

The elasticity equations may be written in conservation law form, which in three space dimensions looks like

$$\frac{\partial}{\partial t}q(x,y,z,t) + \frac{\partial}{\partial x}f(q(x,y,z,t)) + \frac{\partial}{\partial y}g(q(x,y,z,t)) + \frac{\partial}{\partial z}h(q(x,y,z,t)) = 0, \tag{5.1}$$

where q is a vector of state variables, f,g,and h are the flux functions in the x, y and z directions, respectively.

A complete derivation of the equations of motion in an elastic solid can be found in, for example, [40]. For the purposes of this work, we will just state the following equations for the momenta

$$\rho\frac{\partial^2}{\partial t^2}\delta_i = \sigma_{ij} \quad i = 1,2,3; \quad j = 1,2,3 \tag{5.2}$$

that are a result of Newton's second law and relate the particle displacements $\delta = (\delta_1, \delta_2, \delta_3)$ to the stresses $\sigma^{11}, \sigma^{22}, \sigma^{33}, \sigma^{12}, \sigma^{23}, \sigma^{13}$. Here ρ is the density of the material. Note that the particle velocities can be written as the time derivative of the displacement

$$u_i = \frac{\partial}{\partial t}\delta_i, \tag{5.3}$$

where u_i and δ_i are the velocity and displacement in the i-th direction, respectively. So the above equations for the momenta can also be written as first-order equations in terms of the velocities as

$$\rho\frac{\partial}{\partial t}u_i = \sigma_{ij} \quad i = 1,2,3; \quad j = 1,2,3. \tag{5.4}$$

In order to solve equation (5.4), we need a constitutive equation that relates the stresses to the displacements. The simplest form of the constitutive equation assumes a linear relationship between the stress and strain, this is known as Hooke's law. For an isotropic, linear elastic material, Hooke's

law is

$$\begin{bmatrix} \sigma_{11} \\ \sigma_{22} \\ \sigma_{33} \\ \sigma_{12} \\ \sigma_{23} \\ \sigma_{13} \end{bmatrix} = \begin{bmatrix} \lambda+2\mu & \lambda & \lambda & 0 & 0 & 0 \\ \lambda & \lambda+2\mu & \lambda & 0 & 0 & 0 \\ \lambda & \lambda & \lambda+2\mu & 0 & 0 & 0 \\ 0 & 0 & 0 & 2\mu & 0 & 0 \\ 0 & 0 & 0 & 0 & 2\mu & 0 \\ 0 & 0 & 0 & 0 & 0 & 2\mu \end{bmatrix} \begin{bmatrix} \epsilon_{11} \\ \epsilon_{22} \\ \epsilon_{33} \\ \epsilon_{12} \\ \epsilon_{23} \\ \epsilon_{13} \end{bmatrix}. \tag{5.5}$$

Here λ and μ are the Lamé constants, $\kappa = (\lambda + 2\mu)$ where κ is the bulk modulus of the material and μ is the shear modulus.

The relationship between the strain and displacements in the case of infinitessimal strain can be written as

$$\epsilon_{ij} = \frac{1}{2}\left(\frac{\partial u_i}{\partial x_j} + \frac{\partial u_j}{\partial x_i}\right). \tag{5.6}$$

If we combine the equations (5.4-5.6) we get the following system for three-dimensional linear elasticity,

$$\begin{aligned} \sigma_t^{11} - (\lambda+2\mu)u_x - \lambda v_y - \lambda w_z &= 0 \\ \sigma_t^{22} - \lambda u_x - (\lambda+2\mu)v_y - \lambda w_z &= 0 \\ \sigma_t^{33} - \lambda u_x - \lambda v_y - (\lambda+2\mu)w_z &= 0 \\ \sigma_t^{12} - \mu(v_x + u_y) &= 0 \\ \sigma_t^{23} - \mu(v_z + w_y) &= 0 \\ \sigma_t^{31} - \mu(u_z + w_x) &= 0 \\ \rho u_t - \sigma_x^{11} - \sigma_y^{12} - \sigma_z^{13} &= 0 \\ \rho v_t - \sigma_x^{12} - \sigma_y^{22} - \sigma_z^{23} &= 0 \\ \rho w_t - \sigma_x^{13} - \sigma_y^{23} - \sigma_z^{33} &= 0 \end{aligned} \tag{5.7}$$

Note that when λ and μ vary spatially, these equations are no longer conservative. However, in our numerical method we define the solution to these equations locally on each grid cell where λ and μ are constant, so we can perform the following analysis assuming conservation form.

This system (5.7) can be written as

$$q_t + Aq_x + Bq_y + Cq_z = 0 \tag{5.8}$$

where

$$q = \begin{bmatrix} \sigma^{11} \\ \sigma^{22} \\ \sigma^{33} \\ \sigma^{12} \\ \sigma^{23} \\ \sigma^{31} \\ u \\ v \\ w \end{bmatrix}, A = \begin{bmatrix} 0 & 0 & 0 & 0 & 0 & 0 & -(\lambda+2\mu) & 0 & 0 \\ 0 & 0 & 0 & 0 & 0 & 0 & -\lambda & 0 & 0 \\ 0 & 0 & 0 & 0 & 0 & 0 & -\lambda & 0 & 0 \\ 0 & 0 & 0 & 0 & 0 & 0 & 0 & \mu & 0 \\ 0 & 0 & 0 & 0 & 0 & 0 & 0 & 0 & 0 \\ 0 & 0 & 0 & 0 & 0 & 0 & 0 & 0 & \mu \\ -1/\rho & 0 & 0 & 0 & 0 & 0 & 0 & 0 & 0 \\ 0 & 0 & 0 & -1/\rho & 0 & 0 & 0 & 0 & 0 \\ 0 & 0 & 0 & 0 & 0 & -1/\rho & 0 & 0 & 0 \end{bmatrix} \tag{5.9}$$

B and C have a similar structure with nonzero entries in different locations [51]. The matrices A,B and C do not commute so the equations are usually coupled in the multidimensional case. Recall that the system is hyperbolic if the matrices A, B, C, and any linear combination of them are diagonalizable with real eigenvalues and a complete set of linearly independent eigenvectors.

5.1.1 Eigenstructure for linear elasticity

In the spatially-homogeneous isotropic case, the matrices A, B and C have nine eigenvalues that correspond to the wave speeds of two P-waves (c_p), four S-waves (c_s) and three zero-speed waves. The eigenvalues are

$$\lambda^{1,2} = \pm c_p, \quad \lambda^{3,4} = \pm c_s, \quad \lambda^{5,6} = \pm c_s, \text{ and } \lambda^{7,8,9} = 0. \tag{5.10}$$

Where $c_p = \sqrt{\frac{\lambda+2\mu}{\rho}}$ and $c_s = \sqrt{\frac{\mu}{\rho}}$. In the heterogeneous case, each of the material properties λ, μ and ρ may vary spatially. As mentioned in Chapter 3, in this case the waves and speeds are determined locally by the material properties of each grid cell. The equations are still hyperbolic assuming the criteria for hyperbolicity is met at any given point (x, y, z).

The right eigenvectors for the matrix A are

$$r^{1,2} = \begin{bmatrix} \lambda+2\mu \\ \lambda \\ \lambda \\ 0 \\ 0 \\ 0 \\ \pm c_p \\ 0 \\ 0 \end{bmatrix}, r^{3,4} = \begin{bmatrix} 0 \\ 0 \\ 0 \\ \mu \\ 0 \\ 0 \\ 0 \\ \pm c_s \\ 0 \end{bmatrix}, r^{5,6} = \begin{bmatrix} 0 \\ 0 \\ 0 \\ 0 \\ 0 \\ \mu \\ 0 \\ 0 \\ \pm c_s \end{bmatrix}, r^{7} = \begin{bmatrix} 0 \\ 0 \\ 0 \\ 0 \\ 1 \\ 0 \\ 0 \\ 0 \\ 0 \end{bmatrix}, r^{8} = \begin{bmatrix} 0 \\ 1 \\ 0 \\ 0 \\ 0 \\ 0 \\ 0 \\ 0 \\ 0 \end{bmatrix}, r^{9} = \begin{bmatrix} 0 \\ 0 \\ 1 \\ 0 \\ 0 \\ 0 \\ 0 \\ 0 \\ 0 \end{bmatrix}.$$

The eigenvectors for the B and C matrices are similar, but the entries are shifted.

5.1.2 Solution to Riemann problem

Recall that we were interested in solving the linear system $R\alpha = \Delta Q$ to get the coefficients α^p of the eigenvectors which are used to construct the waves $\mathcal{W}^p$ in order to solve the Riemann problem. This is a straightforward process and can be done exactly in the linear case. Consider the Riemann problem in the x-coordinate direction. The structure of the solution to this problem will consist of 9 waves. Three of these waves will have speed zero and correspond to jumps in σ^{12}, σ^{23}, and σ^{13} each of which causes no propagation in the x-direction. Two are P-waves with speed $\pm c_p$ in the x-direction. The other four waves S-waves with speed $\pm c_s$ in the xy- and xz- directions. The solution will be similar in each of the coordinate directions.

5.2 Axisymmetric Elasticity

We use the two-dimensional axisymmetric equations for linear elasticity to compute the solution for comparison against the three-dimensional calculations. The equations and eigenstructure are included here.

5.2.1 Equations

The two-dimensional axisymmetric equations in elasticity are derived in a similar manner to the Euler equations from Chapter 4. The full three-dimensional system is first written in cylindrical coordinates and then reduced by assuming no variation and zero velocity in the θ-direction. For

brevity, I will just write the final two-dimensional system here

$$\frac{\partial}{\partial t}\begin{bmatrix}\sigma^{rr}\\ \sigma^{\theta\theta}\\ \sigma^{zz}\\ \sigma^{rz}\\ \rho u\\ \rho v\end{bmatrix} - \frac{\partial}{\partial r}\begin{bmatrix}(\lambda+2\mu)u_r\\ \lambda u_r\\ \lambda u_r\\ \mu u_z\\ \sigma^{rr}\\ \sigma^{rz}\end{bmatrix} - \frac{\partial}{\partial z}\begin{bmatrix}\lambda u_z\\ \lambda u_z\\ (\lambda+2\mu)u_z\\ \mu u_r\\ \sigma^{rz}\\ \sigma^{zz}\end{bmatrix} = \begin{bmatrix}\frac{\lambda u_r}{r}\\ \frac{(\lambda+2\mu)u_r}{r}\\ \frac{\lambda u_r}{r}\\ 0\\ \frac{\sigma^{rr}-\sigma^{\theta\theta}}{r}\\ \frac{\sigma_{rz}}{r}\end{bmatrix} \tag{5.11}$$

5.2.2 Eigenstructure

The flux-Jacobian in the x-direction in this case is

$$A = -\begin{bmatrix}0 & 0 & 0 & 0 & \lambda+2\mu & 0\\ 0 & 0 & 0 & 0 & \lambda & 0\\ 0 & 0 & 0 & 0 & \lambda & 0\\ 0 & 0 & 0 & 0 & 0 & \mu\\ 1/\rho & 0 & 0 & 0 & 0 & 0\\ 0 & 0 & 0 & 1/\rho & 0 & 0\end{bmatrix}. \tag{5.12}$$

The eigenvalues are

$$\lambda^{1,2} = \pm\sqrt{\frac{\lambda+2\mu}{\rho}} = \pm c_p, \quad \lambda^{3,4} = \pm\sqrt{\frac{\mu}{\rho}} = \pm c_s, \quad \lambda^{5,6} = 0, \tag{5.13}$$

with corresponding right eigenvectors

$$r^{1,2} = \begin{bmatrix}\lambda+2\mu\\ \lambda\\ \lambda\\ \pm c_p\\ 0\\ 0\end{bmatrix},\ r^{3,4} = \begin{bmatrix}0\\ 0\\ 0\\ \mu\\ 0\\ \pm c_s\end{bmatrix},\ r^5 = \begin{bmatrix}0\\ 1\\ 0\\ 0\\ 0\\ 0\end{bmatrix},\ r^6 = \begin{bmatrix}0\\ 0\\ 1\\ 0\\ 0\\ 0\end{bmatrix}.$$

5.3 Determination of Principal Stresses

In order to calculate the maximum and minimum stresses during the calculations in Chapters 9 and 10, as well as the values needed for the photoelastic calculations in Chapter 8, it is important to calculate the principal stresses in each grid cell after every time step. The principal stresses are the components of the stress tensor when the basis is changed in such a way that the shear stress components are zero.

In the case of two-dimensional elasticity, we calculate the eigenvalues (σ_1, σ_2) of the 2×2 stress tensor

$$\sigma = \begin{bmatrix}\sigma^{11} & \sigma^{12}\\ \sigma^{12} & \sigma^{22}\end{bmatrix}, \tag{5.14}$$

to obtain the maximum compressive stress $\max(\sigma_1, \sigma_2)$ and maximum tensile stress $\min(\sigma_1, \sigma_2)$.

The eigenvalues are

$$\sigma_1 = \frac{\sigma^{11}+\sigma^{22}}{2} + \sqrt{\left(\frac{\sigma^{11}-\sigma^{22}}{2}\right)^2 + (\sigma^{12})^2}$$
$$\sigma_2 = \frac{\sigma^{11}+\sigma^{22}}{2} - \sqrt{\left(\frac{\sigma^{11}-\sigma^{22}}{2}\right)^2 + (\sigma^{12})^2}. \tag{5.15}$$

The maximum shear stress is given by $\sigma^s_{max} = \frac{\sigma_1-\sigma_2}{2}$. In our calculations, we checked these relations by numerically calculating the eigenvalues of the stress tensor.

The principal stresses in three dimensions are again given by the eigenvalues of the 3×3 stress tensor

$$\sigma_1 = \frac{I_1}{3} + \frac{2}{3}\left(\sqrt{I_1^2 - 3I_2}\right)\cos\phi$$
$$\sigma_2 = \frac{I_1}{3} + \frac{2}{3}\left(\sqrt{I_1^2 - 3I_2}\right)\cos\left(\phi + \frac{2\pi}{3}\right)$$
$$\sigma_3 = \frac{I_1}{3} + \frac{2}{3}\left(\sqrt{I_1^2 - 3I_2}\right)\cos\left(\phi + \frac{4\pi}{3}\right) \tag{5.16}$$
$$\tag{5.17}$$

where

$$I_1 = \sigma^{11} + \sigma^{22} + \sigma^{33},$$
$$I_2 = \sigma^{11}\sigma^{22} + \sigma^{22}\sigma^{33} + \sigma^{33}\sigma^{11} - (\sigma^{12})^2 - (\sigma^{23})^2 - (\sigma^{13})^2,$$
$$I_3 = \sigma^{11}\sigma^{22}\sigma^{33} - \sigma^{11}(\sigma^{23})^2 - \sigma^{33}(\sigma^{12})^2 + 2\sigma^{12}\sigma^{23}\sigma^{13}, \tag{5.18}$$

and

$$\phi = \frac{1}{3}\cos^{-1}\left(\frac{2I_1^3 - 9I_1I_2 + 27I_3}{2(I_1^2 - 3I_2)^{3/2}}\right). \tag{5.19}$$

The quantities I_1, I_2, and I_3 are known as the stress invariants.

The principal stress directions are the eigenvectors associated with each of the eigenvalues.

Chapter 6

LAGRANGIAN FORM OF THE EULER EQUATIONS

In this chapter I present the details of the equations that we solve in our model of ESWT. The linear elasticity equations are not sufficient because they do not capture the nonlinear steepening effects of the fluid. The Euler equations can model the steepening of the wave into a shock, but can not be used to determine the shear stresses in the solid, which may be important for healing. As was demonstrated in Chapter 4, the isentropic Euler equations are valid and this, combined with the small size of the displacements in the fluid, allows us to use the same equations in both the fluid and solid. It should be noted here that the computational grid is not moving with the flow, but we are still modeling the displacements of the fluid and solid particles as a result of the pressure wave, so the fluid and bone are not stationary. In this chapter we provide details on the equations and the structure of the solution to the Riemann problem.

6.1 One-dimensional form of the equations

6.1.1 Equivalence of Lagrangian formulation with Nonlinear Elasticity

The Lagrangian form for Euler's equations of gas or hydro dynamics uses a coordinate system that moves with the velocity field of the fluid. The equations can be written as

$$\rho \frac{dq}{dt} + \nabla_x f = 0 \tag{6.1}$$

where

$$q = \begin{pmatrix} \eta \\ u \\ E \end{pmatrix}, f = \begin{pmatrix} -u \\ p \\ pu \end{pmatrix}. \tag{6.2}$$

Here ρ is the density, $\eta = 1/\rho$ is the specific volume, u the velocity in the x-direction, $E = e + 0.5u^2$ the total energy density, e the internal energy density and $p = p(\rho, e)$ the pressure given by an appropriate equation of state.

The system (6.1) is written in non-conservative form and some work has been done to develop schemes to solve these equations numerically [75]. We are interested in equations that are written in conservation form, and the one-dimensional system can be written this way if we introduce the Lagrangian mass coordinate $m = \int_{x_0}^{x_1} \rho dx$, so the above equations become

$$\begin{aligned} \eta_t - u_m &= 0 \\ u_t - p_m &= 0 \\ E_t - (pu)_m &= 0. \end{aligned} \tag{6.3}$$

Some work has been done on developing numerical methods for this form of the equations, but it is unclear how to define an appropriate mass coordinate in higher-dimensions [59]. An alternative approach exists if we can assume that the displacements in our model are small so that $\rho(t) \approx \rho_0$, that is the original density does not change over time.

Let $X(a, t)$ be the current position of the fluid particle that was initially at $X(a, 0)$. Following [75] we can think of the velocity u as effecting a coordinate transformation from the reference

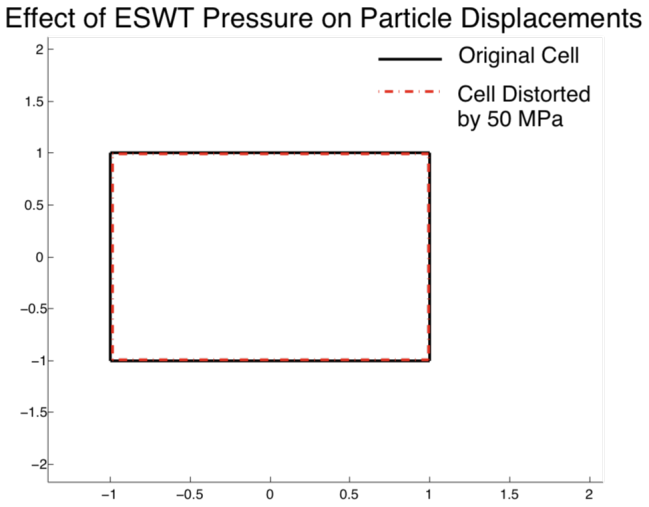

Figure 6.1: The displacement of the grid due to the pressure wave in ESWT compared to the initial computational grid. There is virtually no difference between the two, which supports our use of ρ_0 throughout the calculation.

configuration in a to the current configuration X with jacobian $j(a,t) = X'(a,t)$.

If we take an interval (a_1, a_2), then at time t it has become $(X_1(a_1,t), X_2(a_2,t))$. For any function $g(X,t)$

$$\int_{X_1}^{X_2} g(X,t)dX = \int_{a_1}^{a_2} g(a,t)j(a,t)da. \tag{6.4}$$

We can apply this integral operator to the differential equations above to get,

$$\int_{a_1}^{a_2} \rho(a,t)q_t(a,t)j(a,t)da = -(f(a_2) - f(a_1)). \tag{6.5}$$

If we divide both sides by $\Delta a = a_2 - a_1$, and take the limit Δa goes to 0, we get

$$\rho(a,t)j(a,t)q_t(a,t) = -f(q)_a. \tag{6.6}$$

Which is equivalent to

$$\rho_0 q_t(a,t) = -f(q)_a. \tag{6.7}$$

Thus, in the reference configuration, we can relate the current velocity to the change in pressure using the original background density, ρ_0. In our numerical method, the reference configuration a is equivalent to the cartesian grid where we are performing our calculations. Consider the diagram in Figure 6.1, the grid where the calculations are being performed is plotted against one that is being displaced by the ESWT pressure wave. As you can see, there is virtually no difference between the two.

Given that $\rho \approx \rho_0$, the system 6.1 becomes

$$\begin{aligned} \rho_0 \eta_t &= u_x \\ \rho_0 u_t &= -p_x \\ \rho_0 E_t &= -(pu)_x. \end{aligned} \tag{6.8}$$

Let ϵ be the strain tensor and F the deformation gradient tensor, then it is well-known that in the case of small displacements

$$\rho = \frac{\rho_0}{det(F)} = \frac{\rho_0}{1 + \epsilon^{11}}. \tag{6.9}$$

Then this is related to the specific volume by

$$\eta = \frac{1}{\rho} = \frac{1 + \epsilon^{11}}{\rho_0}. \tag{6.10}$$

If we take the derivative with respect to time of both sides we get $\eta_t = \frac{\epsilon_t}{\rho_0}$. Making this substitution in system (6.8) we have

$$\begin{aligned} \rho_0 (\frac{\epsilon}{\rho_0})_t - u_x &= 0 \\ \rho_0 u_t + p_x &= 0 \\ \rho_0 E_t + (pu)_x &= 0. \end{aligned} \tag{6.11}$$

We can further simplify this system by assuming an isentropic equation of state, where the pressure is independent of energy. This eliminates the last equation of (6.11). Now, since ρ_0 is constant in time, we can rewrite the first equation as $\epsilon_t - u_x = 0$, and it is clear that this system is equivalent to the equations for nonlinear elasticity. Thus, we can use this system to model both the wave propagation in both the fluid and the solid. The difference in materials is incorporated through the equation of state, or equivalently, the stress-strain relationship. A method for solving systems of hyperbolic equations with spatially-varying stress-strain relationships using f-waves was presented in [52]. We utilize this same approach to construct the waves and speeds for our solution.

6.1.2 Waves and speeds

The first step in determining the numerical solution to this system is to calculate the waves and speeds that will be used in the solution of the Riemann problem.

Isentropic Euler Equations

For the system in the previous section, we get the following for the Jacobian

$$f'(q) = -\begin{pmatrix} 0 & 1/\rho_0 \\ \sigma_{\epsilon^{11}} & 0 \end{pmatrix}. \tag{6.12}$$

The characteristic equation for 6.12 is

$$[-\lambda[\lambda^2 - \lambda + \frac{1}{\rho_0}\sigma_{\epsilon^{11}}]] = 0. \tag{6.13}$$

Therefore the eigenvalues for the Jacobian are

$$\lambda_1 = 0, \quad \lambda_{2,3} = \pm\sqrt{\frac{\sigma_{\epsilon^{11}}}{\rho_0}}. \tag{6.14}$$

In the case of the Euler equations with the Tait equation of state, $p(\rho) = p(\epsilon) = B[(\frac{1}{(1+\epsilon)}^{\gamma} - 1]$, we get the following

$$\begin{aligned} \sigma_{\epsilon^{11}} &= B\gamma\left(\frac{1}{(1+\epsilon)}\right)^{\gamma+1} \\ &= B\gamma\frac{1}{(1+\epsilon)}\left(\frac{1}{(1+\epsilon)}\right)^{\gamma} \\ &= \frac{1}{(1+\epsilon)}\gamma(p+B). \end{aligned} \tag{6.15}$$

If we use this and the assumption that $\rho(t) \approx \rho_0$ in our formula for the eigenvalues (6.15), we get the following for our wave speeds

$$\pm\sqrt{\frac{\gamma(p+B)}{\rho_0}}. \tag{6.16}$$

These are equivalent to the acoustic wave speeds in the standard form of the isentropic Euler equations.

Linear Elasticity

For elasticity if we assume that the density ρ is constant throughout a specific material, but can still vary spatially, and denote it ρ_0, then the eigenvalues are

$$\lambda^{1,2} = \left[\pm\sqrt{-\frac{\sigma_{\epsilon^{11}}}{\rho_0}}\right], \tag{6.17}$$

where $\sigma_{\epsilon^{11}} = (\lambda + 2\mu)$. This means that we have

$$\lambda^{1,2} = \pm\sqrt{\frac{\lambda+2\mu}{\rho_0}}, \tag{6.18}$$

the correct sound speeds in a linearly elastic material.

Eigenvectors

The eigenvectors for system (6.8) are

$$r^{1,2} = \begin{pmatrix} 1 \\ \pm\sqrt{\sigma_{\epsilon^{11}}\rho_0} \end{pmatrix}. \tag{6.19}$$

F-wave Decomposition

Now, if we want to compute the waves for the solution to our Riemann problem using an f-wave type approach, we must solve the following system for β in order to get the coefficients for our waves

$$R\beta = f_i(Q_i) - f_{i-1}(Q_{i-1}), \tag{6.20}$$

where R is the matrix of eigenvectors (6.19) and $f_j(Q_j)$ is the locally defined flux in the j-th grid cell.

6.2 Two-dimensional form of the equations

$$\begin{aligned} \epsilon_t^{11} - u_x &= 0 \\ \epsilon_t^{22} - v_y &= 0 \\ \epsilon_t^{12} - \frac{1}{2}(u_y + v_x) &= 0 \\ \rho_0 u_t - \sigma_x^{11} - \sigma_y^{12} &= 0 \\ \rho_0 v_t - \sigma_y^{22} - \sigma_x^{12} &= 0. \end{aligned} \tag{6.21}$$

The Jacobian for the x-direction is the following:

$$f'(q) = -\begin{pmatrix} 0 & 0 & 0 & 1/\rho_0 & 0 \\ 0 & 0 & 0 & 0 & 0 \\ 0 & 0 & 0 & 0 & \frac{1}{2\rho_0} \\ \sigma^p_{\epsilon^{11}} & \sigma^p_{\epsilon^{22}} & 0 & 0 & 0 \\ 0 & 0 & \sigma^s_{\epsilon^{12}} & 0 & 0 \end{pmatrix}. \tag{6.22}$$

Here σ^p is the compressional stress and σ^s the shear stress. We have made use of the fact that the derivative of σ^p with respect to the shear strain will be zero in either the Euler or elastic equations. Similarly, the derivative of σ^s will be zero except in the case of the shear strain ϵ_{12} due to the form of the stress-strain relationship in elasticity and fluids do not support shear stresses.

6.2.1 Eigenstructure

The eigenvalues for system (6.22) are

$$\lambda^{1,2} = \left(\pm\sqrt{\frac{\sigma^p_{\epsilon^{11}}}{\rho_0}}\right); \quad \lambda^{3,4} = \pm\sqrt{\frac{\sigma^s_{\epsilon^{12}}}{2\rho_0}}; \quad \lambda^5 = 0. \tag{6.23}$$

The corresponding eigenvectors for system (6.22) are

$$\begin{pmatrix} 1 \\ 0 \\ 0 \\ \sqrt{\rho_0\sigma^p_{\epsilon_{11}}} \\ 0 \end{pmatrix}, \begin{pmatrix} 1 \\ 0 \\ 0 \\ -\sqrt{\rho_0\sigma^p_{\epsilon_{11}}} \\ 0 \end{pmatrix}, \begin{pmatrix} 0 \\ 0 \\ 1 \\ 0 \\ \pm\sqrt{2\rho_0\sigma^s_{\epsilon^{12}}} \end{pmatrix} \begin{pmatrix} -\frac{\sigma^p_{\epsilon^{11}}}{\sigma^p_{\epsilon^{22}}} \\ 1 \\ 0 \\ 0 \\ 0 \end{pmatrix}. \tag{6.24}$$

The weights that we need to determine the wave strengths in the wave propagation algorithm found by solving $R\beta = f(Q_r) - f(Q_l)$ are found by solving

$$\begin{pmatrix} 1 & 0 & 1 & 0 & 1 \\ 0 & 0 & \frac{\sigma^p_{\epsilon^{11}}}{\sigma^p_{\epsilon^{22}}} & 0 & 0 \\ 0 & 1 & 0 & 1 & 0 \\ -\lambda^1 & 0 & 0 & 0 & -\lambda^2 \\ 0 & -\sqrt{2\sigma_{\epsilon^{12}}} & 0 & \sqrt{2\sigma_{\epsilon^{12}}} & 0 \end{pmatrix} \begin{pmatrix} \beta^1 \\ \beta^2 \\ \beta^3 \\ \beta^4 \\ \beta^5 \end{pmatrix} = \begin{pmatrix} f^1 \\ f^2 \\ f^3 \\ f^4 \\ f^5 \end{pmatrix}. \tag{6.25}$$

Solving system (6.25) for β gives

$$\begin{aligned}
\beta^1 &= \frac{(f^1\lambda^2 + f^4)}{(\lambda^2 - \lambda^1)} \\
\beta^2 &= \frac{(f^1\lambda^1 + f^4)}{(\lambda^2 - \lambda^1)} \\
\beta^3 &= 0 \\
\beta^5 &= \frac{f^5 + \lambda^4 f^3}{\lambda^4 - \lambda^5} \\
\beta^6 &= \frac{-f^3\lambda^5 - f^5}{\lambda^4 - \lambda^5}.
\end{aligned} \tag{6.26}$$

6.3 Three-dimensional equations

The full three-dimensional system of equations for the Isentropic Euler equations in Lagrangian coordinates is

$$\begin{aligned}
(\epsilon_{11})_t &= \frac{\partial u}{\partial x} \\
(\epsilon_{22})_t &= \frac{\partial v}{\partial y} \\
(\epsilon_{33})_t &= \frac{\partial w}{\partial z} \\
(\epsilon_{12})_t &= \frac{1}{2}\frac{\partial u}{\partial y} + \frac{\partial v}{\partial x} \\
(\epsilon_{23})_t &= \frac{1}{2}\frac{\partial v}{\partial z} + \frac{\partial w}{\partial y} \\
(\epsilon_{13})_t &= \frac{1}{2}\frac{\partial u}{\partial z} + \frac{\partial w}{\partial x} \\
\rho u_t &= \frac{\partial \sigma_{12}}{\partial y} + \frac{\partial \sigma_{11}}{\partial x} + \frac{\partial \sigma_{13}}{\partial z} \\
\rho v_t &= \frac{1}{r}\frac{\partial \sigma_{22}}{\partial y} + \frac{\partial \sigma_{12}}{\partial x} + \frac{\partial \sigma_{23}}{\partial z} \\
\rho w_t &= \frac{1}{r}\frac{\partial \sigma_{23}}{\partial y} + \frac{\partial \sigma_{33}}{\partial z} + \frac{\partial \sigma_{13}}{\partial x}.
\end{aligned} \tag{6.27}$$

The corresponding Jacobian for this system in the x-direction is

$$f'(q) = -\begin{pmatrix}
0 & 0 & 0 & 0 & 0 & 0 & \frac{1}{\rho} & 0 & 0 \\
0 & 0 & 0 & 0 & 0 & 0 & 0 & 0 & 0 \\
0 & 0 & 0 & 0 & 0 & 0 & 0 & 0 & 0 \\
0 & 0 & 0 & 0 & 0 & 0 & 0 & \frac{1}{2\rho} & 0 \\
0 & 0 & 0 & 0 & 0 & 0 & 0 & 0 & 0 \\
0 & 0 & 0 & 0 & 0 & 0 & 0 & 0 & \frac{1}{2\rho} \\
\sigma^p_{\epsilon^{11}} & \sigma^p_{\epsilon^{22}} & \sigma^p_{\epsilon^{33}} & 0 & 0 & 0 & 0 & 0 & 0 \\
0 & 0 & 0 & \sigma^s_{\epsilon^{12}} & 0 & 0 & 0 & 0 & 0 \\
0 & 0 & 0 & 0 & 0 & \sigma^s_{\epsilon^{13}} & 0 & 0 & 0
\end{pmatrix} \tag{6.28}$$

The Jacobians in the y- and z- directions are similar with the entries perturbed appropriately.

The eigenvalues for system (6.28) are

$$\lambda^{1,2} = \left(\pm\sqrt{\frac{\sigma^p_{\epsilon^{11}}}{\rho_0}} \right); \quad \lambda^{3,4} = \pm\sqrt{\frac{\sigma^s_{\epsilon^{12}}}{2\rho_0}}; \quad \lambda^{5,6} = \pm\sqrt{\frac{\sigma^s_{\epsilon^{13}}}{2\rho_0}}; \quad \lambda^{7,8,9} = 0. \tag{6.29}$$

The corresponding eigenvectors for system (6.28) are

$$\begin{pmatrix} 1 \\ 0 \\ 0 \\ \sqrt{\rho_0\sigma^p_{\epsilon_{11}}} \\ 0 \end{pmatrix}, \begin{pmatrix} 1 \\ 0 \\ 0 \\ -\sqrt{\rho_0\sigma^p_{\epsilon_{11}}} \\ 0 \end{pmatrix}, \begin{pmatrix} 0 \\ 0 \\ 1 \\ 0 \\ \pm\sqrt{2\rho_0\sigma^s_{\epsilon^{12}}} \end{pmatrix}, \begin{pmatrix} -\frac{\sigma^p_{\epsilon^{11}}}{\sigma^p_{\epsilon^{22}}} \\ 1 \\ 0 \\ 0 \\ 0 \end{pmatrix}. \tag{6.30}$$

6.4 Axisymmetric form of the Lagrangian Isentropic Equations

We use the axisymmetric form of these equations to verify that the shock wave generated by the Euler equations as our initial condition, propagates with the same strength and speed as in the Eulerian frame for the isentropic Euler equations.

The three-dimensional equations in cylindrical coordinates are

$$\begin{aligned}
(\epsilon_{rr})_t &= \frac{\partial u}{\partial r} \\
(\epsilon_{\theta\theta})_t &= \frac{u}{r} + \frac{1}{r}\frac{\partial v}{\partial \theta} \\
(\epsilon_{zz})_t &= \frac{\partial w}{\partial z} \\
(\epsilon_{rz})_t &= \frac{1}{2}\frac{\partial u}{\partial z} + \frac{\partial w}{\partial r} \\
(\epsilon_{r\theta})_t &= \frac{1}{2}\frac{\partial v}{\partial r} + \frac{1}{r}\frac{\partial u}{\partial \theta} - \frac{v}{r} \\
(\epsilon_{\theta z})_t &= \frac{1}{2r}\frac{\partial w}{\partial \theta} + \frac{\partial v}{\partial z} \\
\rho u_t &= \frac{1}{r}\frac{\partial \sigma_{r\theta}}{\partial \theta} + \frac{\partial \sigma_{rr}}{\partial r} + \frac{\sigma_{rr} - \sigma_{\theta\theta}}{r} + \frac{\partial \sigma_{rz}}{\partial z} \\
\rho v_t &= \frac{1}{r}\frac{\partial \sigma_{\theta\theta}}{\partial \theta} + \frac{\partial \sigma_{r\theta}}{\partial r} + \frac{2\sigma_{r\theta}}{r} + \frac{\partial \sigma_{z\theta}}{\partial z} \\
\rho w_t &= \frac{1}{r}\frac{\partial \sigma_{z\theta}}{\partial \theta} + \frac{\partial \sigma_{zz}}{\partial z} + \frac{\partial \sigma_{rz}}{\partial r} + \frac{\sigma_{rz}}{r}.
\end{aligned} \tag{6.31}$$

If we assume that $v = \epsilon_{\theta z} = \epsilon_{r\theta} = 0$ and there is no variation in the θ direction, then the system

(6.31) simplifies to

$$\begin{aligned}
(\epsilon_{rr})_t &= \frac{\partial u}{\partial r} \\
(\epsilon_{\theta\theta})_t &= \frac{u}{r} \\
(\epsilon_{zz})_t &= \frac{\partial w}{\partial z} \\
(\epsilon_{rz})_t &= \frac{\partial u}{\partial z} + \frac{\partial w}{\partial r} \qquad (6.32) \\
\rho u_t &= \frac{\partial \sigma_{rr}}{\partial r} + \frac{\sigma_{rr} - \sigma_{\theta\theta}}{r} + \frac{\partial \sigma_{rz}}{\partial z} \\
\rho w_t &= \frac{\partial \sigma_{zz}}{\partial z} + \frac{\partial \sigma_{rz}}{\partial r} + \frac{\sigma_{rz}}{r}. \qquad (6.33)
\end{aligned}$$

It is interesting to note here that the strain in the $\theta\theta$ direction is non-zero and in this case is called the *hoop strain*. A uniform radial displacement is not a rigid body motion, as it would be in the two-dimensional plane strain case, but instead produces a circumferential strain. This is because the original circumference of the cylinder is $2\pi r$, but when there is a strain in the radial direction the circumference grows to $2\pi(r + u_r)$, inducing a strain $2\pi u_r / 2\pi r = u_r / r$.

The Jacobian for system (6.32) in the z-direction is

$$f'(q) = -\begin{pmatrix} 0 & 0 & 0 & \frac{1}{\rho} & 0 & 0 \\ 0 & 0 & 0 & 0 & 0 & 0 \\ 0 & 0 & 0 & 0 & \frac{1}{2\rho} & 0 \\ \sigma^{rr}_{\epsilon_{rr}} & \sigma^{rr}_{\epsilon_{zz}} & 0 & 0 & 0 & 0 \\ 0 & 0 & \sigma^{rz}_{\epsilon_{rz}} & 0 & 0 & 0 \\ 0 & 0 & 0 & 0 & 0 & 0 \end{pmatrix}, \qquad (6.34)$$

and has an eigen-structure that is equivalent to the 2D system, with the addition of a second zero-speed eigenvalue. The corresponding eigenvector is

$$r^6 = \begin{pmatrix} 0 \\ 0 \\ 1 \\ 0 \\ 0 \\ 0 \end{pmatrix}. \qquad (6.35)$$

We solve these equations with the same approach as the axisymmetric form of the Euler equations. In this case, the equations for the source terms are

$$\begin{aligned}
(\epsilon_{\theta\theta})_t &= \frac{u}{r} \\
\rho u_t &= \frac{\sigma_{rr} - \sigma_{\theta\theta}}{r} \qquad (6.36) \\
\rho w_t &= \frac{\sigma_{rz}}{r}.
\end{aligned}$$

6.5 Preliminary Calculations

6.5.1 Comparison with the Euler Equations

Given the result in Figure 4.3, we are confident that the two systems of equations should agree for the weak shocks present in ESWT. In order to verify this, we used an initial condition generated by a calculation with the Euler equations for both the Lagrangian and Eulerian codes and compared the pressure wave at F2. In Figure 6.2 we see that the two codes give good agreement, but the wave from the Lagrangian calculation has been slightly attenuated.

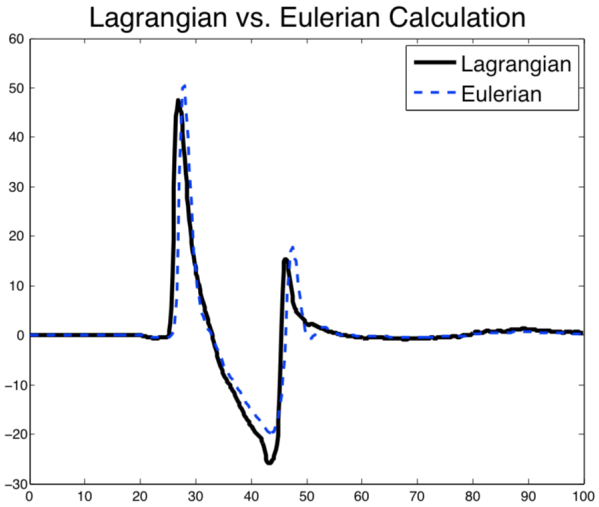

Figure 6.2: Comparison of the pressure pulse at F2 obtained in the Euler calculation (red dashed curve) and the Lagrangian calculation (blue curve). It is clear that the two sets of equations give good agreement. The wave in the Lagrangian case is slightly attenuated, but this may be due to error in initializing the calculation. In these calculations $\Delta x = 0.5mm$.

6.5.2 Initial Condition

As was discussed in Chapter 2, the initial condition for ESWT and ESWL has been the focus of some study. Prior work used the calculations performed by Hamilton [39, 3, 14] or plane wave initial data [72, 16] to simulate the ESWT wave at F2. These approaches are insufficient when investigating general 3D geometries because we are interested in both the focusing of the wave and the shear waves that may be generated in the solid.

We have modeled the initial wave at F1 as an isothermal expanding spherical wave. This generates larger negative pressures than what are typically measured at F1, since the typical pressure wave form measured 10mm from F1 is a decaying exponential with peak over pressure of 40 MPa [16, 14]. It is challenging to analytically calculate the correct theoretical wave form from an explosion in water generated by a spark plug. Theoretical results exist for strong shocks generated by explosions [69, 73, 79, 78], but this assumes an explosive source like TNT. In using an initial condition like a point-source explosion, a rarefaction region is generated as the wave expands, so the pressure wave

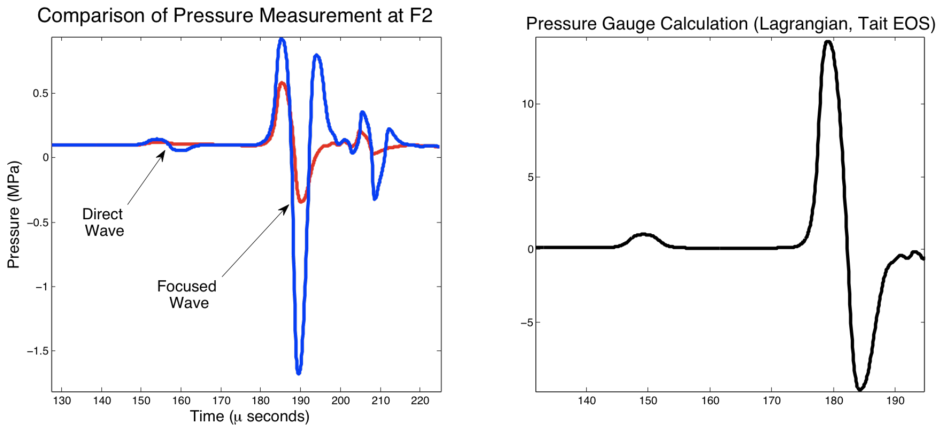

Figure 6.3: Comparison of pressure gauge measurements for different initial conditions in the Lagrangian form of the equations. In a) the blue curve is the spherically expanding pressure wave with both positive and negative pressure components, whereas the red curve has only positive pressure at F1 and there is a significantly smaller negative tail. In b) a set of initial conditions generated with the same all positive initial condition at different resolutions.

will have a negative tail. Something else is occurring with the shock that is generated by the spark plug source, but accurate modeling of this initial condition is beyond the scope of this work.

In order to generate an initial condition that more closely matches the measured initial pulse at F1, we simply do not allow the pressure to be negative in the region near F1. The results of this type of calculation can be seen in Figure 6.3. There is some precendent for this as T. Christopher [14] used this approach in order to truncate the overly negative tails he obtained in his model of the Dornier HM3 lithotripter. A rarefaction wave is generated when the direct wave hits the reflector, the largest tensile component is generated at the corner where the reflector is truncated, but reflection along the entire ellipsoidal bowl contributes to the tensile component of the pressure wave in our calculations. Results from the 2D axisymmetric calculation are used as initial data for the three-dimensional calculations. To do this we simply rotate the initial data about the z-axis, which is actually the x-axis in the three-dimensional calculations.

As mentioned in Chapter 2, different energy levels are used in the various ESWT treatments, as these lead to different peak over pressures at F2. The different energy levels correspond to different initial point source volumes and pressures. A list of the initial explosive pulse radius (centered at F1) and subsequent peak over pressure at F2 can be found in Table 6.1. The initial data used for each of our results is available in the ChomboClaw repository [29]. In Figure 6.5.2, we show an example of a general high pressure initial condition, in this case the figures come from the initialization of a 2D Lagrangian calculation.

Table 6.1: Initial Condition for Lagrangian Equations, $\delta h = 0.5$mm

Initial Radius (mm)	Initial Strain ($\epsilon_{rr} = \epsilon_{zz}$)	Pressure (MPa) at F2
2.0	-0.05	1.0
2.0	-0.25	2.0
4.0	-0.15	15.0
4.0	-0.25	33.0

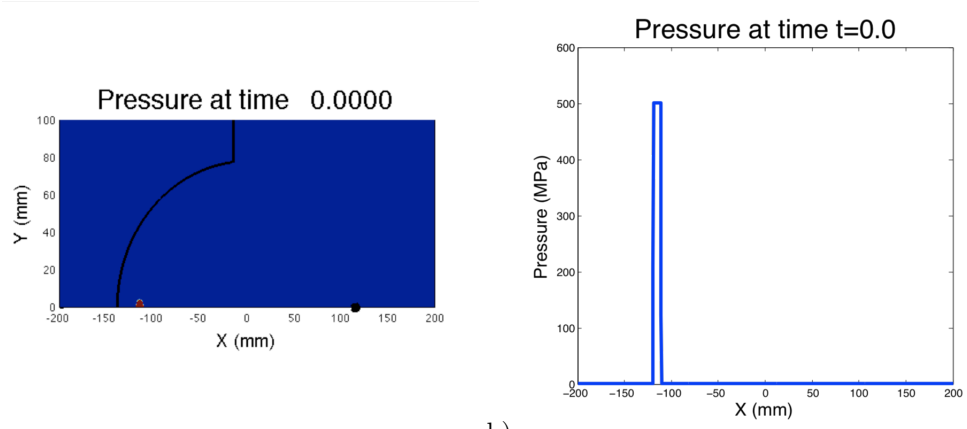

a) b)

Figure 6.4: Snapshot of a general initial condition for our calculations. In a) an isothermal spherical pressure pulse is initialized at F1 for an axisymmetric calculation. In b) a slice of the initial data is plotted to show more clearly how it is being defined. The velocities are initialized to zero.

Chapter 7

COMPUTATIONAL APPROACH

In this chapter I will describe in greater detail the numerical methods used to solve the hyperbolic systems of PDEs used in modeling ESWT. This chapter also contains an overview of the CLAWPACK software package where these methods are implemented, as well as a discussion of adaptive mesh refinement and computational issues encountered when solving the three-dimensional system.

7.1 High Resolution Finite Volume Methods

The acoustics equations, as well as the equations for linear elasticity and compressible flow are hyperbolic systems that can be written in the form

$$q_t - A(x,y,z)q_x + B(x,y,z)q_y + C(x,y,z)q_z = 0. \tag{7.1}$$

This system of equations is written in conservation form where A,B and C are the flux-functions in the x, y and z directions. This equation essentially states that within a given volume, the change in the state variables in time is due to fluxes at the boundary of the volume.

Recall that in our finite volume method, the computational domain is broken up into discrete grid cells, or volumes, and the state variables q are averaged within each grid cell to obtain piecewise constant data, with variation present only at cell interfaces. If we denote Q_i^n to the the average of grid cell i at time $n+1$, then

$$Q_i^{n+1} = Q_i^n - \frac{\Delta t}{\Delta x}(F_{i+1/2} - F_{i-1/2}) \tag{7.2}$$

where $F_{i-1/2}$ is the contribution of the flux at the $i-1/2$ interface and $F_{i+1/2}$ is the contribution of the flux at the $i+1/2$ interface. So in order to define our numerical method, we need to calculate the fluxes at the interfaces of our grid cells. We calculate the fluxes by solving Riemann problems at the cell interfaces and write the solution of these Riemann problems in terms of left-going and right-going waves.

In the case of 1D acoustics we obtained the following waves $\mathcal{W}$

$$\mathcal{W}^1_{i-1/2} = \alpha^1_{i-1/2}\begin{bmatrix} -\rho_{i-1}c_{i-1} \\ 1 \end{bmatrix} = \alpha^1_{i-1/2}r^1_{i-1}, \tag{7.3}$$

$$\mathcal{W}^2_{i-1/2} = \alpha^2_{i-1/2}\begin{bmatrix} \rho_i c_i \\ 1 \end{bmatrix} = \alpha^2_{i-1/2}r^2_{i}, \tag{7.4}$$

with strengths α determined by

$$\begin{bmatrix} p_i - p_{i-1} \\ u_i - u_{i-1} \end{bmatrix} = \begin{bmatrix} -\rho_{i-1}c_{i-1} & \rho_i c_i \\ 1 & 1 \end{bmatrix} = \begin{bmatrix} \alpha^1_{i-1/2} \\ \alpha^2_{i-1/2} \end{bmatrix}. \tag{7.5}$$

To obtain the new value of the state variables in grid cell i at time $t = n+1$, we must add in

the appropriate contribution to Q_i^{n+1},

$$Q_i^{n+1} = Q_i^n + \frac{\Delta t}{\Delta x}(\lambda_{i-1/2}^2 \mathcal{W}_{i-1/2}^2 + \lambda_{i+1/2}^1 \mathcal{W}_{i+1/2}^1). \tag{7.6}$$

In general, there will be more than one left-going and one right-going wave at each interface. For a system of m equations will consist of up to m waves each carrying part of the jump in q. If we assume there are m waves emanating to the left and right of a given interface, then we can define the left-going fluctuation as

$$\mathcal{A}^- \Delta q_{i-1/2} = \sum_{p=1}^{m} (\lambda^p)^- \mathcal{W}_{i-1/2}^p. \tag{7.7}$$

Similarly, the right-going fluctuation would be written as

$$\mathcal{A}^+ \Delta q_{i-1/2} = \sum_{p=1}^{m} (\lambda^p)^+ \mathcal{W}_{i-1/2}^p. \tag{7.8}$$

With this notation, it is clear that updating Q_i by adding in the appropriate waves gives the wave-propagation form of Godunov's method,

$$Q_i^{n+1} = Q_i^n - \frac{\Delta t}{\Delta x}[\mathcal{A}^+ \Delta Q_{i-1/2} + \mathcal{A}^- \Delta Q_{i+1/2}]. \tag{7.9}$$

Godunov's method is only first-order accurate. We use second-order correction terms to achieve higher order accuracy.

The introduction of second-order correction terms can be motivated by the Lax-Wendroff method applied to the case of constant-coefficient acoustics. The method can be written as a correction to the first-order upwind method in terms of the following correction fluxes

$$\tilde{F}_{i-1/2} = \frac{1}{2} \sum_{p=1}^{2} \left| \lambda_{i-1/2}^p \right| \left(1 - \frac{\Delta t}{\Delta x} \left| \lambda_{i-1/2}^p \right| \right) \mathcal{W}_{i-1/2}^p. \tag{7.10}$$

The second-order method takes the form..

$$q_i^{n+1} = q_i^n - \frac{\Delta t}{\Delta x}[\lambda_{i-1/2}^2 \mathcal{W}_{i-1/2}^2 + \lambda_{i+1/2}^1 \mathcal{W}_{i+1/2}^1] - \frac{\Delta t}{\Delta x}[\tilde{F}_{i+1/2} - \tilde{F}_{i-1/2}]. \tag{7.11}$$

This is the update used in the CLAWPACK software [27]. In the special case where $A_i = A$ is constant, equation (7.11) reduces to the standard Lax-Wendroff method. Flux limiting is used to appropriately cut off the second order correction terms in order to avoid spurious oscillations.

7.1.1 F-wave Formulation

The definition of the fluctuations $\mathcal{A}^{\pm} \Delta Q_{i+1/2}$ is based on a decomposition of the jump in q between the let and right state in the Riemann problem of the form (7.2). An alternative approach is to decompose the jump in f into waves $\mathcal{Z}^p$, called f-waves,

$$f(q_r) - f(q_l) = \sum_{p=1}^{m} \mathcal{Z}^p. \tag{7.12}$$

Assuming these waves $\mathcal{Z}^p$ are moving at speeds s^p, we define the fluctuations directly from $\mathcal{Z}^p$ as

$$\mathcal{A}^-\Delta Q_{i+1/2} \sum_{p:s^p_{i+1/2}<\ 0}^{m} \mathcal{Z}^p_{i+1/2} \quad \text{and} \quad \mathcal{A}^+\Delta Q_{i+1/2} \sum_{p:s^p_{i+1/2}>\ 0}^{m} \mathcal{Z}^p_{i+1/2}, \tag{7.13}$$

where the subscript $(i+1/2)$ refers to quantities resulting from the Riemann problem at the grid interface $x_{i+1/2}$. Moreover, in this framework, the high resolution correction fluxes are written as

$$\tilde{F}_{i+1/2} = \frac{1}{2} \sum_{p:s^p_{i+1/2}<\ 0}^{m} \operatorname{sgn}\left(s^p_{i+1/2}\right)\left(1 - \frac{\Delta t}{\Delta x}|s^p_{i+1/2}|\right)\tilde{\mathcal{Z}}^p_{i+1/2}. \tag{7.14}$$

If we have a set of m waves $\mathcal{W}^p$ and speeds s^p satisfying the conservation condition (3.22), then we can formulate the corresponding scheme in terms of f-waves by setting

$$\mathcal{Z}^p = s^p\mathcal{W}^p, \quad 1 \le p \le m. \tag{7.15}$$

On the other hand, that if we start with a decomposition of the jump in $f(q)$ as f-waves, then the waves $\mathcal{W}$ can only be recovered if the speeds are not zero.

An advantage of the f-wave approach is that by using (7.12) to define $\mathcal{Z}^p$ guarantees that the method will be conservative when the fluctuations (7.13) are used. This is true for any linearization $\bar{A}(q_l, q_r)$ of the Jacobian matrix $A(q) = f'(q)$ of the system, such as the simple arithmetic average $\bar{A}(q_l, q_r) = A(\frac{1}{2}(q_l + q_r))$. Whereas condition (3.22), may not be satisfied if the wave splitting is based on (7.2), unless $\bar{A}(q_l, q_r)$ is chosen to be a sepcial average such as the Roe average.The f-wave formulation is also advantageous in the context of spatially-varying flux funtions and problems, like those discussed in Chapter 6.

7.2 Multi-dimensional Numerical Method

Consider the numerical approximation of a two-dimensional hyperbolic system of conservation laws of the form

$$\frac{\partial q}{\partial t} + \frac{\partial f(q)}{\partial x} + \frac{\partial g(y)}{\partial y} = 0. \tag{7.16}$$

Let us assume a uniform Cartesian grid with space intervals $\Delta x, \Delta y$ in the x and y directions, respectively. Then set $x_i = i\Delta x,\ y_j = j\Delta y$ with $i, j \in \mathbb{Z}$. We will denote with $Q^n_{i,j}$ the approximate average of the solution $q(x, y, t)$ at time t^n over the cell $\mathcal{C}_{i,j} = (x_{i-1/2}, x_{i+1/2}) \times (y_{j-1/2}, y_{j+1/2})$, $x_{\pm 1/2} = (i \pm 1/2)\Delta x$, $y_{j\pm 1/2} = (j \pm 1/2)\Delta y$

$$Q^n_{i,j} \approx \frac{1}{\Delta x \Delta y}\int\int_{\mathcal{C}} q(x, y, t^n)dxdy. \tag{7.17}$$

7.2.1 Dimensional Splitting

The simplest way to extend one-dimensional numerical methods to higher space dimensions is to use dimensional splitting. A fractional-step method is applied to split the multidimensional problem into a sequence of one-dimensional problems. To solve the two dimensional system (7.16), we might alternate between solving the one-dimensional problem in the x-direction $\frac{\partial q}{\partial t} + \frac{\partial f(q)}{\partial x} = 0$ and the one-dimensional problem in the y-direction $\frac{\partial q}{\partial t} + \frac{\partial g(q)}{\partial y} = 0$. Given the initial values $Q^n_{i,j}$ at time t^n, we solve the first system along each row of cells $\mathcal{C}_{i,j}$ with j fixed in order to update $Q^*_{i,j}$. Then, using the values $Q^*_{i,j}$ as initial data, we solve the second system along each column of cells $\mathcal{C}_{i,j}$ with

i fixed, which gives $Q_{i,j}^{n+1}$ at time t^{n+1}.

7.2.2 Flux-Differencing Methods

Consider the integral form of the system (7.16) given by

$$\frac{d}{dt}\int\int_{\mathcal{C}_{i,j}} q(x,y,t)dxdy = \int_{y_{j-1/2}}^{y_{j+1/2}} f(q(x_{i+1/2},y,t))dy - \int_{y_{j-1/2}}^{y_{j+1/2}} f(q(x_{i-1/2},y,t))dy \tag{7.18}$$

$$+ \int_{x_{i-1/2}}^{x_{i+1/2}} g(q(x,y_{j+1/2},t))dx - \int_{x_{i-1/2}}^{x_{i+1/2}} g(q(x,y_{j-1/2},t))dx. \tag{7.19}$$

If we integrate this expression from t^n to t^{n+1}, we are led to a fully discrete flux-differencing method of the form

$$Q_{i,j}^{n+1} = Q_{i,j}^n - \frac{\Delta t}{\Delta x}\left[F(Q_{i,j}^n, Q_{i+1,j}^n) - F(Q_{i-1,j}^n, Q_{i,j}^n)\right] - \frac{\Delta t}{\Delta y}\left[G(Q_{i,j}^n, Q_{i,j+1}^n) - G(Q_{i,j-1}^n, Q_{i,j}^n)\right], \tag{7.20}$$

where the numerical fluxes $F(Q_{i,j}^n, Q_{i+1,j}^n)$ and $G(Q_{i,j}^n, Q_{i,j+1}^n)$ represent an approximation of the physical fluxes through the edges given by $x = x_{i+1/2}$, $y \in (y_{j-1/2}, y_{j+1/2})$ and $x \in (x_{i-1/2}, x_{i+1/2})$, $y = y_{j+1/2}$, respectively, over the time interval $[t^n, t^{n+1})$

$$F(Q_{i,j}^n, Q_{i+1,j}^n) \approx \frac{1}{\Delta t \Delta y}\int_{t^n}^{t^{n+1}} \int_{y_{j-1/2}}^{y_{j+1/2}} f(q(x_{i+1/2},y,t))dydt, \tag{7.21}$$

$$G(Q_{i,j}^n, Q_{i,j+1}^n) \approx \frac{1}{\Delta t \Delta x}\int_{t^n}^{t^{n+1}} \int_{x_{i-1/2}}^{x_{i+1/2}} f(q(x,y_{j+1/2},t))dxdt. \tag{7.22}$$

To define the numerical fluxes in (7.22), we can solve one-dimensional Riemann problems normal to each cell interface. If we use the approximate Riemann solvers described in Chapter 3, then we get

$$F(Q_{i,j}, Q_{i+1,j}) = f(Q_{i,j}) + \sum_{p=1}^{m}\left(s_{i+1/2,j}^{x,p}\right)^{-}\mathcal{W}_{i+1/2,j}^{x,p} \tag{7.23}$$

$$= f(Q_{i+1,j}) - \sum_{p=1}^{m}\left(s_{i+1/2,j}^{x,p}\right)^{-}\mathcal{W}_{i+1/2,j}^{x,p}, \tag{7.24}$$

where the set of m waves $\mathcal{W}_{i+1/2,j}^{x,p}$ and speeds $s_{i+1/2,j}^{x,p}$ is obtained by solving a Riemann problem in the x-direction for the system $\partial q/\partial t + \partial f(q)/\partial x = 0$ with data $Q_{i,j}, Q_{i+1,j}$ for the left and right states. If we solve the similar problem in the y-direction, we get the following numerical fluxes

$$G(Q_{i,j}, Q_{i,j+1}) = g(Q_{i,j}) + \sum_{p=1}^{m}\left(s_{i,j+1/2}^{y,p}\right)^{-}\mathcal{W}_{i,j=1/2}^{y,p} \tag{7.25}$$

$$= g(Q_{i,j+1}) - \sum_{p=1}^{m}\left(s_{i,j+1/2}^{y,p}\right)^{-}\mathcal{W}_{i,j+1/2}^{y,p}. \tag{7.26}$$

We can write the algorithm in terms of fluctuations by setting

$$\mathcal{A}^{\pm}\Delta Q_{i+1/2,j} = \sum_{p=1}^{m} \left(s^{x,p}_{i+1/2,j}\right)^{\pm} \mathcal{W}^{x,p}_{i+1/2,j} \text{ and } \mathcal{B}^{\pm}\Delta Q_{i,j+1/2} = \sum_{p=1}^{m} \left(s^{y,p}_{i,j+1/2}\right)^{\pm} \mathcal{W}^{y,p}_{i,j+1/2}. \quad (7.27)$$

We then obtain the following first-order upwind scheme

$$Q^{n+1}_{i,j} = Q^{n}_{i,j} - \frac{\Delta t}{\Delta x}\left(\mathcal{A}^{+}\Delta Q_{i-1/2,j} + \mathcal{B}^{-}\Delta Q_{i+1/2,j}\right) - \frac{\Delta t}{\Delta y}\left(\mathcal{B}^{+}\Delta Q_{i,j-1/2} + \mathcal{B}^{-}\Delta Q_{i,j+1/2}\right), \quad (7.28)$$

which is typically stable only for Courant number up to one half. To improve stability we include second-order correction terms and transverse fluctuations.

7.2.3 Multidimensional Wave Propagation Algorithms

The general form of the wave propagation algorithm for solving two-dimensional hyperbolic systems is

$$Q^{n+1}_{i,j} = Q^{n}_{i,j} - \frac{\Delta t}{\Delta x}\left(\mathcal{A}^{+}\Delta Q_{i-1/2,j} + \mathcal{A}^{-}\Delta Q_{i+1/2,j}\right) \quad (7.29)$$

$$- \frac{\Delta t}{\Delta y}\left(\mathcal{B}^{+}\Delta Q_{i,j-1/2} + \mathcal{B}^{-}\Delta Q_{i,j+1/2}\right) \quad (7.30)$$

$$- \frac{\Delta t}{\Delta x}\left(\tilde{F}_{i+1/2,j} - \tilde{F}_{i-1/2,j}\right) - \frac{\Delta t}{\Delta x}\left(\tilde{G}_{i,j-1/2} - \tilde{G}_{i,j+1/2}\right), \quad (7.31)$$

where the quantities $\mathcal{A}^{\pm}\Delta Q$ and $\mathcal{B}^{\pm}\Delta Q$ represent fluctuations arising from Riemann problems in the x and y directions, respectively. The $\tilde{F}$ and $\tilde{G}$ fluxes represent the second order corrections.

A method of the form , that is (7.31) with $\tilde{F} = \tilde{G} = 0$, is based on propagating waves normal to each interface. In reality, the waves will propagate in a multidimensional manner and affect cell averages in cells above and below those that are directly adjacent to the interface. In order to include these transverse effects, each fluctuation $\mathcal{A}^{*}\Delta Q_{i+1/2,j}$ (similarly $\mathcal{B}^{*}\Delta Q_{i+1/2,j}$) for $* = +$ and $-$ is split into two transverse fluctuations. The so-called down-going waves are $\mathcal{B}^{-}\mathcal{A}^{*}\Delta Q_{i+1/2,j}$ and similarly the up-going waves are $\mathcal{B}^{+}\mathcal{A}^{*}\Delta Q_{i+1/2,j}$. This transverse decomposition of the fluctuations can be viewed as solving a second Riemann problem in the transverse direction, even though it is not based on left and right states as we normally think of for a Riemann solver. Let us consider, for example, that the waves and speeds resulting from solving Riemann problems in the normal direction are based on the eigenstructure of some linearized matrices $\tilde{A}$ and $\tilde{B}$ of $f'(q)$ and $g'(q)$, respectively. Then we compute the coefficients β^p of the projection of $\mathcal{A}^{+}\Delta Q_{i+1/2,j}$ on the eigenvectors r^p_y of $\tilde{B}$, so that $\mathcal{A}^{+}\Delta Q_{i+1/2,j} = \sum_{p=1}^{m} \beta^p r^p_y$, and we get

$$\mathcal{B}^{\pm}\mathcal{A}^{+}\Delta Q_{i+1/2,j} = \sum_{p=1}^{m} (\lambda^p_y)^{\pm} \beta^p r^p_y, \quad (7.32)$$

where λ^p_y are the eigenvalues of $\tilde{B}$.

The transverse fluctuations are used to update the four neighboring $\tilde{G}$ fluxes (and similarly $\tilde{F}$

fluxes), according to

$$\begin{aligned}
\tilde{G}_{i+1,j+1/2} &= \tilde{G}_{i+1,j+1/2} - \frac{\Delta t}{2\Delta x}\mathcal{B}^{+}\mathcal{A}^{+}\Delta Q_{i+1/2,j}, \\
\tilde{G}_{i+1,j-1/2} &= \tilde{G}_{i+1,j-1/2} - \frac{\Delta t}{2\Delta x}\mathcal{B}^{-}\mathcal{A}^{+}\Delta Q_{i+1/2,j}, \\
\tilde{G}_{i,j+1/2} &= \tilde{G}_{i,j+1/2} - \frac{\Delta t}{2\Delta x}\mathcal{B}^{+}\mathcal{A}^{-}\Delta Q_{i+1/2,j}, \\
\tilde{G}_{i,j-1/2} &= \tilde{G}_{i,j-1/2} - \frac{\Delta t}{2\Delta x}\mathcal{B}^{-}\mathcal{A}^{-}\Delta Q_{i+1/2,j}.
\end{aligned} \tag{7.33}$$

The transverse correction terms also have the effect of improving the stability limit, allowing for a Courant number of 1, relative to the maximum wave speed in any direction.

Once the transverse corrections described above have been implemented, it is possible to obtain second-order accuracy by making one-dimensional flux corrections analogous to (7.11). Here we use the waves and speeds computed in solving the Riemann problem normal to each interface. The corrections have the form

$$\tilde{F}_{i+1/2,j} = \frac{1}{2}\sum_{p=1}^{m} |s^{x,p}_{i+1/2,j}| \left(1 - \frac{\Delta t}{\Delta x}|s^{x,p}_{i+1/2,j}|\right) \tilde{\mathcal{W}}^{x,p}_{i+1/2,j}, \tag{7.34}$$

where $\tilde{\mathcal{W}}^{x,p}_{i+1/2,j}$ is a limited version of $\mathcal{W}^{x,p}_{i+1/2,j}$ obtained by comparing $\mathcal{W}^{x,p}_{i+1/2,j}$ to $\mathcal{W}^{x,p}_{i-1/2,j}$ or $\mathcal{W}^{x,p}_{i+3/2,j}$ depending on the sign of s.

The second-order correction terms can also be propagated in in the transverse direction, thus improving the stability properties and reducing spurious oscillations in many problems [51]. This is accomplished by applying the routine that performs the transverse splitting to

$$\mathcal{A}^{\pm}\Delta Q_{i+1/2,j} \pm \sum_{p=1}^{m} |s^{x,p}_{i+1/2,j}| \left(1 - \frac{\Delta t}{\Delta x}|s^{x,p}_{i+1/2,j}|\right) \tilde{\mathcal{W}}^{x,p}_{i+1/2,j}, \tag{7.35}$$

instead of to $\mathcal{A}^{\pm}\Delta Q_{i+1/2,j}$.

In the interest of brevity, we only consider the extension of the above methods to two-dimensional problems. The three-dimensional implementation is analogous to what is done in 2D with the inclusion of additional doubly-transverse solvers. Discussion of the implementation of the full three-dimensional system can be found in [51].

7.3 Adaptive mesh refinement

Adaptive mesh refinement (AMR) is a process in a numerical computation where the domain of computational interest is discretized in such a way that the finest grid is used near features that require higher resolution. The grid may be statically defined at the beginning of a calculation or it can be defined dynamically during the course of the calculation. In using AMR, we save computational time by not using a fine grid over the entire computational domain and the method requires less storage. As we discuss later, the computational time savings are crucial for effectively modeling ESWT.

The algorithm used in CHOMBO and AMRCLAW are based on the local adaptive mesh refinement strategy that was first introduced by Berger and Oliger for computing time-dependent solutions to hyperbolic partial differential equations in multiple space dimensions [5]. In this approach, we start with the entire computational domain covered with a coarse mesh of Cartesian grid cells. Regions requiring additional resolution are identified or tagged by computing some local measure of

the original error. The tagged cells are then covered by a disjoint union of rectangles in the domain, which are then refined by some integer factor. Once the refinement step is completed, an integrator is used to update the solution on the composite grid. Then a correction procedure is used to fix up the solution at the coarse-fine grid interfaces. Eventually, the refinement at a grid cell may be greater than what is required for the calculation, and at this time the fine grid may be removed. An example of the use of AMR for refinement in a small region of the domain can be seen in Figure 7.1 where the finest grid is used only in refinement about the wave as it propagates.

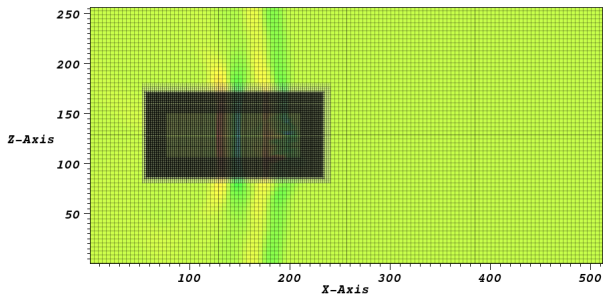

Figure 7.1: Adaptive mesh refinement allows the use of a fine grid in only a small part of the domain, in this case the region of interest is where the shock wave is propagating.

The main disadvantage to using block-structured AMR is its relative difficulty to implement when compared to algorithms defined on a single grid. AMRCLAW is a package developed by Berger and LeVeque [6] that provides the functionality of adaptive mesh refinement with the solvers for the wave propagation algorithm that are available in CLAWPACK [27]. This enables users to easily use AMR for problems they are solving with CLAWPACK. One of the disadvantages of this software is the lack of data structures available in Fortran 77 and lack of dynamic memory allocation that make it less useful for large, three-dimensional problems. Specifically, those problems that exceed 2GB in size.

An alternative software package that we have used for the three-dimensional problems in ESWT is Chombo, a set of C++ classes designed to support block-structured AMR applications. Chombo is based in part of the BoxLib toolkit [22]. In order to use this code base with the wave propagation algorithm implemented in CLAWPACK, Donna Calhoun wrote ChomboClaw[10]. Her work enabled us to use the same Riemann solvers and other fortran routines within the C++, ChFortran framework of Chombo. This enabled us to not only take advantage of AMR routines available in Chombo, but

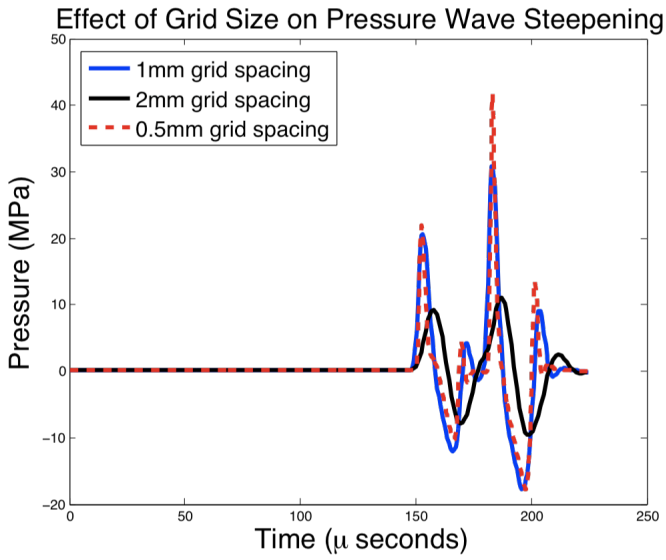

Figure 7.2: Effect of grid size on shock wave profile

also the routines for parallelization. Chombo contains many libraries, but those used in ChomboClaw [10] are the AMRTimeDependent and BoxTools libraries.

Something else we should note here is the use of HDF5 for I/O in Chombo. HDF5 is a portable, self-describing, binary format that has been developed for both serial and parallel applications [37]. Binary I/O is essential for problems generating large data sets that will typically be transferred to different machines for visualization and processing. The HDF5 output from Chombo can be visualized using VisIt, a freely available visualization package developed at LLNL [49].

7.3.1 AMR for ESWT

The focal region of most shock wave therapy devices is on the order of 10mm, however, the size of the lithotripter device and the propagation path of the shock wave is on the order of 100mm. The pressure jump is on the order of 0.1mm and requires a well-refined grid in order to maintain the correct strength and speed. These disparate spatial scales necessitate the use of adaptive mesh refinement. This enables us to use a coarse grid for the majority of the calculation, saving computational cost.

The pressure waveform found in ESWT contains a very thin region of high pressure that can not be resolved without a highly refined mesh. In Figure 7.3.1 we investigated the effect of grid refinement on the shock wave profile and found that with grid resolution greater than 0.25mm, the wave form at F2 was no longer a shock.

7.3.2 Performance

We have done some preliminary timing tests on an ESWT problem where a shock wave hits a cylinder directly. Figure 7.3 shows the number of minutes required for the job to complete as the number of processors are increased. It's clear from the graph that there is significant improvement from 30 to 64 processors. Near doubling of the processors led to job completion in 39% of the time

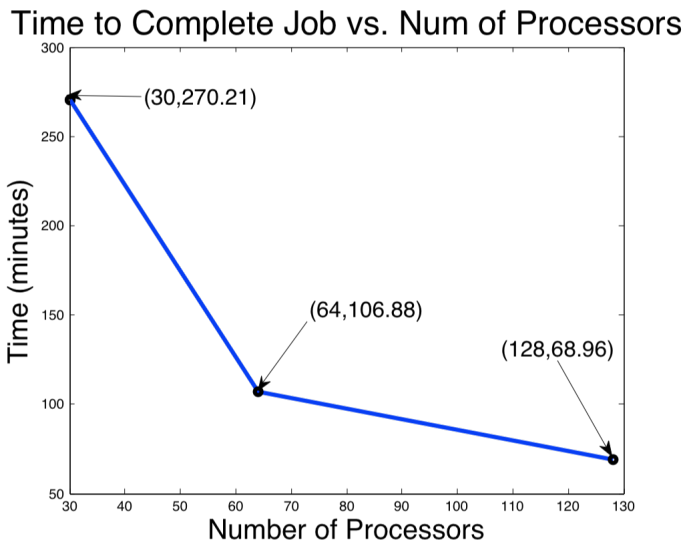

Figure 7.3: Timing data for a shock wave hitting a cylinder.

or ≈ 2.5 times as fast. This greater than 2 speed up is possibly due to the fact that the number of processors was more than doubled and the number of processors used in the smaller calculation was not a multiple of 4, which is the number of processors available per node. If we then compare the improvement from 30 to 128 processors, we see that the job was completed ≈ 3.9 times faster than with 30 processors. Lastly, if we consider the improvement from 64 to 128 processors, we see that the job was completed using 128 processors ≈ 1.5 times faster. The general trend seems to be that the time for job completion is halved as the number of processors is doubled. It should be noted here that we would have performed additional tests, but we could not request more processors on the Lonestar system.

7.3.3 Stability issues

There are also some numerical issues with the code. In some cases instability develops that seems to be related to the conservation fix at the coarse-fine grid boundaries in adaptive mesh refinement. It may be the case that some of the material properties are being set improperly leading to the instability. We should emphasize here that this is an extremely rare occurrence and is not related to the equations used for our model. This will be addressed in the next version of the code.

Chapter 8

PHOTOELASTICITY AND BIREFRINGENCE

Photoelasticity is an experimental technique for stress and strain analysis. The method is based on an optical property of some materials called birefringence. The birefringence in a stressed photoelastic object is dictated by the state of stress at each point in the specimen. This technique has been used by our collaborators at the Applied Physics Lab and others to investigate regions of maximal stress in ESWL and ESWT experiments [16, 83]. We use these experiments to validate our model. In this chapter we provide some background on the basic principles of photoelasticity, the governing equations and the numerical methods we use to solve these equations. In the results section we show how these methods are applied to our computational results of the strain field.

8.1 Background

The photoelastic effect can be adequately described by the electromagnetic theory of light [66, 1]. According to this theory, light is a transverse electromagnetic wave, where the electric and magnetic fields are perpendicular to each other and to the direction of propagation. The magnitude of the light (electric) vector, E, can be expressed in terms of a one-dimensional wave-equation

$$E = a\cos(2\pi/\lambda)ct = a\cos 2\pi ft = a\cos\omega t. \tag{8.1}$$

Where a is the amplitude, λ is the wavelength, c is the speed of light, t is the time, f is the frequency of the light, and $\omega = 2\pi f$ is the circular frequency of the light. For convenience, the amplitude and phase of a light wave are represented using the real part of

$$E = ae^{(i(2\pi/\lambda)ct} = ae^{iwt}. \tag{8.2}$$

Superposition of two or more waves having the same frequency but different amplitude and phase is easily performed using the exponential representation.

Most light sources consist of a large number of randomly oriented atomic or molecular emitters. The light rays emitted from such a source will have no preferred orientation and these rays make up an ordinary light beam. If a light beam is made up of rays with their electric fields restricted in a single plane, the light beam is said to be plane polarized or linearly polarized. The direction of the light vector is used to describe the polarization. Polarized light can be produced from an ordinary light source by reflection, scattering, fine grids and passing through a birefringent material.

In a vacuum, light propagates with a velocity, c, that is faster than its velocity in any other medium. The ratio of the velocity of light in free space to the velocity in a medium, n, is called the index of refraction. A wave propagating in a material will develop a linear optical path shift, δ, called retardation, with respect to a similar wave traveling in free space. The absolute retardation is given by

$$\delta = d(n-1), \tag{8.3}$$

where d is the thickness of the material along the path of light propagation. The retardation of one wave with respect to another is called the relative retardation.

8.1.1 Linear Polariscope

In photoelasticity, an optical instrument called a polariscope, is used to study the stress effect of models made of birefringent materials. In experimental work, two types of polariscopes are commonly used, the linear or plane polariscope and the circular polariscope. We will first focus on the linear polariscope.

Begin with light of wavelength λ, traveling in the z direction with velocity v, and polarized in the yz-plane. It's electric vector will be

$$\mathbf{E} = A\cos\left(\frac{2\pi}{\lambda}(z - vt)\right)\mathbf{j}. \tag{8.4}$$

Suppose this ray impinges normally on a birefringent plate of thickness d. Since birefringent materials resolve a light vector into two orthogonal components, the wave will be split into two components that propagate through the plate at different velocities, v_1 and v_2. Figure 8.1 shows the relationships between the different angles. The two scalar component waves are

$$\begin{aligned} E_1 &= E\cos\theta = a\cos\theta e^{i\omega t} \\ E_2 &= E\sin\theta = a\sin\theta e^{i\omega t}, \end{aligned} \tag{8.5}$$

where θ is the angle between the light vector E and the axis of polarization.

As the two components leave the birefringent plate, they have been retarded by different amounts. The retardation can be expressed as

$$\begin{aligned} \delta_1 &= d(n_1 - 1), \\ \delta_2 &= d(n_2 - 1), \end{aligned} \tag{8.6}$$

where n_1 and n_2 are the indices of refraction for waves vibrating parallel to the principal axes. The relative retardation is then computed as

$$\delta = \delta_2 - \delta_1 = d(n_2 - n_1). \tag{8.7}$$

The relative phase shift Δ between the two components as they emerge from the plate is given by

$$\Delta = \Delta_2 - \Delta_1 = (2\pi/\lambda)d(n_2 - n_1). \tag{8.8}$$

Since only the relative phase shift Δ affects the interference of the light components, it is common practice to set $\Delta_1 = 0$ and $\Delta_2 = \Delta$ [1]. Therefore the two components of the light vector are described by

$$\begin{aligned} E_1' &= a\cos\theta e^{i\omega t}, \\ E_2' &= a\sin\theta e^{i(\omega t - \Delta)}. \end{aligned} \tag{8.9}$$

Many noncrystalline transparent materials are optically isotropic under normal conditions, but become birefringent when stressed [66]. This effect persists while the loads are present, but disappears almost instantaneously when the loads are removed [66]. In a three-dimensional stress system, there are three principal stresses and three principal stress directions at any point. Relations between stresses and the indices of refraction at a point in a birefringent material were formulated by Maxwell

in 1852 as the stress-optic law [1, 66],

$$\begin{aligned} n_1 - n_0 &= C_1\sigma_1 + C_2(\sigma_2 + \sigma_3), \\ n_2 - n_0 &= C_1\sigma_2 + C_2(\sigma_1 + \sigma_3), \\ n_3 - n_0 &= C_1\sigma_3 + C_2(\sigma_1 + \sigma_2). \end{aligned} \tag{8.10}$$

Here n_0 is the index of refraction of the material in its unstressed state, n_1, n_2 and n_3 are the principal indices of refraction which coincide with the principal stress directions, σ_1, σ_2 and σ_3 are the principal stresses at the point and C_1 and C_2 are material constants known as *stress-optic coefficients*.

Incident light will propagate through a two-dimensional plane-stressed birefringent body and become polarized in the principal planes. The light will then emerge with a stress-induced relative retardation that can be determined by the stress-optic law to be

$$\delta = dC(\sigma_1 - \sigma_2), \tag{8.11}$$

or

$$\Delta = 2\pi dC(\sigma_1 - \sigma_2)/\lambda. \tag{8.12}$$

This is more commonly written as

$$\sigma_1 - \sigma_2 = Nf_\sigma/d, \tag{8.13}$$

where $N = \delta/\lambda = \Delta/2\pi$ is the fringe order and $f_\sigma = \lambda/C$ is the material fringe value. This is typically used in photoelastic stress analysis since the principal stress difference can be calculated if the material fringe value of the specimen can be measured at each point.

In three-dimensional photoelasticity, the stress-optic law is typically expressed in terms of the secondary principal stresses. The secondary principal stresses lie in the plane whose normal vector is coincident with the path of the light beam and not in the direction of the principal stress σ_1, σ_2 or σ_3. The equations above can be rewritten in terms of the secondary principal stresses σ_1' and σ_2' as

$$\begin{aligned} \Delta &= 2\pi dC(\sigma_1' - \sigma_2')/\lambda, \\ \sigma_1' - \sigma_2' &= Nf_\sigma/d. \end{aligned} \tag{8.14}$$

Since it is relatively simple to understand the form of the light emerging from a linear polarizer, we can use a polarizer to measures the relative retardation and the principal-stress directions that occur when polarized light passes through a stressed photoelastic model. When a light wave passes through the plane polarizer, the plane-polarized light wave emerging from the polarizer is

$$E = a\cos\theta e^{i\omega t}. \tag{8.15}$$

This plane-polarized light then enters the stressed model and is resolved into two components, E_1 and E_2, with vibrations parallel to the principal stress directions, σ_1 and σ_2, at the point it passes through. The two components of the wave will propagate through the material with different velocities and emerge with a relative phase shift between them described by (8.12). The phase difference cannot be observed directly because the eye, cameras, and other sensing devices are not sensitive to phase of the light. So a portion of the components E_1 and E_2 are brought together in a mixing device where they interfere with one another. The phase difference is thereby converted to an intensity difference, which can be detected and measured.

To accomplish this, a second polarizer (analyzer) is placed in the light path with its transmit-

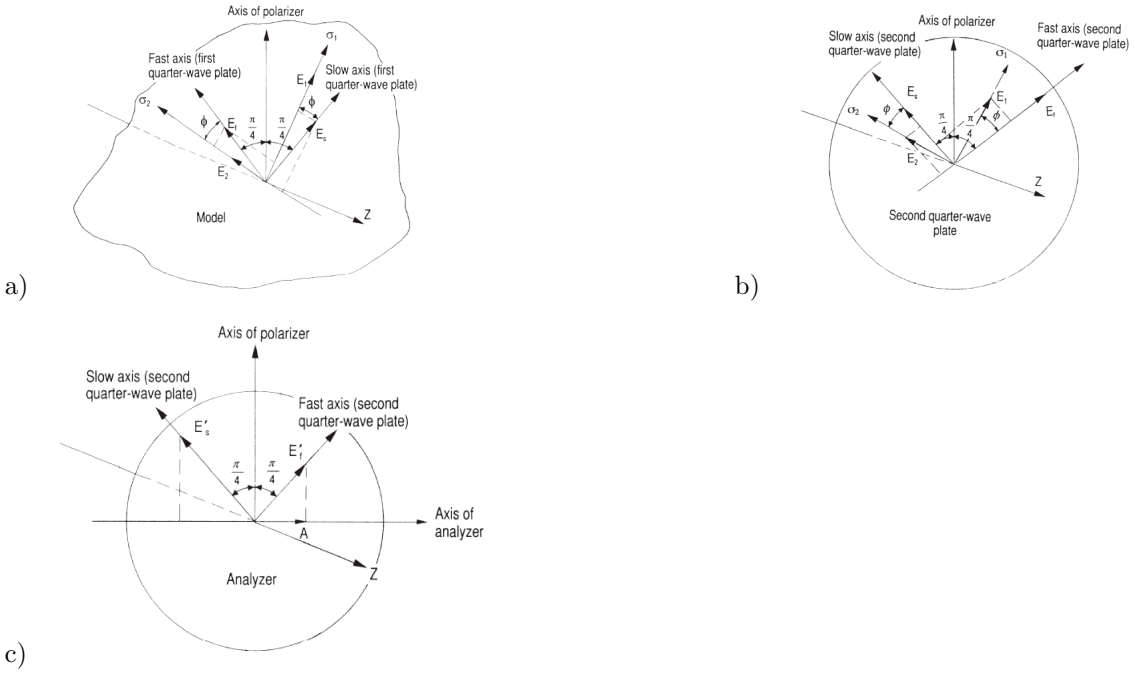

Figure 8.1: Different components of a circular polarizer, redrawn to mimic figures in [66]. See also [82].

ting axis at inclination θ from the original axis of polarization. This polarizer will transmit only components that are parallel to its axis. So the light emerging from the analyzer is given by

$$E_a = E_2' \cos(\theta) - E_1' \sin(\theta) = ia \sin(2\theta) \sin(\Delta/2) e^{i(\omega t - \Delta/2)}. \tag{8.16}$$

The intensity of light is equal to the product of the light vector and its conjugate, the intensity of the light emerging from the analyzer is

$$I = E_a E_a^* = a^2 \sin^2(2\theta) \sin^2(\Delta/2) = I_m \sin^2(2\theta) \sin^2(\Delta/2), \tag{8.17}$$

where I_m is the maximum intensity of the light emerging from the analyzer. In this case, the unstressed background will appear dark and this configuration is referred to as a dark field polariscope.

If the relative angle between the polarizer and analyzer is 90 degrees, the intensity is

$$I = I_m \left(1 - \sin^2(2\theta) \sin^2(\Delta/2)\right). \tag{8.18}$$

This result describes a simple harmonic wave of wavelength λ and with amplitude dependent on the relative retardation as well as inclination of the principal stress axes. The irradiance (amplitude squared) of the emergent light is zero if either

1. $\phi = m\pi$ (i.e., if the polarizers are aligned with the principal axes of refractive index or stress) or

2. $[(n_1 - n_2)]/(\lambda n_0)]d = 0, 1, 2, ...$ (i.e., if the relative retardation is an integer multiple of the

wavelength).

The equations show that two waves of radiation can combine to produce zero light. This interference phenomenon is something we can easily observe with our eyes or using a camera. Interference can occur only when waves of the same wavelength and the same polarization are able to interfere with one another.

8.1.2 Isoclinic and Isochromatic Fringes

Isoclinic fringes are a loci of points of constant inclination of the principal axes of refraction. When the birefringence of a material is produced by stress, the isoclinics indicate points at which the principal stress axes have the same inclination as the polarizer and analyzer. Isochromatic fringes are points where relative retardation is an integral multiple of the wavelength of the radiation. Using the equations above, we can relate the isochromatics to the magnitude of the stress. Recall that for the linear case we have

$$R = C_\sigma(\sigma_1 - \sigma_2)d = (\frac{n_1 - n_2}{n_0})d \tag{8.19}$$

where σ_1 and σ_2 are the principal stresses, d is the thickness of the material and n_i are the indices of refraction. Along an isochromatic, $R = m\lambda$, so along an isochromatic line

$$C_\sigma(\sigma_1 - \sigma_2) = \frac{m\lambda}{d}. \tag{8.20}$$

Thus, isochromatics are lines of constant principal stress difference or lines of constant maximum shear stress. To see this we write

$$\sigma_1 - \sigma_2 = 2\tau_{max} = \frac{m\lambda}{dC_\sigma}. \tag{8.21}$$

This is the information that is typically used when inferring the values of the stress from a fringe pattern obtained in an experiment, or the inverse of the problem we are interested in solving.

To see the difference in the two cases, consider the calculated results in Figure 8.2. The output from a linear analyzer, as shown in Figure 8.2 a) will contain both the isochromatic and isoclinic fringes, so it is more of a challenge to invert the image and obtain the stresses in the object. Whereas, the output from a circular analyzer, Figure 8.2 b), allows for a clearer analysis. The results from these calculations demonstrate that we are able to handle both cases with our numerical method.

8.2 Equations for General Photoelasticity

This section provides the details of how to derive the equations for photoelasticity that we use starting with Maxwell's equations. We also show the derivation of the stress-optic relations and provide details on when this analysis is valid. This distinction is important when considering the experiments in ESWT where simple application of the stress-optic law is invalid.

Following Aben [1], the derivation of general equations for the the polarization vector starts with Maxwell's equations

$$\nabla \times H = -\frac{1}{c}\frac{\partial D}{\partial t} \tag{8.22}$$

$$\nabla \times E = -\frac{1}{c}\frac{\partial H}{\partial t} \tag{8.23}$$

where H is the magnetic vector, E is the electric vector and D is the electric induction vector. In the case of a plane monochromatic wave with frequency ω the light field can be expressed in terms

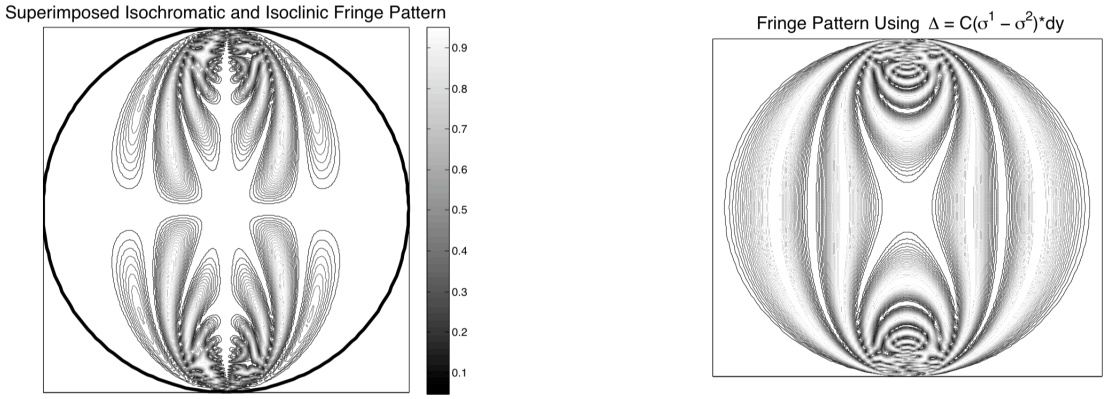

a) b)

Figure 8.2: Comparison of fringe output for different polarizer setups calculated using the analytic expressions for the stress field in a disc undergoing diametral compression. a) The output from a linear analyzer will contain both the isochromatic and isoclinic fringes, which leads to greater interference; b) The output from the circular analyzer contains only the isochromatics and is thus more useful for obtaining information about principal stresses.

of these vectors and complex exponentials (e.g. $E = E'e^{i\omega t}$). Assuming solutions of this form and inserting them into Maxwell's equations, we get

$$\nabla \times \nabla \times E' = \frac{\omega^2}{c^2} D'. \tag{8.24}$$

Then for an orthogonal coordinate system (omitting the primes), we get

$$\frac{d^2 E_1}{dz^2} + \frac{\omega^2}{c^2} D_1 = 0 \tag{8.25}$$

$$\frac{d^2 E_2}{dz^2} + \frac{\omega^2}{c^2} D_2 = 0 \tag{8.26}$$

where E_i and D_i are the components of the electric vector and electric induction vector along the x_ith coordinate vector in the system. Equations (8.5) describe the propagation of plane monochromatic electromagnetic waves in a nonhomogeneous dielectric medium in general [1].

The dielectric tensor relates the electric vector and electric induction in the following way

$$D_i = \sum_{j=1}^{2} \epsilon_{ij} E_j, i = 1, 2. \tag{8.27}$$

Using this in equations 1 and 2 above we get

$$-\frac{d^2 E_1}{dz^2} = \frac{\omega^2}{c^2}(\epsilon_{11} E_1 + \epsilon_{12} E_2) \tag{8.28}$$

$$-\frac{d^2 E_2}{dz^2} = \frac{\omega^2}{c^2}(\epsilon_{21} E_1 + \epsilon_{22} E_2). \tag{8.29}$$

It is sometimes advantageous to write the equations above in terms of the secondary principal directions. This is done by considering relations that rely on geometric relationships derived from the intersection of the $x_1 - x_2$ plane and the ellipsoid defined by the dielectric tensor ($x_i \epsilon_{ij} x_j = 1$). This intersection is an ellipse with principal axes that are used to define the *secondary principal values of the dielectric tensor in the $x_1 - x_2$ plane* and are denoted ϵ_1 and ϵ_2. The directions of these axes form an angle ϕ with the x_1 and x_2 axes. If rotation of the secondary axes occurs then the angle ϕ is a function of z and this is relevant when considering different properties of the medium that simplify the equations.

In the $x_1 - x_2$ plane, the following relationships hold:

$$\epsilon_{11} = \frac{\epsilon_1 + \epsilon_2}{2} + \frac{\epsilon_1 - \epsilon_2}{2} \cos(2\phi) \tag{8.30}$$

$$\epsilon_{22} = \frac{\epsilon_1 + \epsilon_2}{2} + \frac{\epsilon_1 - \epsilon_2}{2} \cos(2\phi) \tag{8.31}$$

$$\epsilon_{12} = \epsilon_{21} = \frac{\epsilon_1 - \epsilon_2}{2} \sin(2\phi), \tag{8.32}$$

and the components of the electric vector along secondary principal directions E_i^s are related to the components E_i through the following

$$E_1 = E_1^s \cos\phi - E_2^s \sin\phi \tag{8.33}$$

$$E_2 = E_1^s \sin\phi + E_2^s \cos\phi. \tag{8.34}$$

By introducing these relationships into the equations 3 and 4 we arrive at the following:

$$\begin{aligned} &\frac{d^2 E_1^s}{dz^2} + \left[\frac{\omega^2}{c^2} \epsilon_1 - \left(\frac{d\phi}{dz} \right)^2 \right] E_1^s - 2 \frac{d\phi}{dz} \frac{dE_2^s}{dz} - \frac{d^2\phi}{dz^2} E_2^s = 0 \\ &\frac{d^2 E_2^s}{dz^2} + \left[\frac{\omega^2}{c^2} \epsilon_2 - \left(\frac{d\phi}{dz} \right)^2 \right] E_2^s - 2 \frac{d\phi}{dz} \frac{dE_1^s}{dz} - \frac{d^2\phi}{dz^2} E_1^s = 0. \end{aligned} \tag{8.35}$$

These equations involve the secondary principal directions and are equivalent to (**??**).

In the case of photoelasticity, the low optical anisotropy and rotation of secondary principal directions makes the geometrical optics approximation invalid for a number of cases. The condition for determining the applicability of this approximation can be written as [1]

$$\frac{d\phi}{dz} \frac{\lambda}{2\pi\Delta n} \ll 1, \tag{8.36}$$

where λ is the wavelength and Δn is the birefringence. In a photoelastic medium Δn is typically on the order of 10^{-3} and $\frac{d\phi}{dz}$ may be unity, the condition (8.36) will probably not hold. Therefore, we would like to further simplify equations (8.35). This is done by considering the first order approximation to these equations, which gives a result that agrees well with experimental data [1].

Simplified Photoelastic Equations

Consider solutions to (8.5) of the form

$$E_j = A_j(z) e^{ikz} \quad j = 1, 2 k = \frac{\omega}{c} \epsilon \tag{8.37}$$

where ϵ is the dielectric constant of the medium in the absence of stress. This transformation does not alter the phase retardation or the amplitude ratio of the components of the light vector. Therefore,

the components A_j of the light vector determine the same light ellipse as the components E_j. If we substitute this into (8.5) , we get [1]

$$\begin{aligned}\frac{d^2A_1}{dz^2} - 2ik\frac{dA_1}{dz} + \frac{\omega^2}{c^2}(\epsilon_{11} - \epsilon)A_1 + \frac{\omega^2}{c^2}\epsilon_{12}A_2 = 0\\ \frac{d^2A_2}{dz^2} - 2ik\frac{dA_2}{dz} + \frac{\omega^2}{c^2}\epsilon_{21}A_1 + \frac{\omega^2}{c^2}(\epsilon_{22} - \epsilon)A_2 = 0.\end{aligned} \tag{8.38}$$

Since the optical anisotropy of a photoelastic medium is weak we have that [1]

$$\epsilon_{jj} - \epsilon \approx 10^{-3} \text{ to } 10^{-4} \tag{8.39}$$

$$\epsilon_{ij} \approx 10^{-3} \text{ to } 10^{-4} \quad i \neq j. \tag{8.40}$$

As a result, the functions A_j will vary slowly with z. Note that in the special case where the medium is isotropic, $A_j =$ constant. The coefficients on the first derivatives and constant terms in equations (8.38) are on the order of 10^5 and 10^6, so we can neglect the second derivatives $\frac{d^2A_j}{dz^2}$. Therefore the equations (8.38) simplify to

$$\begin{aligned}\frac{dA_1}{dz} &= -iC(\epsilon_{11} - \epsilon)A_1 - iC\epsilon_{12}A_2\\ \frac{dA_2}{dz} &= -iC(\epsilon_{22} - \epsilon)A_2 - iC\epsilon_{21}A_1\end{aligned} \tag{8.41}$$

where $C = \frac{\omega}{2c\sqrt{\epsilon}}$. In using this system we are neglecting solutions that describe reflected waves whose influence in a photoelastic medium can be neglected [1].

Similar to what was done in the previous section we can use an additional transformation

$$\begin{aligned}A_1 &= A_1^s\cos(\phi) - A_2^s\sin(\phi)\\ A_2 &= A_1^s\sin(\phi) + A_2^s\cos(\phi)\end{aligned} \tag{8.42}$$

(recall ϕ is the angle between the principal coordinate axes and the secondary principal coordinate axes) to obtain equations for the light vector along the secondary principal directions,

$$\begin{aligned}\frac{dA_1^s}{dz} &= -iC(\epsilon_1 - \epsilon)A_1^s + \frac{d\phi}{dz}A_2^s\\ \frac{dA_2^s}{dz} &= -iC(\epsilon_2 - \epsilon)A_2^s - \frac{d\phi}{dz}A_1^s.\end{aligned} \tag{8.43}$$

Further simplification of the equations is obtained through the following transformation

$$\begin{aligned}A_j &= B_j(z)\exp^{if(z)} \quad j = 1, 2\\ f(z) &= \frac{1}{2}C\int(\epsilon_{11} - \epsilon_{22} - 2\epsilon)dz.\end{aligned} \tag{8.44}$$

This transformation also preserves the phase retardation and amplitude ratio of the components of the light vector.

Using this transformation in Equations (8.43) yields

$$\begin{aligned}\frac{dB_1}{dz} &= -\frac{1}{2}iC(\epsilon_{11}-\epsilon_{22})B_1 - iC\epsilon_{12}B_2\\ \frac{dB_2}{dz} &= -\frac{1}{2}iC(\epsilon_{22}-\epsilon_{11})B_2 - iC\epsilon_{21}B_1.\end{aligned} \tag{8.45}$$

With an equivalent form for the components of the light vector in the secondary principal directions, B_j [1].

Explicit Stress Dependence

In photoelasticity, we are usually concerned with the stresses occurring within a material, such as the birefringent models observed in ESWT experiments. In order to derive optical equations in which the stresses appear directly, we need a relationship between the dielectric tensor ϵ_{ij} and the stress tensor σ_{ij}. For an isotropic medium undergoing elastic deformations we have the following [1]

$$\epsilon_{ij} = \epsilon\delta_{ij} + 2C_i\sigma_{ij} + 2C_2\sqrt{\epsilon}\sum_{k=1}^{3}\sigma_{kk}\delta_{ij} \tag{8.46}$$

where δ_{ij} is the Kronecker delta tensor and C_1 and C_2 are the photoelastic constants. This form of the equations was chosen so that the well-known equations of photoelasticity for the case of elastic deformations follow from equation (8.46).

If we plug equation (8.46) into the system (8.41) we get

$$\begin{aligned}\frac{dA_1}{dz} &= -iC\left(2C_1\sqrt{\epsilon}\sigma_{11} + 2C_2\sqrt{\epsilon}\sum_{k=1}^{3}\sigma_{kk}\right)A_1 - 2iCC_1\sqrt{\epsilon}\sigma_{12}A_2\\ \frac{dA_2}{dz} &= -2iCC_1\sqrt{\epsilon}\sigma_{21}A_1 - iC\left(2C_1\sqrt{\epsilon}\sigma_{11} + 2C_2\sqrt{\epsilon}\sum_{k=1}^{3}\sigma_{kk}\right)A_2.\end{aligned} \tag{8.47}$$

Now we use the transformation

$$\begin{aligned}A_j &= W_j(z)\exp^{-ig(z)} \quad j=1,2\\ g(z) &= 2CC_2\sqrt{\epsilon}\int\sum_{k=1}^{3}\sigma_k k dz\end{aligned} \tag{8.48}$$

to get

$$\begin{aligned}\frac{dW_1}{dz} &= -iC_0\sigma_{11}W_1 - iC_0\sigma_{12}W_2\\ \frac{dW_2}{dz} &= -iC_0\sigma_{21}W_1 - iC_0\sigma_{22}W_2\end{aligned} \tag{8.49}$$

where $C_0 = 2CC_1\sqrt{\epsilon}$.

If we introduce equation (8.46) into the system (**??**) we get

$$\frac{dB_1}{dz} = -\frac{1}{2}iC_0(\sigma_{11}-\sigma_{22})B_1 - iC_0\sigma_{12}B_2 \tag{8.50}$$

$$\frac{dB_2}{dz} = -iC_0\sigma_{21}B_1 + \frac{1}{2}C_0(\sigma_{11}-\sigma_{22})B_2, \tag{8.51}$$

or in terms of the secondary principal stresses

$$\frac{dB_1^s}{dz} = -\frac{1}{2}iC_0(\sigma_1 - \sigma_2)B_1^s + \frac{d\phi}{dz}B_2^s \tag{8.52}$$

$$\frac{dB_2^s}{dz} = -\frac{d\phi}{dz}B_1^s + \frac{1}{2}C_0(\sigma_1 - \sigma_2)B_2^s. \tag{8.53}$$

Equations (8.51) are the equations we solve numerically in order to determine the light intensity field that would result from the stresses obtained in our simulations of a shock wave hitting a cylinder, see Chapter 9. We should also note here that equations (8.51) are equivalent to the classical equations of photoelasticity derived by Neumann [1], but are more tractable for our purposes.

8.2.1 Special Case

One important special case to note here is that of a homogeneous solid, where in this case we mean that the stress tensor σ is constant and $d\phi/dz = 0$. This means that the above system (8.53) simplifies to

$$\frac{dB_1^s}{dz} = -\frac{1}{2}iC_0(\sigma^1 - \sigma^2) \tag{8.54}$$

$$\frac{dB_2^s}{dz} = -\frac{1}{2}iC_0(\sigma^2 - \sigma^1). \tag{8.55}$$

It then follows that, in the homogeneous photoelastic medium, two perpendicular independent plane-polarized vibrations with constant amplitudes are propagated [1]. The phase retardation of these vibrations Δ is

$$\Delta = C_0(\sigma^1 - \sigma^2)z, \tag{8.56}$$

where z is the thickness, or region over which the equations were integrated. This is equivalent to the stress-optic law, and demonstrates that this law is only valid when the principal stress directions do not change with z. An assumption that is not valid for three-dimensional objects [1].

8.3 Numerical Approach

We are interested in solving (8.51) for stresses generated by an ESWT pressure wave in an acrylic object. We use the model described in Chapter 6 to calculate the stresses in the object over time, and then post process these results to determine the appropriate light intensity distribution.

We assume that the monochromatic, polarized light is propagating along the $y-$axis $(0, 1, 0)$, so the system we solve is

$$\frac{dB_1}{dy} = -\frac{1}{2}iC_0(\sigma_{11} - \sigma_{33})B_1 - iC_0\sigma_{13}B_2 \tag{8.57}$$

$$\frac{dB_2}{dy} = -iC_0\sigma_{31}B_1 + \frac{1}{2}C_0(\sigma_{11} - \sigma_{33})B_2, \tag{8.58}$$

where we us appropriate stress components and integration is performed with respect to y. This system can be written as

$$\frac{dB}{dy} = M(y)B(y), \tag{8.59}$$

with initial data $B_0(y_0)$. In our numerical solution of this problem, the matrix M is constant in each grid cell.

8.3.1 Test Case

In order to verify that we are calculating the appropriate intensity field, we first compare our results with a well-known test case, a circle undergoing diametrical compression. The analytic solution for the strain field in this case is given by

$$\sigma^{rr} = \frac{p}{\pi R \Delta h} \frac{\left((1-\frac{r}{R}^2)^2(\frac{r}{R}^4 + 2\frac{r}{R}^2 - 1 - 2\cos(2\theta))\right)}{(\frac{r}{R}^4 + 1 - 2\cos(2\theta))^2} \tag{8.60}$$

$$\sigma^{\theta\theta} = \frac{p}{\pi R \Delta h} \frac{(\frac{r}{R}^8 + 4\frac{r}{R}^4 - 4\frac{r}{R}^2 - 1 + 2(-2\frac{r}{R}^6 + \frac{r}{R}^4 + 1)\cos(2\theta))}{(\frac{r}{R}^4 + 1 - 2\frac{r}{R}^2\cos(2\theta))^2} \tag{8.61}$$

$$\sigma^{\theta r} = \frac{p}{\pi R \Delta h} \frac{2(1-\frac{r}{R}^4)(1-\frac{r}{R}^2)\sin(2\theta)}{(\frac{r}{R}^4 + 1 - 2\frac{r}{R}^2\cos(2\theta))^2} \tag{8.62}$$

The solutions (8.60-8.62) for σ^{rr}, $\sigma^{\theta\theta}$ and $\sigma^{r\theta}$ are plotted in Figures 8.3 a), 8.3 b) and 8.3 c), respectively. The fringe patterns that researchers typically study are correlated through (8.10) to the difference in principal stresses $\sigma^1 - \sigma^2$, the eigenvalues of the stress tensor (see Chapter 4). This difference for the diametric compression problem are plotted in Figure 8.3.1 a). Ideally, these will correlate with the fringe patterns observed in the laboratory. By solving equation (8.10), and calculating the intensity I using equation (8.17), we can predict computationally what these fringe patterns will look like for this 2D problem in Figure 8.3.1 b).

For a simple, relatively thin two-dimensional model, this is an effective technique for determining either the fringe patterns from known stress values, or the difference in principal stresses from the fringe calculation. However, as was discussed in the previous section, relation (8.18) relies on no variation of the principal directions in the object and for a three-dimensional object, this is rarely the case [1]. In order to consider the fringe patterns resulting from light propagation in a three-dimensional object, we had to solve the system (8.58) numerically. We did this using two different numerical approaches, the trapezoidal method and the matrix exponential. It is important to note here that the eigenvalues for the matrix M are purely imaginary, so we must be careful to choose a numerical method with an appropriate stability region. For this reason, the first method we tried was the trapezoidal method. The results of this calculation are in Figure 8.3.1a). This method only captures the first order fringe, higher order fringes are damped out. In order to get better results, we wanted to use a higher-order method that would also capture the oscillatory nature of the fringe pattern.

Note that in each grid cell at a fixed moment in time, the stress tensor σ is constant. This means that the matrix M will also be constant, and we can solve equation (8.58) exactly through the use of a matrix exponential. For a $M \in \mathbb{C}^{2\times 2}$, with eigenvalues $\lambda^1 = \bar{\lambda}^2 = a + ib$, the matrix exponential has the following form

$$e^{At} = e^{at}\cos(bt)I + e^{at}\frac{\sin(bt)}{b}(A - aI), \tag{8.63}$$

where I is the identity matrix. When we use this approach we get the result in Figure 8.3.1b), which is more accurate than the trapezoidal method, and can be used in three-dimensional object because it does not rely on any simplifying assumptions.

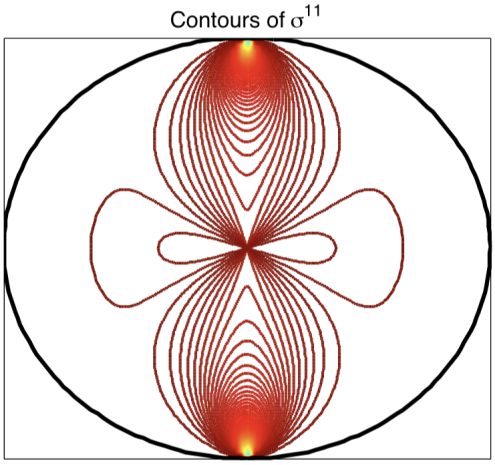

a)

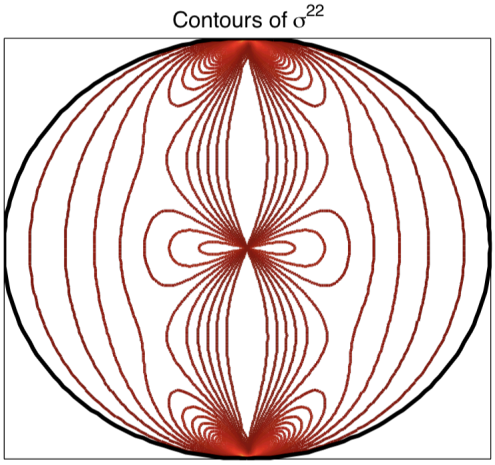

b)

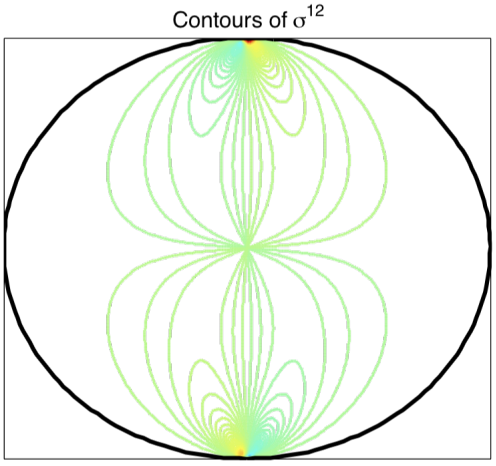

c)

Figure 8.3: Solution for the diametrically loaded circle a) σ^{11}, b) σ^{22}, c) σ^{12}

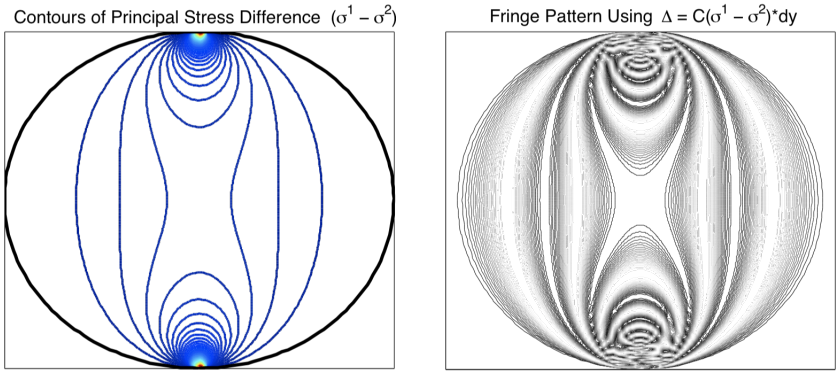

a) b)

Figure 8.4: Comparison of contours of maximum principal stress difference in a) with the Isochromatic fringe patterns calculated in b). The two agree reasonably well.

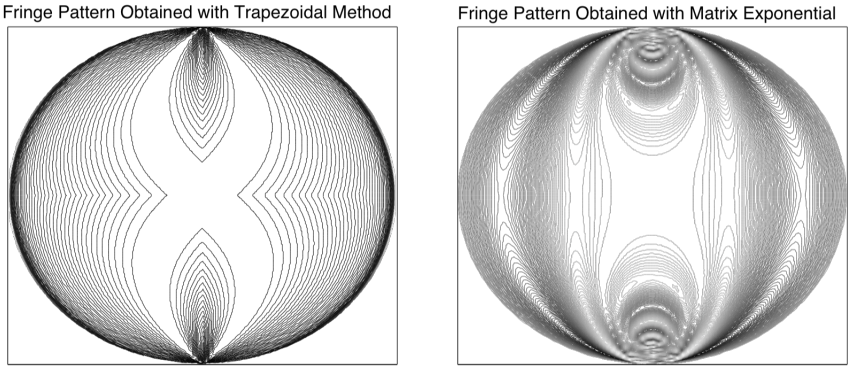

a) b)

Figure 8.5: a) Calculation of the fringes or principal stress contours with the trapezoidal method. Only one of the fringes is found, the rest are lost due to the inaccuracy of the method. b) Calculation of the fringes or principal stress contours with the matrix exponential, far more accurate and agrees reasonably well with Figure 8.3.1 a).

Chapter 9

VERIFICATION AND VALIDATION

In this chapter we will demonstrate the validity of our mathematical and computational model for shock wave therapy by comparing a series of numerical calculations to laboratory experiments.

9.1 Final model

9.1.1 Layout for numerical calculations

For the calculations done in comparison with the HM3 Dornier lithotripter, we used the numerical layout illustrated in Figure 9.1. Following T. Christopher [14], the ellipsoid for the HM3 has a major axis of $139mm$, a minor axis of $78mm$ and foci at $(\pm 115, 0, 0)$. The material in the reflector is made of brass, the fluid is water and we are not currently incorporating the interface between air and water. The material properties needed for the linear elasticity model are included in Table 9.1. The parameters used for water and tissue in the Tait equation of state are included in Chapter 4.

Table 9.1: Elastic material proprties

Material	Bulk modulus (MPa)	Shear modulus (MPa)	Density (kg/m^3)
brass	8650	6624.07	4528.24
acrylic	1850	9305	3126.5
water	2140	0	1000
bone(cortical)	12444	3510	1200

Table 9.2: Citations: bone [55]

Note the following relations between the material properties are given by the following relations and are provided here for reference [33],

$$\lambda = \frac{E\nu}{(1+\nu)(1-2\nu)} \tag{9.1}$$

$$G = \frac{E}{2(1+\nu)} \tag{9.2}$$

$$\nu = \frac{\lambda}{2(\lambda+G)} \tag{9.3}$$

$$E = 2G(1+\nu) \tag{9.4}$$

9.2 Pressure pulse measurements at F2

One of the key features of both ESWT and ESWL is the pressure wave form as measured at F2. In order to generate the correct wave form at F2 generated by an explosion in water at F1 by

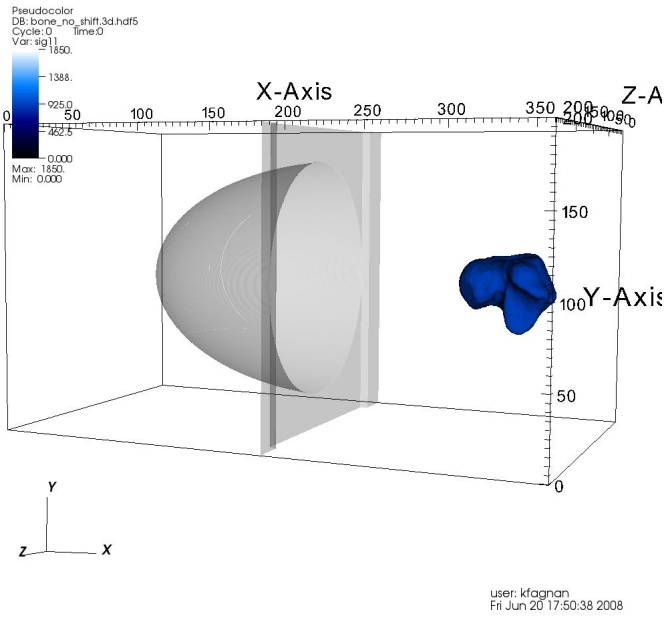

Figure 9.1: Numerical layout of the simulated HM3 Dornier Lithotripter with the talus bone at F2.

the HM3 Dornier lithotripter, we followed the same approach as T. Christopher [14]. That group used a triangular pulse initial condition for the change in density and velocity. The displacements generated in the fluid during the initial wave propagation and reflection are large, so we used the Euler equations to model the propagation and steepening of the wave. As demonstrated in Chapter 6, the pressure wave in ESWT can be modeled by an isentropic equation of state.

9.2.1 2-D Axisymmetric Gauge Calculations

In Figure 9.2 we see the shock wave measure at F2 when using the linear elastic code to model the wave propagation. The pulse is smeared out and does not accurately represent the shock wave form measured in ESWT. For this reason, we use the equations derived in Chapter 6 to model the wave propagation and steepening that we expect. The results from an axisymmetric version of this calculation are presented in Figure 9.3. In this result there is nice steepening of the focused wave with some variation in the positive peak pressure that depends on the initial condition used. For a more complete discussion of appropriate initial conditions for ESWT experiments, see Chapter 6.

9.2.2 Focal region

In addition to having the correct rise time for the peak pressure and tensile component of the wave form, it is important to calculate the focal region where pressures are strong enough to affect the tissue.

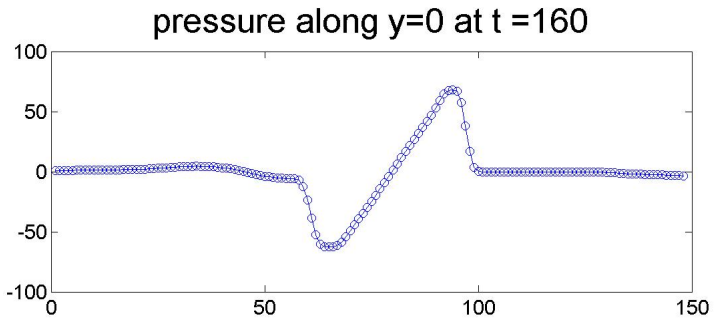

Figure 9.2: ESWT pulse measured at F2 obtained using the linear elasticity code.

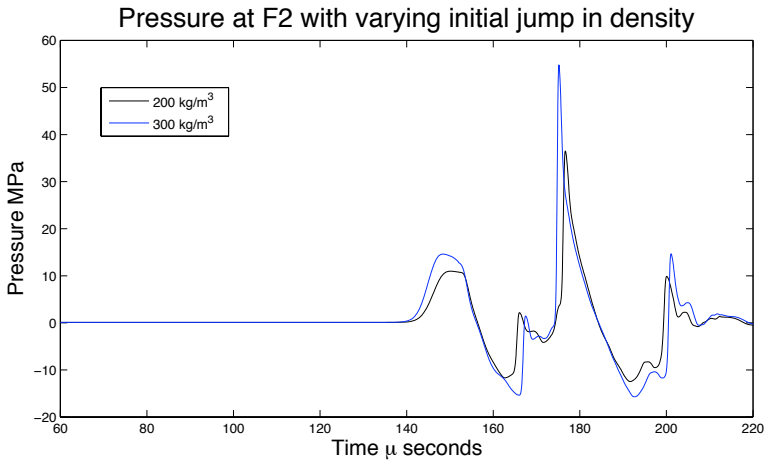

Figure 9.3: Axisymmetric calculation, Tait EOS for the ESWT pulse measured at F2.

Linear 2D HM3 Calculation

While not physically relevant, this calculation serves to demonstrate the effect of the geometry on the focal region of the calculation. In Figure 9.4 it is clear that the calculation produces a nice cigar shaped focal region when there is no inclusion present at the focus. In addition to this calculation, we include some additional two-dimensional calculations that demonstrate how the focal region changes when there is an object present at F2, see Figure 9.5. The change in the focal region due to objects present in the wave propagation path is to be expected. The impedence change from water to idealized bone causes part of the pressure wave to be reflected at each interface, see Chapter 2. From a clinical perspective, it is important to have an idea of where the maximal stresses are deposited in relation to F2, since it is clear that when treating bone, the focal region will not necessarily be centered about the focus.

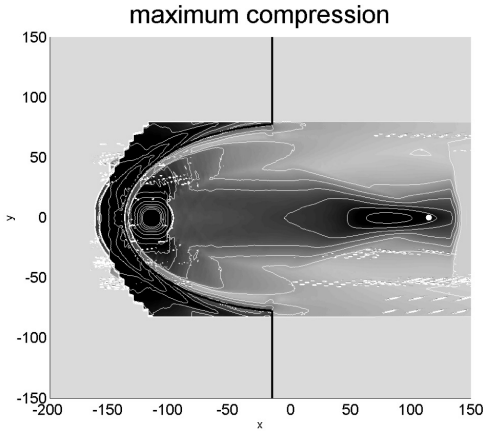

Figure 9.4: The maximal stress in a 2D calculation with no inclusion at the focus.

Nonlinear Calculation

The first results shows the calculation of the maximal stress region using the axisymmetric Lagrangian code. This calculation produces a nice cigar shaped region and the maximum pressure in this case is 15MPa.

Figure 9.6 shows the three-dimensional result with no inclusion present at F2. The calculation was performed using an initial condition from an axisymmetric calculation and started at $t = 120\mu s$, which is why the contour lines are not perfectly cigar shaped. What is clear from this calculation is that the wave does indeed continue to focus as it propagates and deposits the maximal energy, in this case 25.03 MPa at F2. I have included slices of the three-dimensional contour lines as they are easier to interpret than the isosurface calculations.

9.3 Cylindrical Calculations

9.3.1 Laboratory experiment

One of the experiments we used to validate the results of our calculations was performed by researchers at the Center for Industrial and Medical Ultrasound at the University of Washington. They photographed the shock wave from a device simulating the HM3 Dornier lithotripter as it

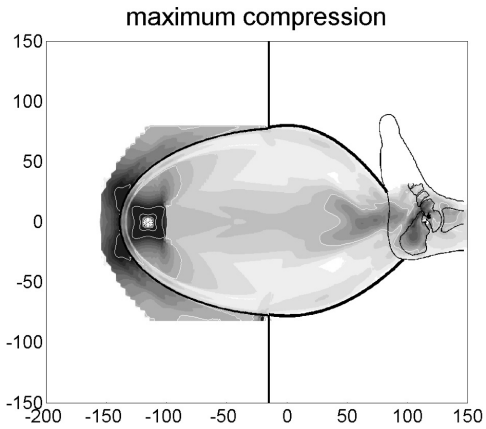

Figure 9.5: The maximum stress at each point over the entire calculation. The standard cigar shaped region is deformed because of the geometry of the bone inclusion. The range of the pressure was ([-15 15]).

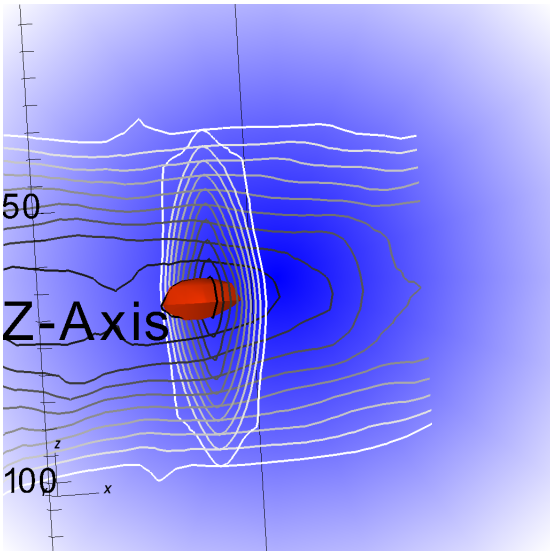

Figure 9.6: Results from three-dimensional calculation with focusing wave showing the cigar-shaped isosurface of maximum stress centered about F2 - (115,0,0)

propagated through an acrylic cylinder. Since acrylic is a birefringent material, the stresses have a photoelastic effect that can be captured through the use of a high-speed camera. The photographs from one of the experiments is in Figure 9.7. In this section, we compare these photographs to our numerical calculations.

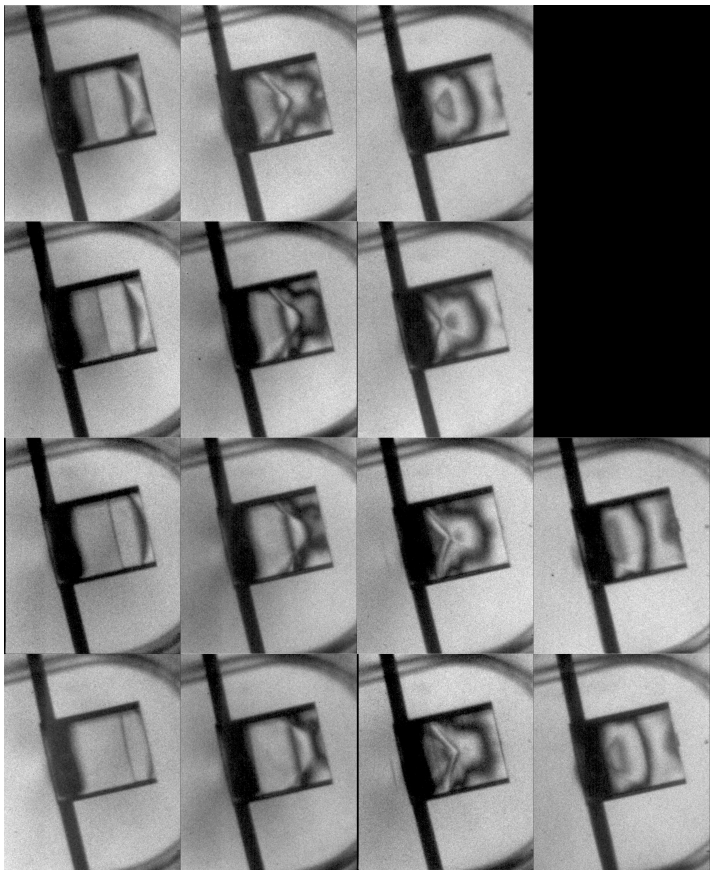

Figure 9.7: Laboratory experiment where a shock wave propagates through an acrylic cylinder and the stresses are photographed using a high speed camera and polarized filters[30]. Courtesy of Dr. Michael Bailey's group in the University of Washington Applied Physics Lab.

9.3.2 Results from linear elasticity

The first attempt at modeling the wave propagation in the cylinder was performed using linear elasticity in the fluid and solid [30]. The results in Figure 9.8 show the stress fields calculated using a plane wave initial condition. This shows that we achieve reasonably good agreement with the linear calculation even though we did not use a focusing wave or a nonlinear model in the fluid.

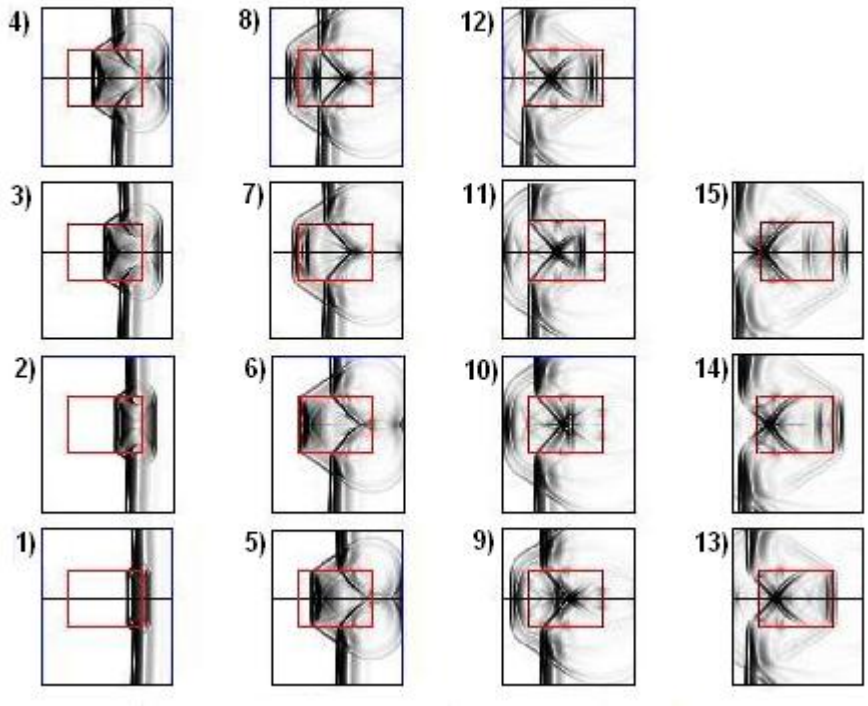

Figure 9.8: Axisymmetric calculation of a shock wave hitting a cylinder situated at F2 using linear elasticity.

9.3.3 Photoelastic comparison

In this experiment we compared the results from the nonlinear calculation with experiment after post-processing with the photoelastic equations. The experiment was initialized using the data from the axisymmetric Euler equations in order to incorporate both the focusing of the wave and the nonlinearity in the fluid. In Figure 6.2 from Chapter 6 it's clear that the Lagrangian code works well with the result from the Euler equations as an initial condition, so this is a reasonable approach.

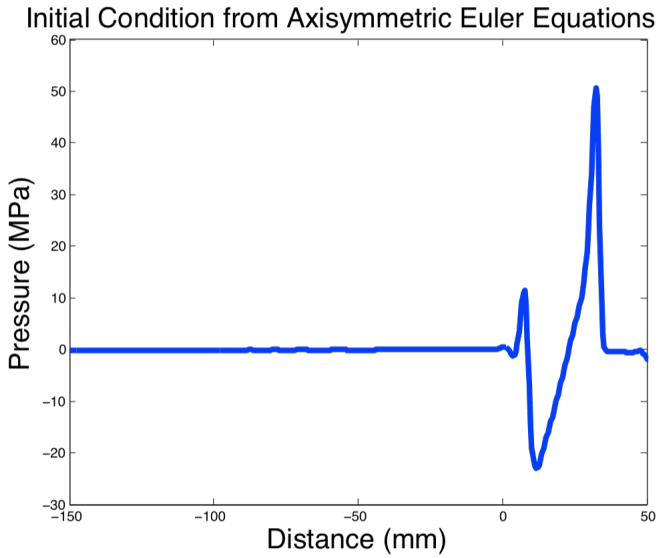

Figure 9.9: Pressure pulse used to initialize the nonlinear cylinder calculations (plotted in space, not time)

Results from nonlinear elasticity

A nonlinear axisymmetric calculation was performed to verify that the photoelastic code was working effectively. The two-dimensional stress fields were rotated about the z-axis in order to compare with the three-dimensional experiment. We compare the results from the calculations with the photographs of the cylinders in the laboratory experiments, shown in Figure 9.7. The results in Figure 9.10 and Figure 9.11 show photographs from the laboratory experiments in the first column and the results from the calculation in the second column. The images from the calculations are pseudocolor plots of the light intensity field, assuming a circular polariscope was used. The fringe patterns then indicate the isoclinic lines of maximum principal stress difference, which is the same as what is photographed in the lab. The calculation agrees well with the fringe patterns produced in the experiment, predicting the same v-shaped pattern of greatest stress, usually used to infer the location where the stone would break. It should be noted here that the results from the calculation provide similar insight to those obtained using linear elasticity. However, this approach may be more useful when considering cases with more complex photoelastic patterns such as those produced by Zhong, et. al. [83].

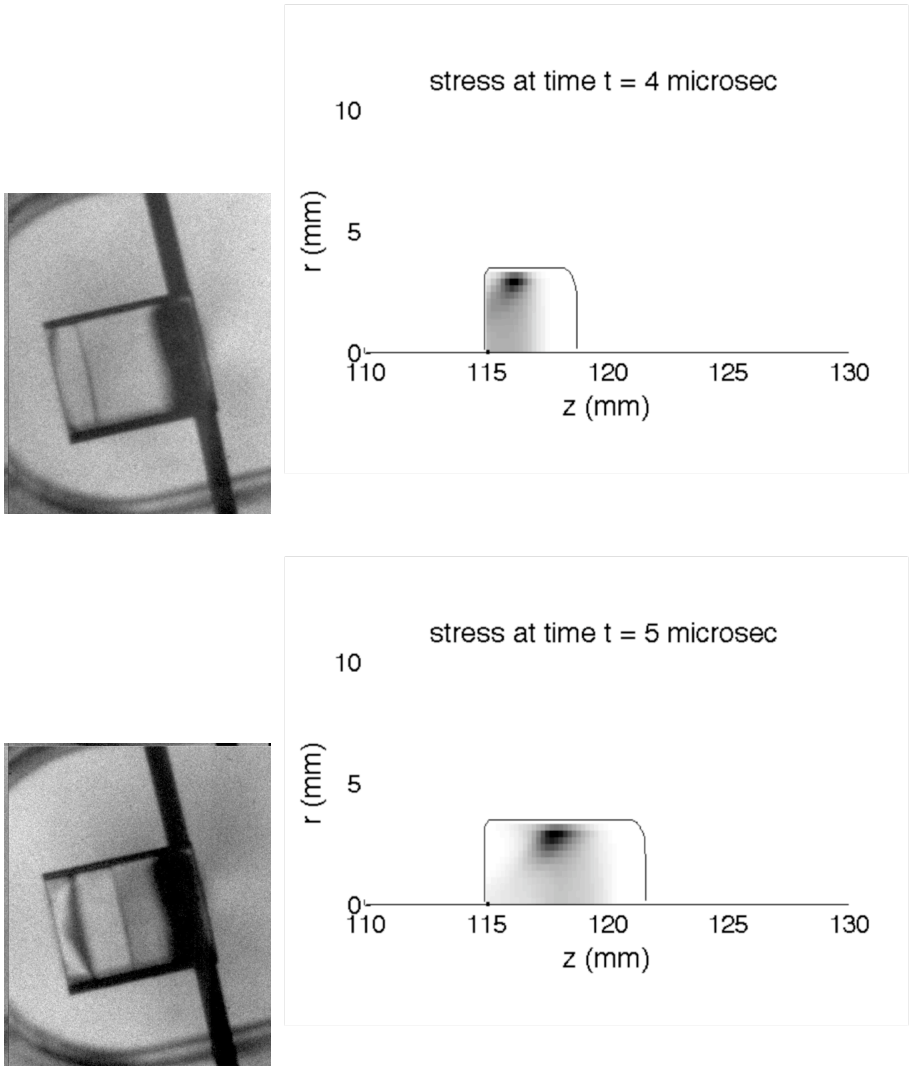

Figure 9.10: Nonlinear wave propagation in the fluid and linear elasticity in the solid acrylic cylinder. The pseudocolor plot captures the isoclinic regions of maximum principal stress difference. The calculation agrees well with the laboratory experiment.

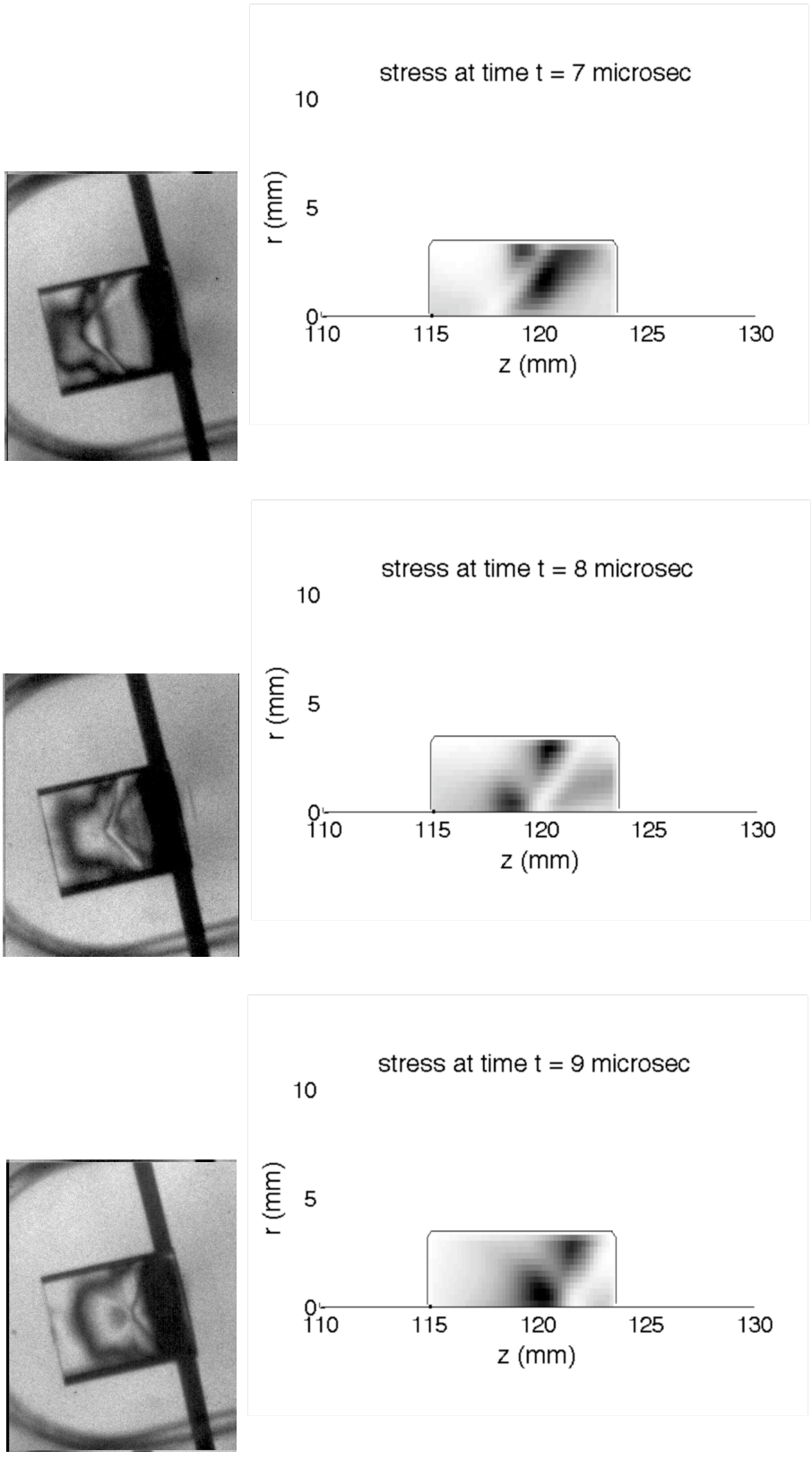

Figure 9.11: Nonlinear wave propagation in the fluid and linear elasticity in the solid acrylic cylinder. The pseudocolor plot captures the isoclinic regions of maximum principal stress difference. The calculation agrees well with the laboratory experiment.

9.3.4 Sphere

We performed calculations on the sphere from two different angles in order to confirm that the code was producing symmetric results with an object that was not aligned with the computational grid. It is also interesting to note that in calculations on smooth objects, there is no stress concentration that develops because there are no corners. These calculations could eventually be used in conjunction with the photoelastic code to compare against additional laboratory experiments.

In order to compare the rotated calculation with the direct calculation, we took two-dimensional slices along $y = 0$ in the direct case and at a 60 degree rotation about the y-axis, this is why the axes are not the same in the plots. In this case, the two regions of compression should be in the same location, as indicated by the results in Figure 9.12. There is some effect on the maximum stress when the initial condition is rotated, but these values are approximate because the material properties are not exact for the biological material. What we do know is the location of stress deposition for the given geometry is correct, which enables us to investigate the effect of other geometries and angle of treatment on the location of the focal region. The model could be further improved by the incorporation of a more accurate model for the bone material.

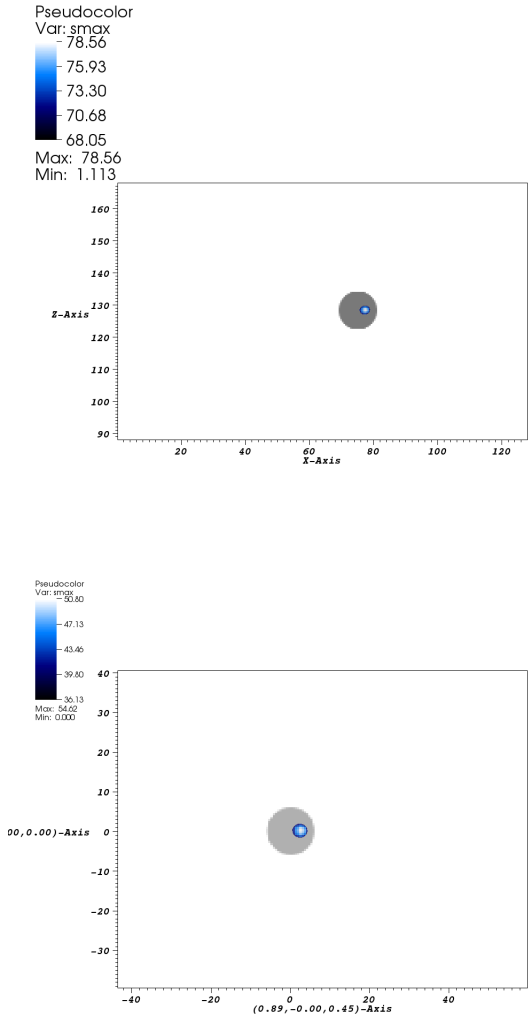

Figure 9.12: Comparison of maximum compression deposition for a sphere shot directly along the x-axis and rotation of 60 degrees about the y-axis.

9.4 Talus

We performed several fully three-dimensional calculations using the bone geometry of a talus. A group in the mechanical engineering department at The University of Washington has developed a rapid prototyping system for building bone models from CT scans [13]. They provided a digital copy of a talus that we used in our numerical calculations and also constructed a series of talus bones made out of different materials ranging from polyurethane to acrylic. Dr. Matula's group performed some experiments where they photographed the deflection of the cavitation field while varying the location of the talus at F2. We performed the corresponding calculations with our 3D code and kept track of the region of maximum negative pressure. This region should correspond to the cavitation field in the laboratory experiments. We compare the results in Figure 9.14 with the numerical results in Figure 9.15 and found reasonably good agreement between the cavitation field and the numerically calculated region of maximum tension. The talus calculations performed using the 3D linear elasticity code and with a pressure wave form that was more smeared out than the actual ESWT waveform [30].

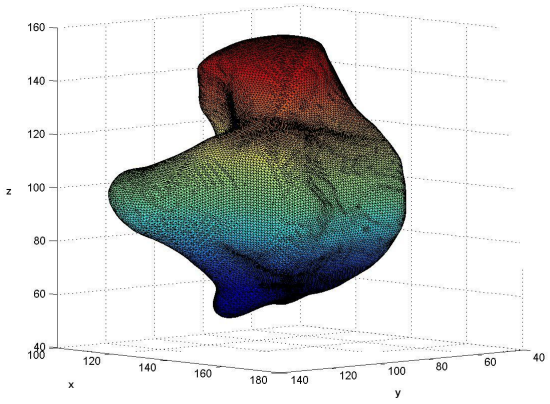

Figure 9.13: Digital representation of rapid prototype talus model.

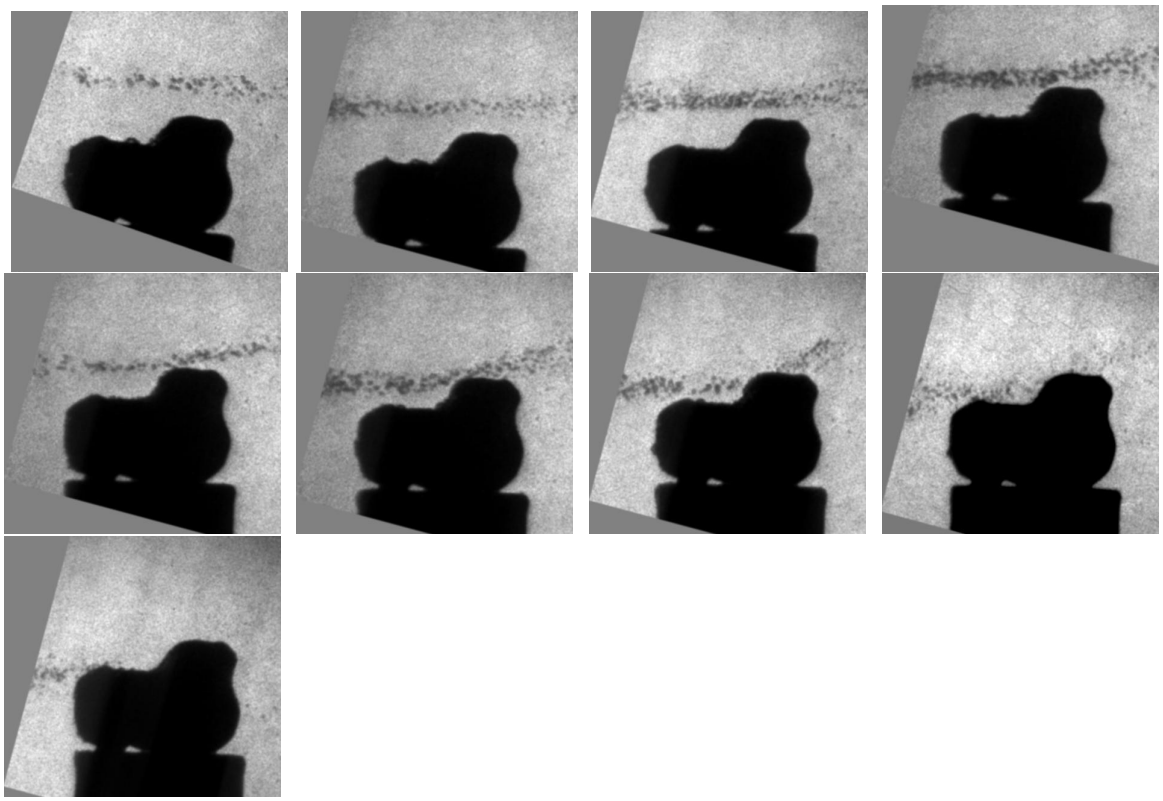

Figure 9.14: Photographs of experiments performed by Juan Tu, Applied Physics Lab, University of Washington.

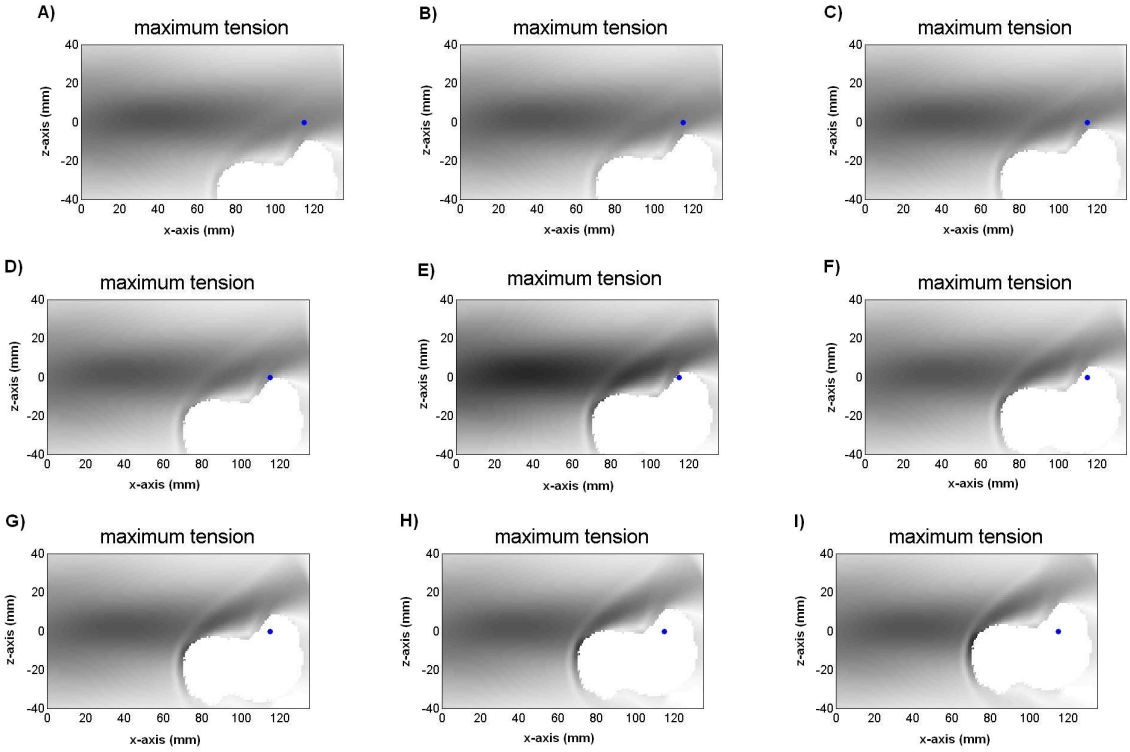

Figure 9.15: Calculation of the deflection of the ESWT pressure wave versus the location of the talus relative to F2.

Chapter 10

PREDICTIONS

In this chapter we provide details on the numerical experiments we performed in order to gain insight into the ESWT treatment. The first set of experiments were performed to investigate the pressure deposition in the treatment of nonunions. We used a cylinder comprised of averaged cortical bone material properties to represent the bone undergoing ESWT.

The calculations were performed on cylinders that are 20 mm in diameter, which is smaller than most bones in the body, but demonstrate the ability of our code to handle structures that are smaller than the talus or hip bone geometries. The angle of treatment has an effect on the deposition of the shear stress, as well as the location of the maximum and minimum principal stresses. To quantify this, we generated some one-dimensional curves showing the relationship between treatment angle, focal distance from F2 and principal stress values.

There are four heterotopic ossification experiments. The first involves shooting the HO from two different angles in order to mimic the treatments performed by Michael Chang. The stress contours and focal regions were quantitatively different in this case as well. In order to say something more about the treatment of HOs, I also devised an idealization of the HO experiment. In one case a sphere is embedded in a cylinder and centered at F2. In the second case, there is a gap between the sphere and the cylinder, obtained by subtracting the intersection of the sphere with a cylinder of a slightly larger radius. This is meant to show the importance of characterizing the nature of the material the HO is comprised of, as well as how attached it is to the skeleton. Currently it is known that the bone deposits form in the soft tissue and grow until intersecting with the skeletal system, but it is not clear how strong that attachment is [57]. If the attachment is weak, a gap exists between the HO and the skeleton, or there is an impedance difference in the two materials, then the behavior will be more like that of the sphere that is separate from the cylinder. In the fourth experiment, the material properties of the sphere or idealized HO are changed. We used this change to determine how much of an effect this has on the wave propagation.

The final set of experiments are axisymmetric calculations with variable parameters for the Tait equation of state. These experiments demonstrate the predictive capabilities of our mathematical and computational model of ESWT for materials that are more biological.

10.1 Nonunions

One of the aims of this work was to explore the effect of applying shock wave therapy at different angles when there is a fracture in the bone. To explore this, we have performed several three-dimensional experiments where we calculated the maximum stresses present in the cylinder during the pressure wave propagation. From the variation of the angle and position of F2 relative to the center of the cylinder, we are able to draw conclusions about the effect of positioning on the treatment of nonunions. Stress deposition location is dictated by the geometry of the interfaces between different materials. As discussed in Chapter 2, the reflections at these interfaces give rise to increases in the stresses as incoming waves interact with their reflected counterparts. This becomes clear when examining the experimental results which show that even as the object is shifted relative to F2, the location and shape of the compressive, tensile and shear stresses are determined by the geometry. The magnitude of the stresses will also be affected by the location of the object relative to F2

10.1.1 Initial Condition

These calculations were initialized with a shock wave that was computed from a high-resolution axisymmetric calculation with positive peak pressure of ≈50 MPa. In order to initialize a three-dimensional calculation, the initial data was rotated about the x-axis, which corresponded to the z-axis in the axisymmetric case. The rotation of the initial data was accomplished by rotating by 45 and 60 degrees about the y-axis with a center of $(115, 0, 0)$, the position of F2 for an HM3 Dornier lithotripter [14]. The following are snap shots of the three different initial conditions.

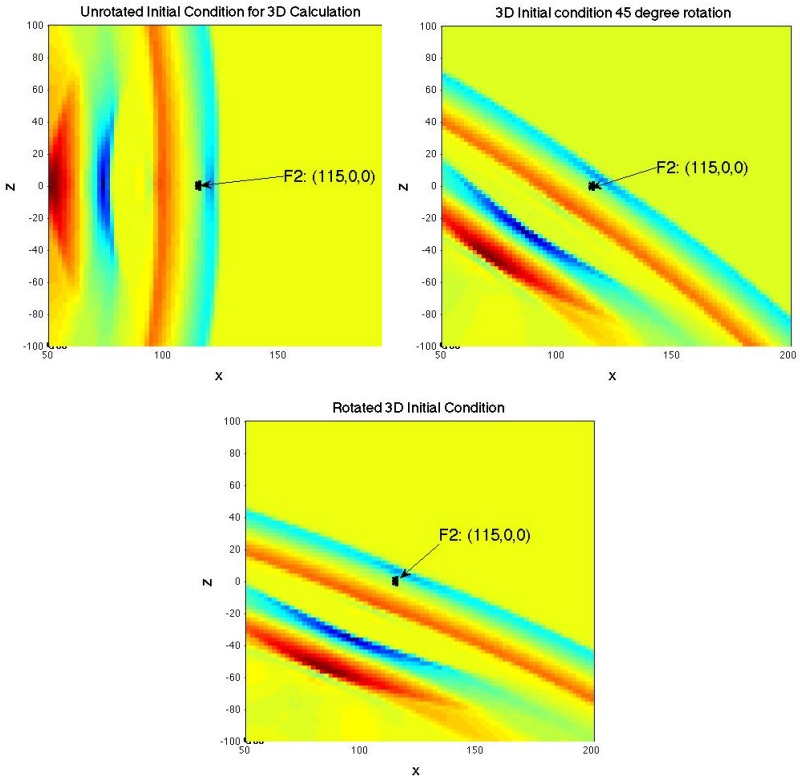

Figure 10.1: Initial conditions used for the three-dimensional calculations - direct, 45 degree rotation and 60 degree rotation about the y-axis. These are slices from $t = 162\mu s$, the time the calculations are started.

10.1.2 Cylinder

The first series of experiments were performed on a solid cylinder with the shock wave incident at three different angles. The cylinder represents a complete bone with corresponding material properties given in Table 9.1. This was used as a baseline for comparison against the cylinder with a break in it.

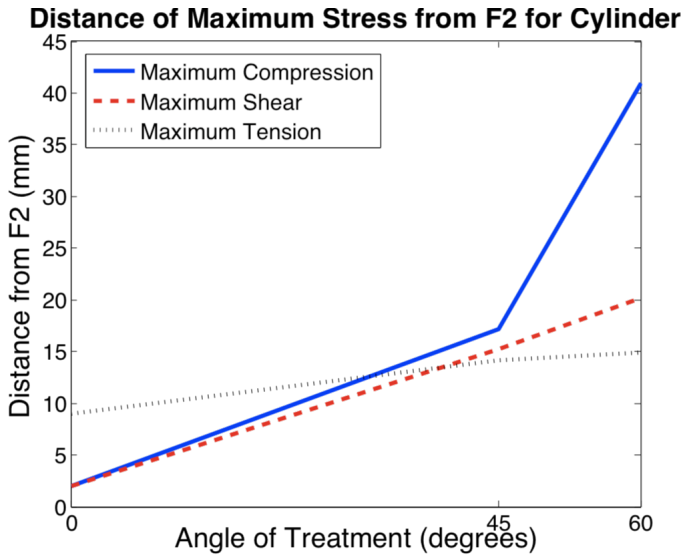

Figure 10.2: A comparison of the maximum stress deposition relative to the focus. The maximum shear and compression are the least affected when shot directly, but the location shift increases as the angle increases. The maximum tension is affected by the presence of an object at the focus, but less by the angle of treatment. Data from Tables (10.1,10.2,10.3)

The regions of maximum compression and shear are toward the back side of the cylinder, close to F2. Whereas the region of maximum tension is largely concentrated in the front of the cylinder where the first reflection occurs. This behavior is what we would expect from the discussion in Chapter 2 regarding Figure 2.4.

As the angle of treatment is varied, the region of maximum stress, or focal region, changes shape. The compression and shear regions are elongated, but still near the back of the cylinder. The maximum tension is shifted in location along the front of the cylinder, which makes sense since the incident wave is now interacting with a larger portion of the cylinder/water interface. It is also important to note that the actual location of the maximum stress region is shifted positively along the z-axis as the angle of the treatment is increased. This leads to the increase in distance of the maximum stress location from F2 observed in the compression and shear. However the increased distance for the tension is smaller as the angle is increased primarily because the presence of the object at F2 and the impedance difference between the two materials causes the maximum tension to be deposited at the surface of the object, not at F2.

Stress type	Maximum in absolute value (MPa)	Location (x,y,z)
Compression	64.83 MPa	(77,128,128)
Tension	-65.18 MPa	(66,128,128)
Shear	53.26 MPa	(77,128,128)

Table 10.1: Cylinder stresses for direct wave

Stress type	Maximum in absolute value (MPa)	Location (x,y,z)
Compression	59.36 MPa	(85,128,142)
Tension	-78.5 MPa	(65,128,118)
Shear	40.40 MPa	(83,128,141)

Table 10.2: Cylinder stresses for 45 degree rotation

Stress type	Maximum in absolute value (MPa)	Location (x,y,z)
Compression	53.77 MPa	(84,128,168)
Tension	-55.33 MPa	(65,128,117)
Shear	38.85 MPa	(84,129,146)

Table 10.3: Cylinder stresses for 60 degree rotation

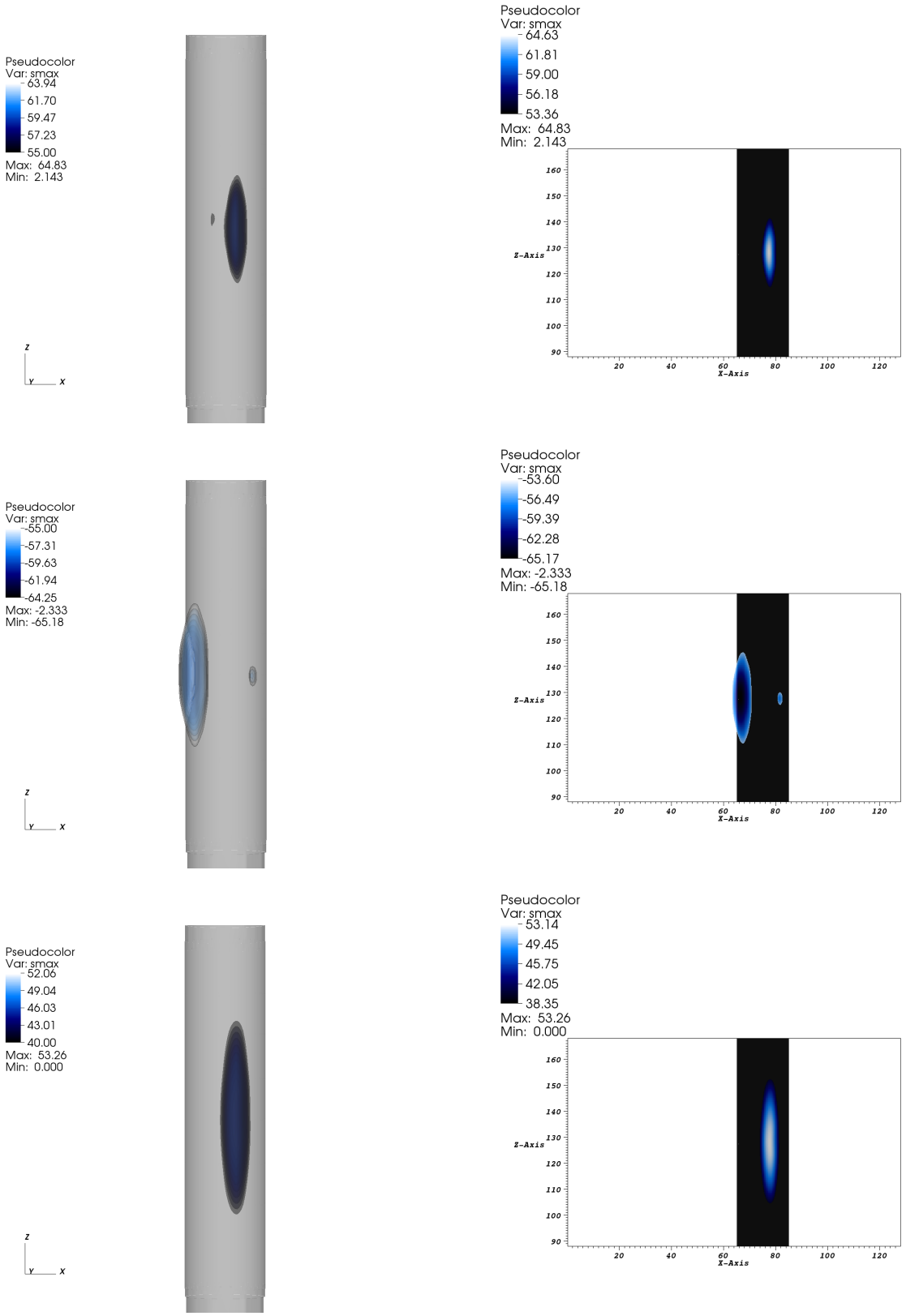

Figure 10.3: Three-dimensional results for the direct treatment of a complete cylinder. This figure shows the isosurfaces of maximum compression, tension and shear in the first column with corresponding 2D slices at y=0 in the second column.

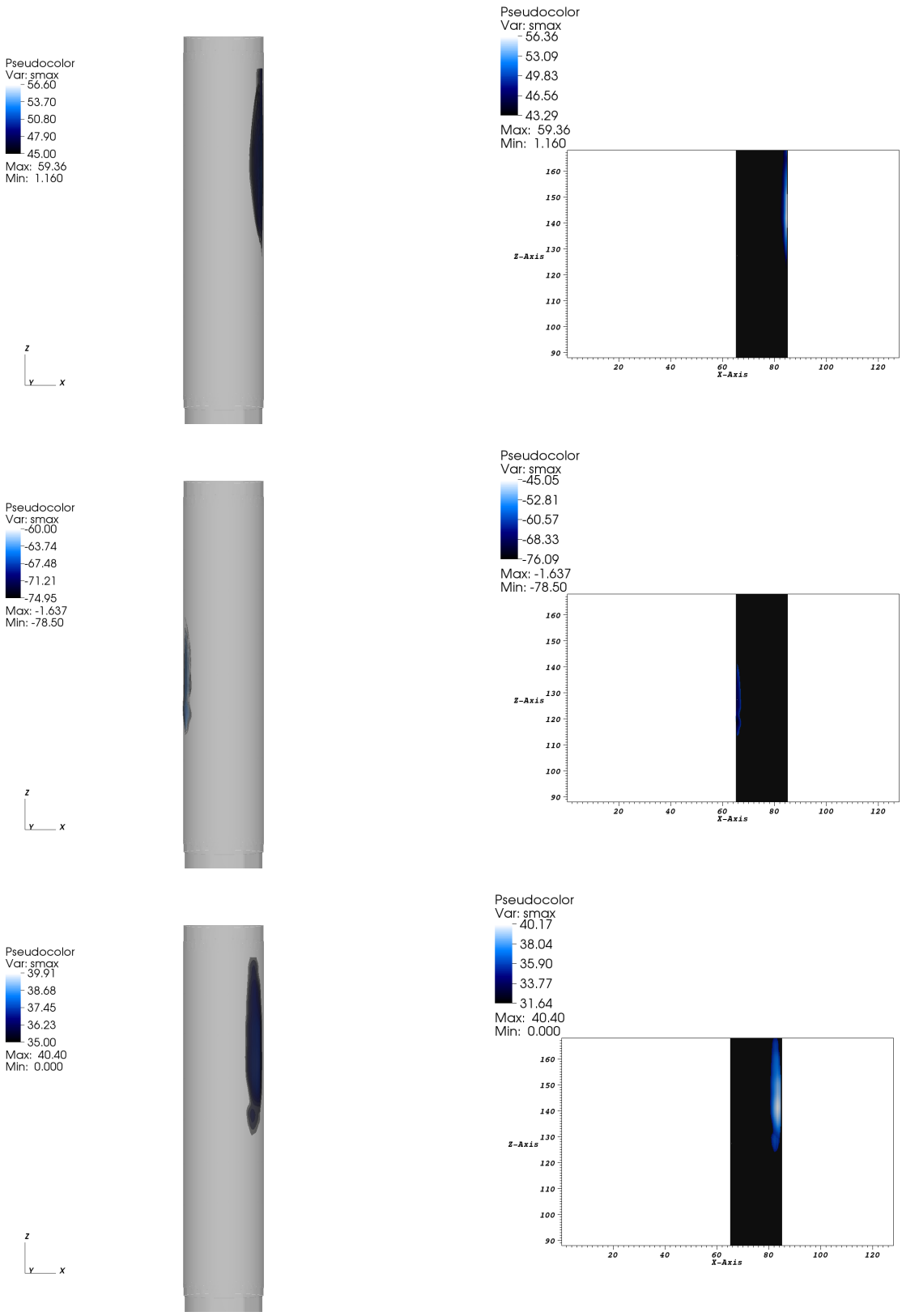

Figure 10.4: Three-dimensional results for 45 degree angles of treatment of a complete cylinder. This figure shows the isosurfaces of maximum compression, tension and shear in the first column with corresponding 2D slices at y=0 in the second column.

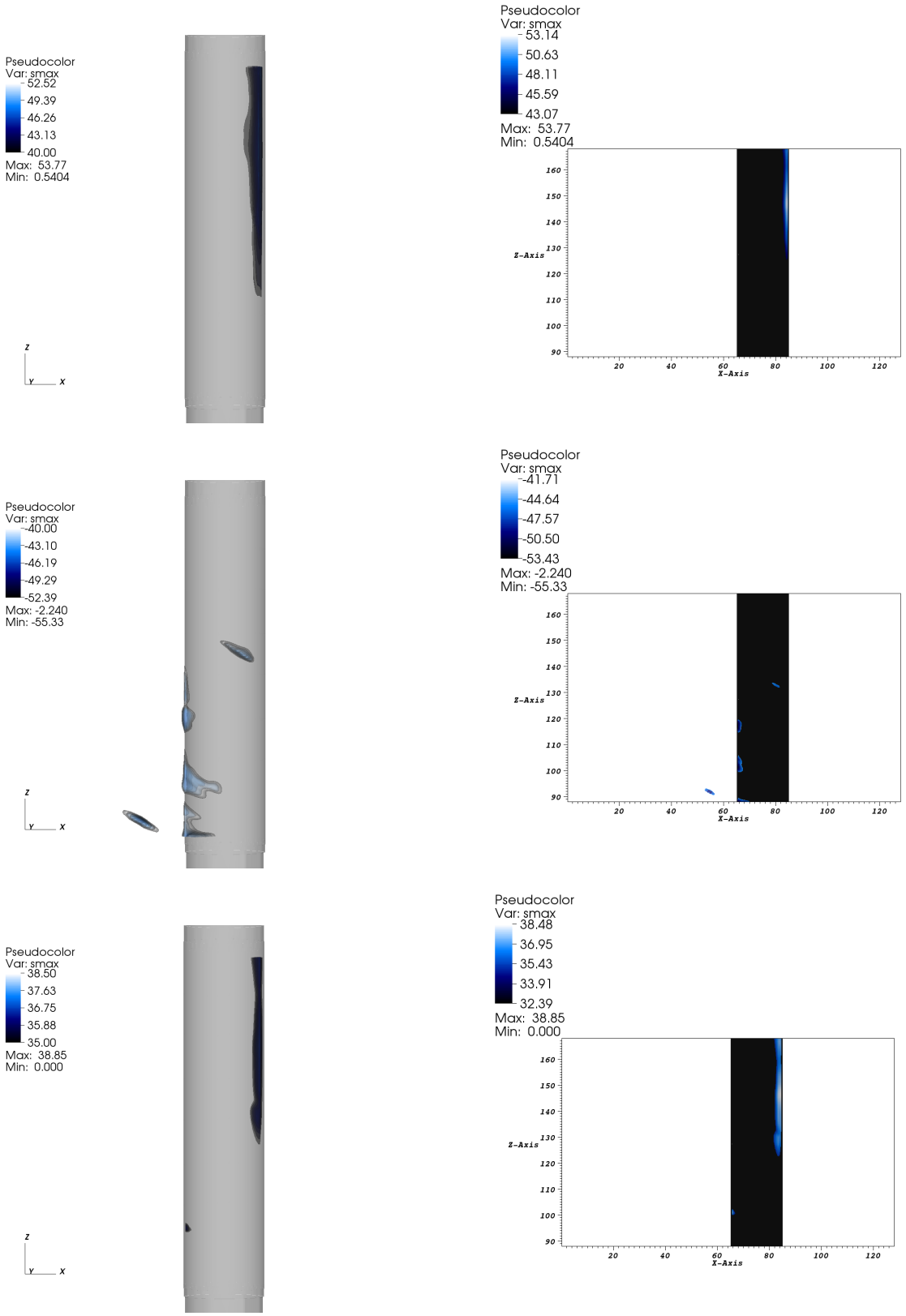

Figure 10.5: Three-dimensional results for 60 degree angles of treatment for a complete cylinder. This figure shows the isosurfaces of maximum compression, tension and shear in the first column with corresponding 2D slices at y=0 in the second column.

10.1.3 Broken Cylinder

The broken cylinder is meant to simulate a break in a bone and give insight about the deposition of energy in the treatment of a non-union. The deposition of stress varies as both the angle and position of the bone are changed.

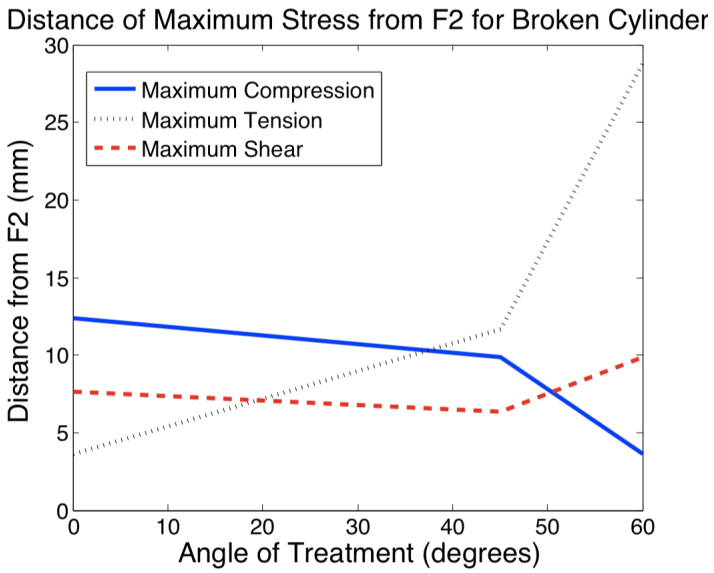

Figure 10.6: A comparison of the location of maximum stress deposition relative to the focus. In this case all of the locations of stress deposition are affected by the angle, but because of the gap, the compression and shear location are less affected by the angle of treatment. Data for plots summarized in Tables (10.4,10.5,10.6)

In the case of the broken cylinder, the maximum stress deposition in the direct experiment is similar to that of the unbroken cylinder, except that the there are two locations of maximal stress deposition on either side of the break. The pressures in the bone are much larger than in the fluid, so the contours of maximum stress are concentrated on either side of the gap. The location on the x-axis is nearly the same as in the unbroken cylinder, and the distances from F2 are also similar.

As the angle of treatment is varied, there is less of a shift in the z-direction for the shear and compressive stresses. This is caused by the impedance difference between the fluid and solid material at the gap. There is also a slight shift in maximum compression and shear stress location along the x-axis due to reflection at the gap. Geometrically, the shape of the regions of compressive and shear stress are quite different from the direct case. Instead of being an ellipsoidal type shape, the regions are compressed into the corner of the lower-half of the cylinder. The region of maximum tension deposition is similar to that of the unbroken cylinder case, though it is also affected by the gap and the tension is concentrated on the upper half of the cylinder.

Stress type	Maximum in absolute value (MPa)	Location (x,y,z)
Compression	56.02 MPa	(78,128,140),(78,128,116)
Tension	-66.92 MPa	(78,128,130), (78,128,126)
Shear	56.14 MPa	(78,128,136), (78,128,136)

Table 10.4: Stresses in broken cylinder for direct wave

Stress type	Maximum in absolute value (MPa)	Location (x,y,z)
Compression	63.06 MPa	(84,128,124)
Tension	-67.3 MPa	(65,128,134)
Shear	47.73 MPa	(81,128,126)

Table 10.5: Stresses in broken cylinder for 45 degree rotation

Stress type	Maximum in absolute value (MPa)	Location (x,y,z)
Compression	55.33 MPa	(78,128,126)
Tension	-52.75 MPa	(65,128,101)
Shear	42.36 MPa	(84,129,124)

Table 10.6: Stresses in broken cylinder for 45 degree rotation

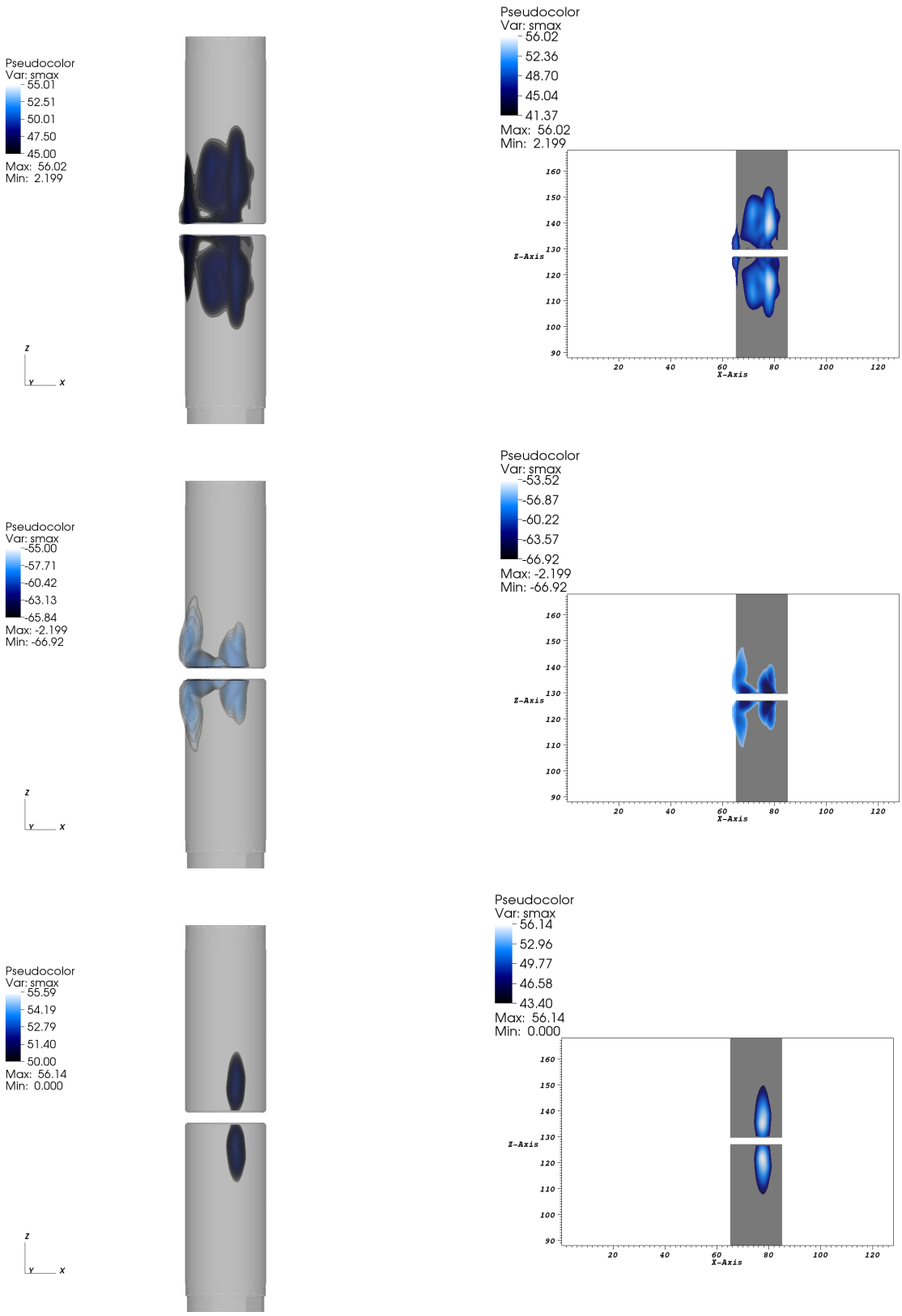

Figure 10.7: Three-dimensional results for the direct treatment of a broken cylinder. This figure shows the isosurfaces of maximum compression, tension and shear in the first column with corresponding 2D slices at y=0 in the second column.

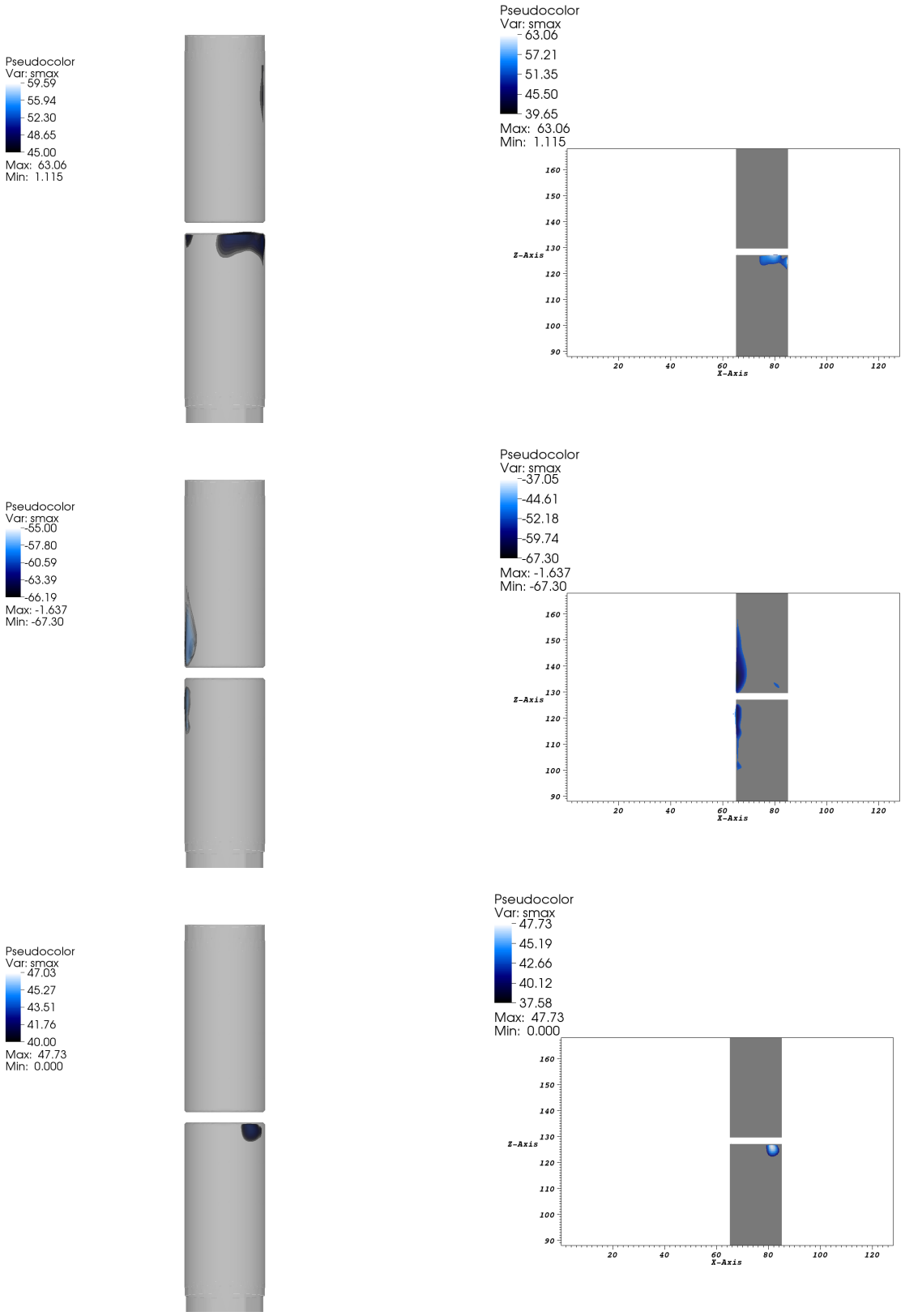

Figure 10.8: Three-dimensional results for the 45 degree treatment of a broken cylinder. This figure shows the isosurfaces of maximum compression, tension and shear in the first column with corresponding 2D slices at y=0 in the second column.

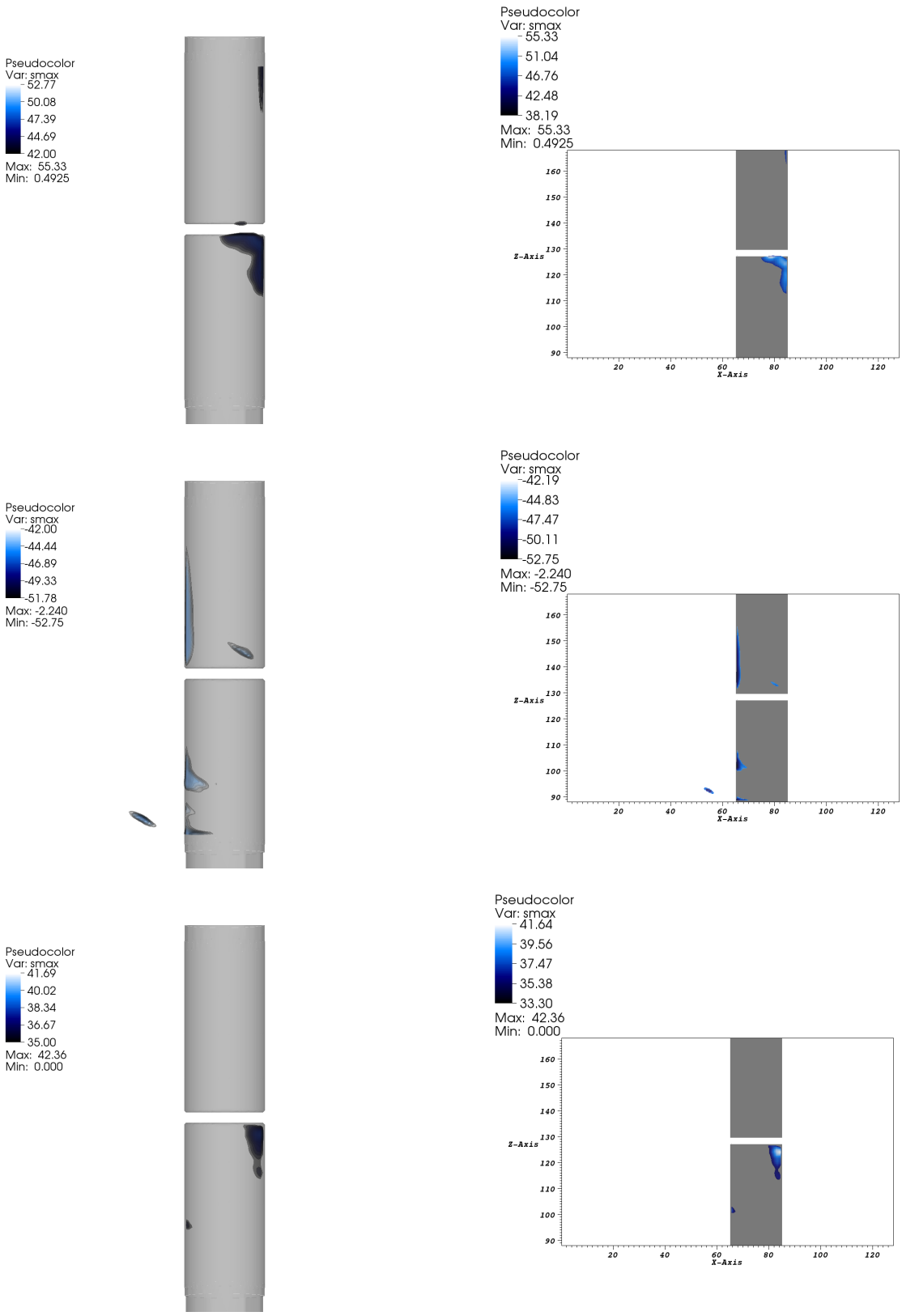

Figure 10.9: Three-dimensional results for the 60 degree treatment of a broken cylinder. This figure shows the isosurfaces of maximum compression, tension and shear in the first column with corresponding 2D slices at y=0 in the second column.

10.1.4 Shifted Broken Cylinder

For this experiment, we shifted the broken cylinder so that the focus of the device was 5mm closer to the leading edge of the cylinder. This was to investigate the change in stress deposition when the device is shifted laterally as well as changing the angle of treatment.

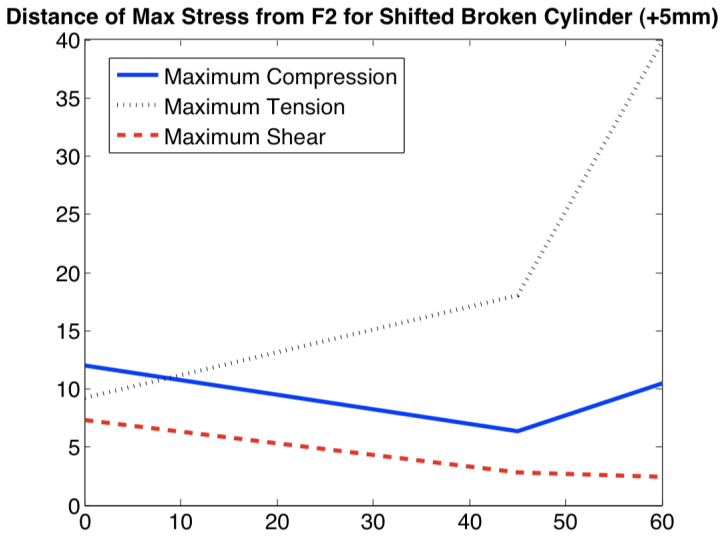

Figure 10.10: A comparison of plots of the location of the maximum stresses relative to the focus of the device for a positive 5mm shift in the cylinder relative to the focus. Data from Tables (10.7,10.8,10.9)

In the direct case, one thing we can note here is the difference in the magnitude of the stresses that is a result of the energy of the wave not being as focused before striking the cylinder. Again there are two locations for maximum stress, shifted approximately 5mm in the the positive direction. The overall trend in this case is the same as that in the broken cylinder case above, with the exception of larger distances from F2, as would be expected from the shift in location of the device. The shape and location of the maximum stress contours relative to the cylinder are similar in both the shifted and unshifted broken cylinders.

It is also interesting to note that in the case of the region of maximum tension, the energy is no longer concentrated on the lower half of the cylinder. In this case the region of maximum tension is actually larger in the lower half of the cylinder, which is due to the shift relative to F2.

Stress type	Maximum in absolute value (MPa)	Location (x,y,z)
Compression	59.02 MPa	(74,128,140))
Tension	-71.36 MPa	(64,128,126)
Shear	55.87 MPa	(73,128,135)

Table 10.7: Stresses in broken cylinder for direct wave shifted by $+5mm$

Stress type	Maximum in absolute value (MPa)	Location (x,y,z)
Compression	65.65 MPa	(80,128,124)
Tension	-73.34 MPa	(60,128,118)
Shear	49.02 MPa	(76,128,126)

Table 10.8: Stresses in broken cylinder shifted by $+5mm$ with 45 degree rotation

Stress type	Maximum in absolute value (MPa)	Location (x,y,z)
Compression	55.22 MPa	(79,125,118)
Tension	-67.43 MPa	(63,128,90)
Shear	45.07 MPa	(79,129,124)

Table 10.9: Stresses in broken cylinder shifted by $+5mm$ with 60 degree rotation

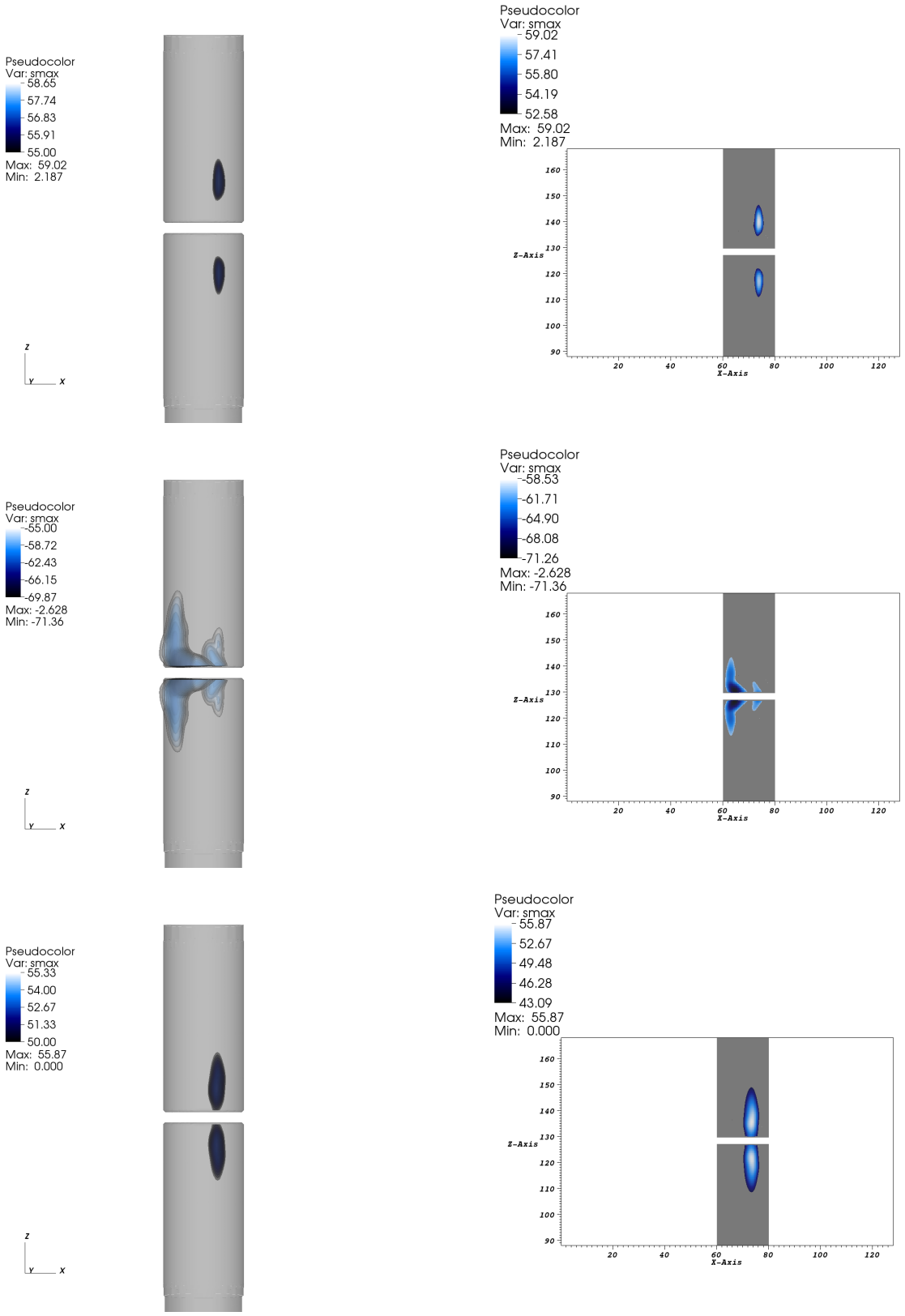

Figure 10.11: Three-dimensional results for the direct treatment of a broken cylinder shifted by $+5mm$. This figure shows the isosurfaces of maximum compression, tension and shear in the first column with corresponding 2D slices at y=0 in the second column.

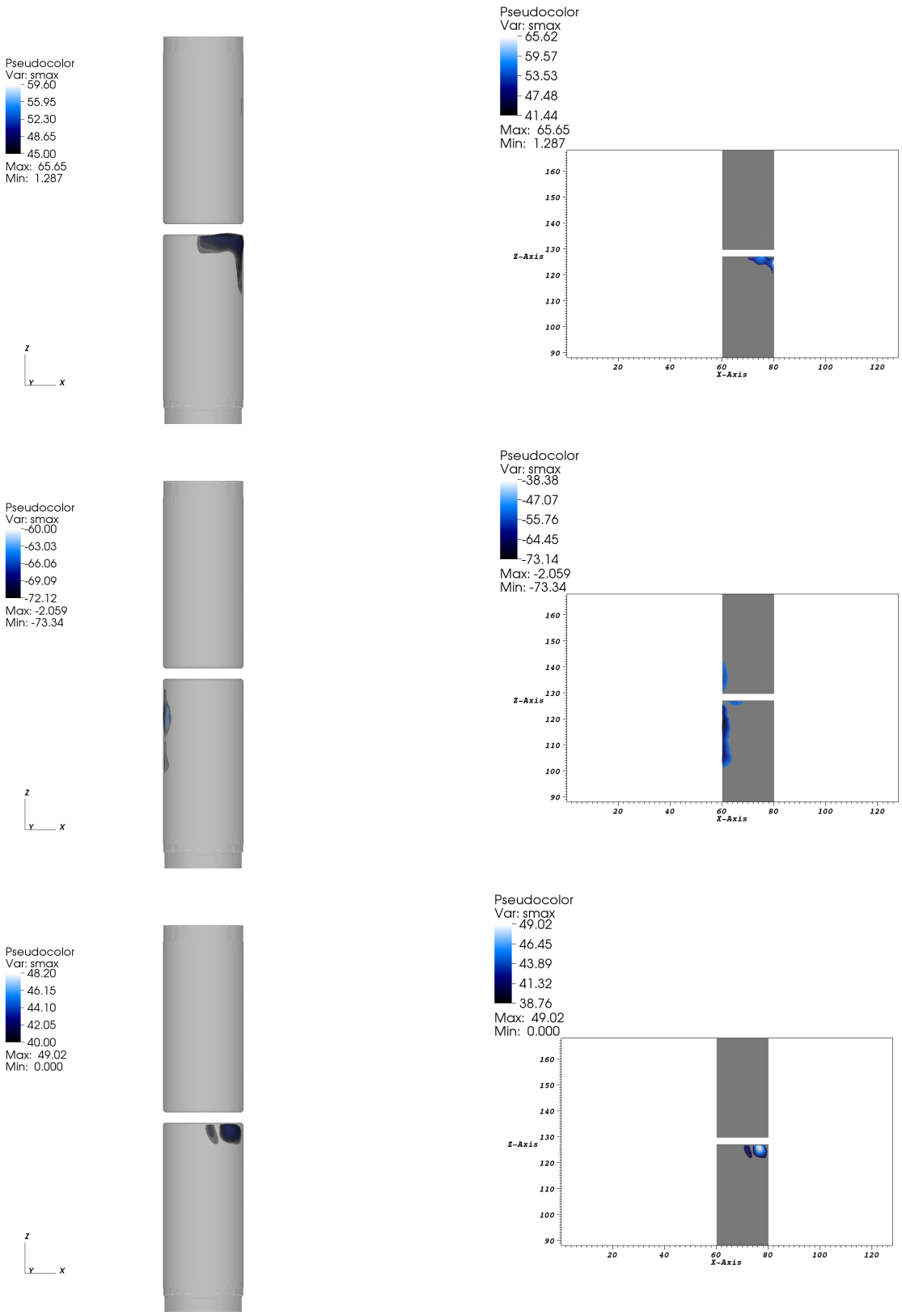

Figure 10.12: Three-dimensional results for the treatment of a broken cylinder shifted by $+5mm$ rotated by 45 degrees. This figure shows the isosurfaces of maximum compression, tension and shear in the first column with corresponding 2D slices at y=0 in the second column.

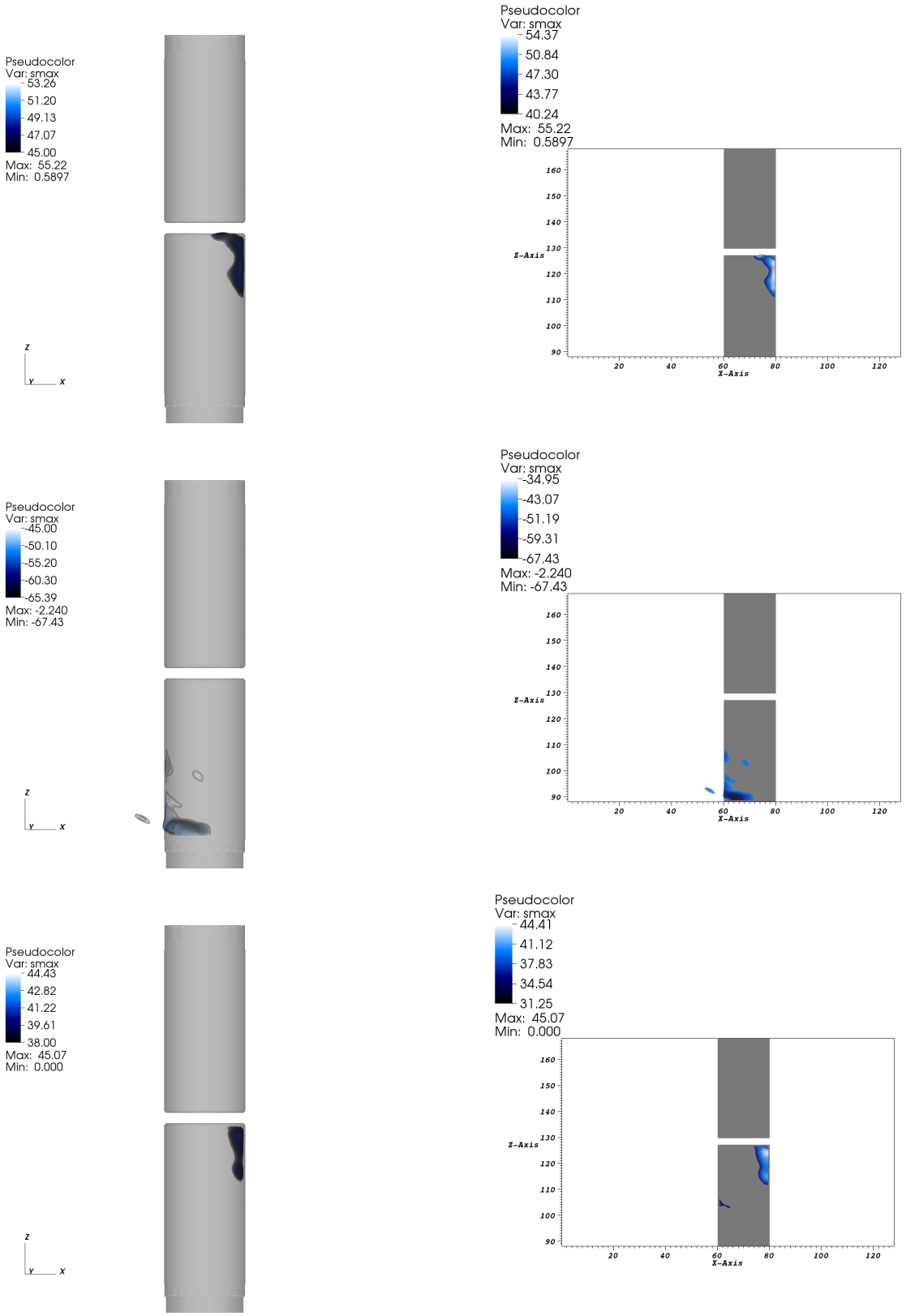

Figure 10.13: Three-dimensional results for the treatment of a broken cylinder shifted by $+5mm$ rotated by 60 degrees. This figure shows the isosurfaces of maximum compression, tension and shear in the first column with corresponding 2D slices at y=0 in the second column.

Direct Shock Wave - Negative 5mm Shift

The following set of experiments were done with a broken cylinder that was shifted $-5mm$ relative to the focus. The first figure summarizes the shift in location of the maximum compression, tension and shear as a plot of distance as a function of angle. The second figure summarizes the change in energy deposition as a function of the angle of treatment.

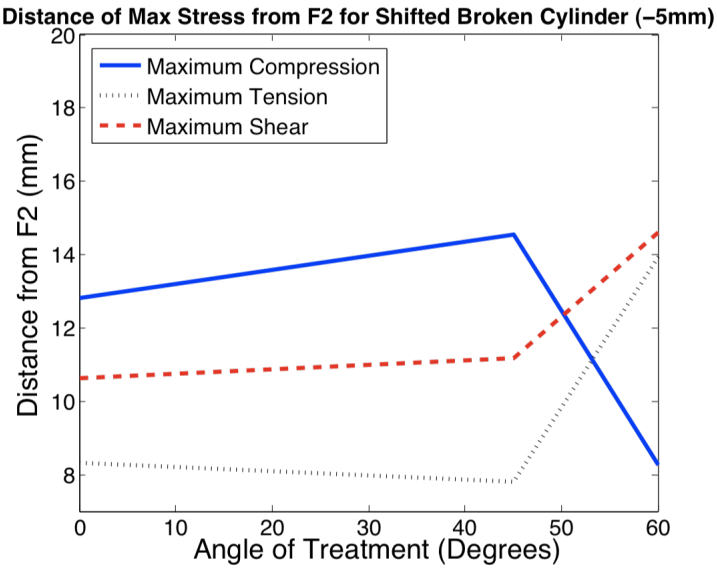

Figure 10.14: A comparison of the location of maximum stress deposition for a negative 5mm shift in the cylinder relative to the focus. Data from Tables (10.10,10.11,10.12)

The locations of the maximum stress relative to the focus are similar in distance to those in the positive 5mm shift case because the geometry of the cylinder has the largest effect on the locations of maximal stresses. The overall strength of the pressures that are deposited are smaller than the case where the cylinder was centered precisely at F2, this is due to attenuation of the wave past the focus.

The shape and location of the maximum stress contours are similar to the two previous cases of the broken cylinder. In this case the tension is again concentrated in the upper half of the cylinder as in the unshifted case.

Stress type	Maximum in absolute value (MPa)	Location (x,y,z)
Compression	58.41 MPa	(83,128,138)
Tension	-67.99 MPa	(70,127,126)
Shear	56.74 MPa	(83,128,121)

Table 10.10: Stresses in broken cylinder for direct wave shifted by $-5mm$

Stress type	Maximum in absolute value (MPa)	Location (x,y,z)
Compression	59.04 MPa	(89,128,124)
Tension	-68.84 MPa	(70,128,134)
Shear	42.64 MPa	(86,128,126)

Table 10.11: Stresses in broken cylinder shifted by $-5mm$ for 45 degree rotation

Stress type	Maximum in absolute value (MPa)	Location (x,y,z)
Compression	52.68 MPa	(83,128,126)
Tension	-57.17 MPa	(70,128,141)
Shear	39.04 MPa	(89,129,124)

Table 10.12: Stresses in broken cylinder shifted by $-5mm$ for 60 degree rotation

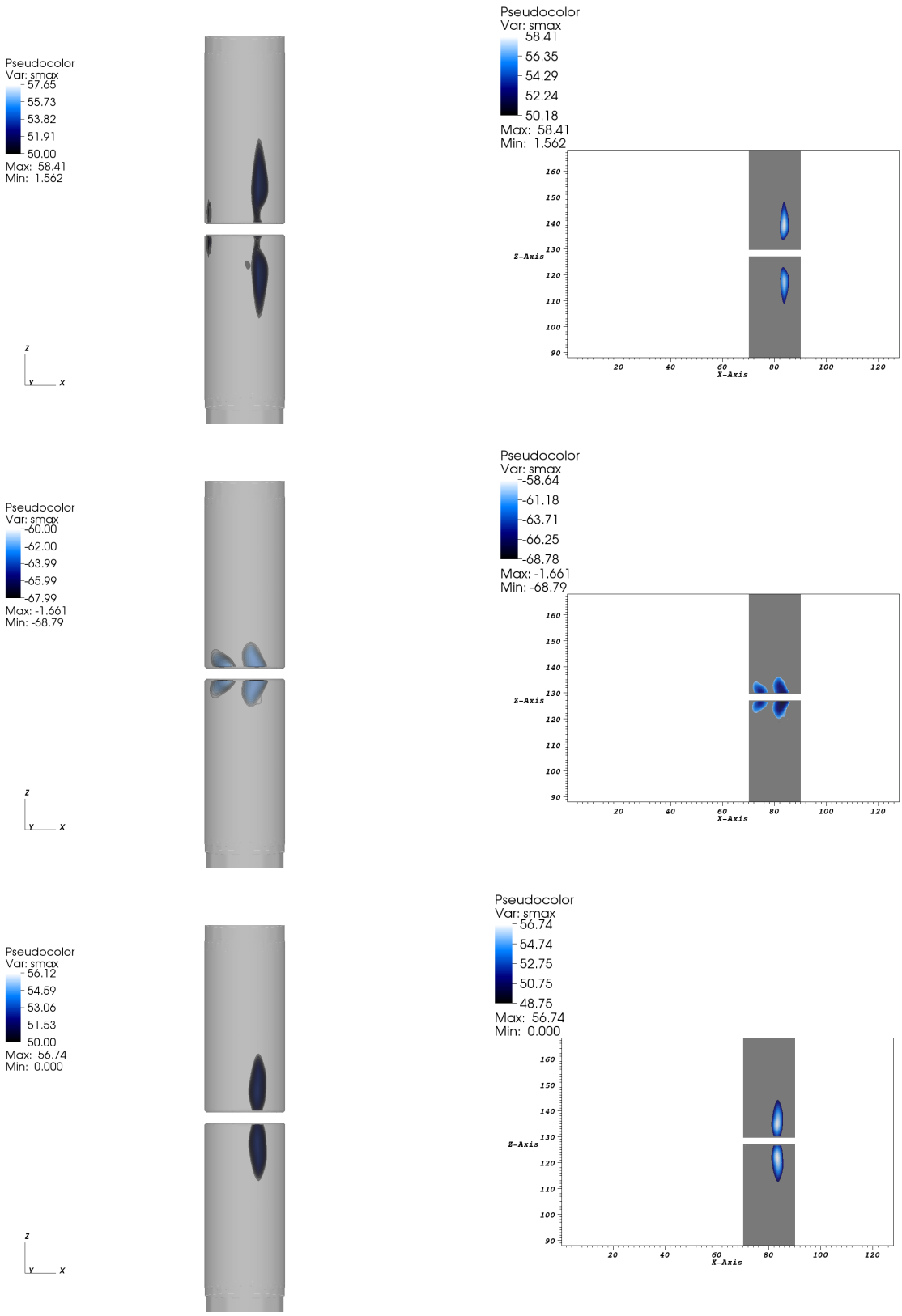

Figure 10.15: Three-dimensional results for the direct treatment of a broken cylinder shifted by $-5mm$. This figure shows the isosurfaces of maximum compression, tension and shear in the first column with corresponding 2D slices at y=0 in the second column.

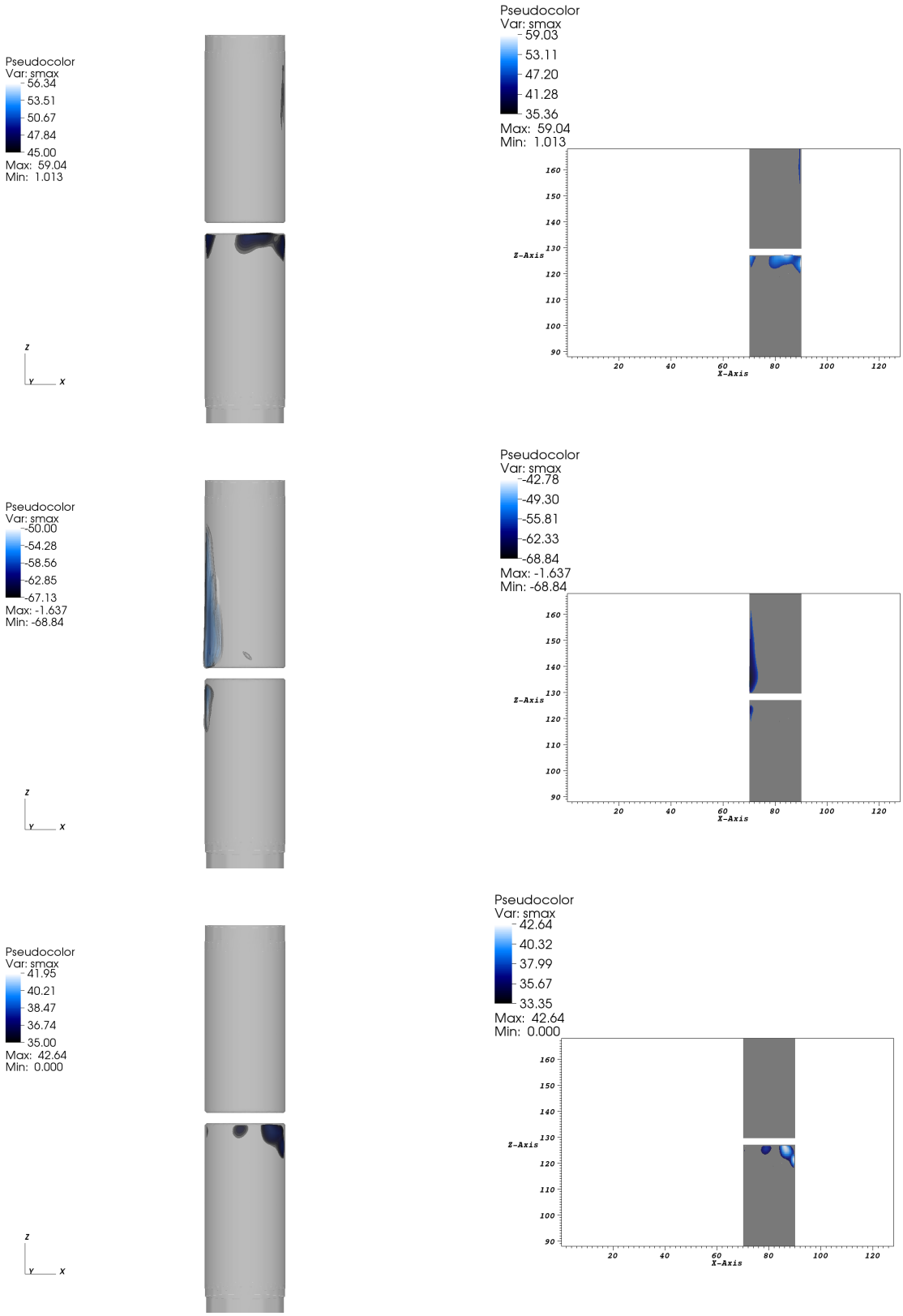

Figure 10.16: Three-dimensional results for the treatment of a broken cylinder shifted by $-5mm$ rotated by 45 degrees. This figure shows the isosurfaces of maximum compression, tension and shear in the first column with corresponding 2D slices at y=0 in the second column.

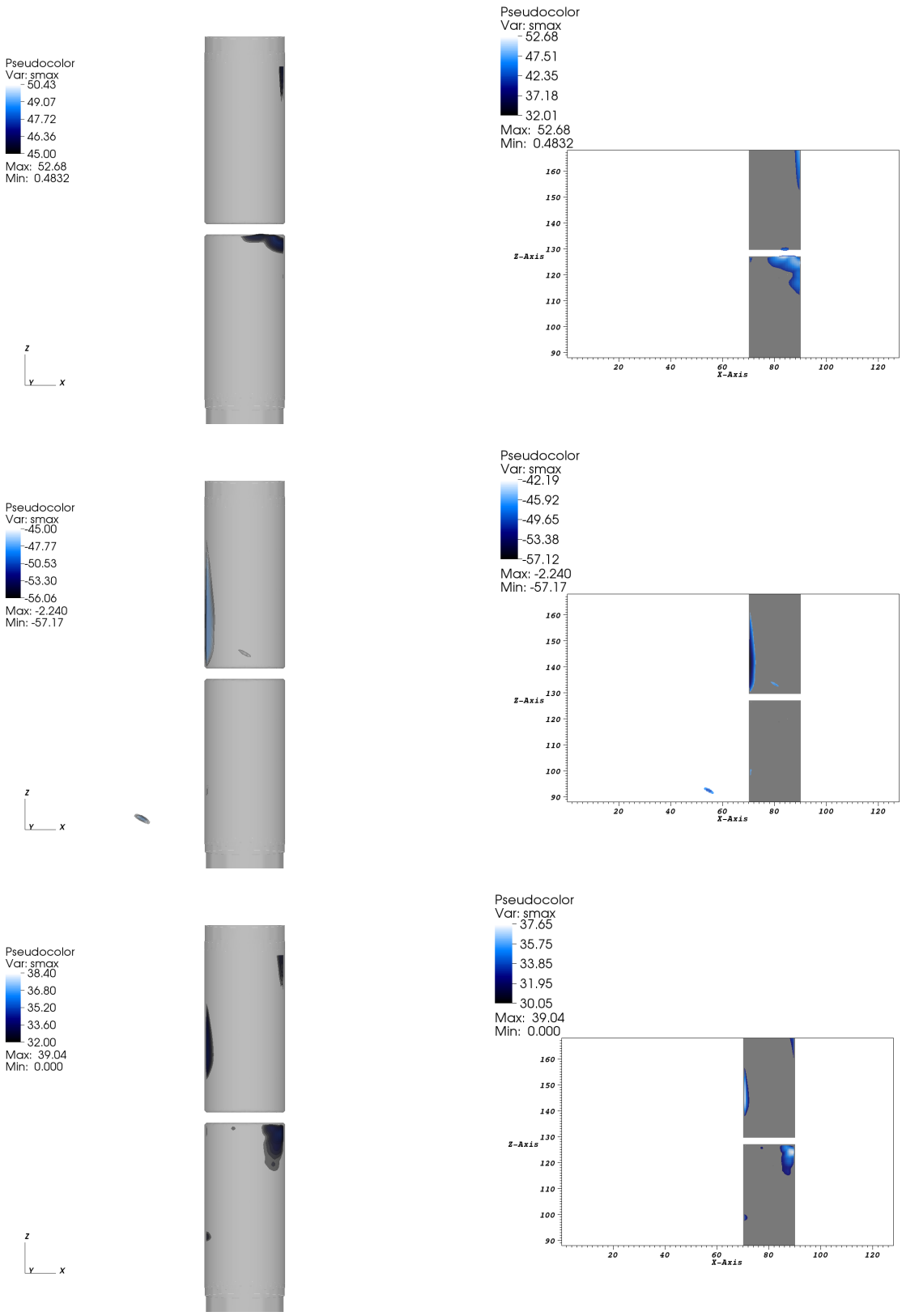

Figure 10.17: Three-dimensional results for the treatment of a broken cylinder shifted by $-5mm$ rotated by 60 degrees. This figure shows the isosurfaces of maximum compression, tension and shear in the first column with corresponding 2D slices at y=0 in the second column.

10.2 Tissue

There are references in the literature that contain measurements for idealized biological materials [70, 61, 36]. Since we can easily vary the material properties of the grid cells in our model, we used these measured parameters to investigate their effect on the shock wave propagation.

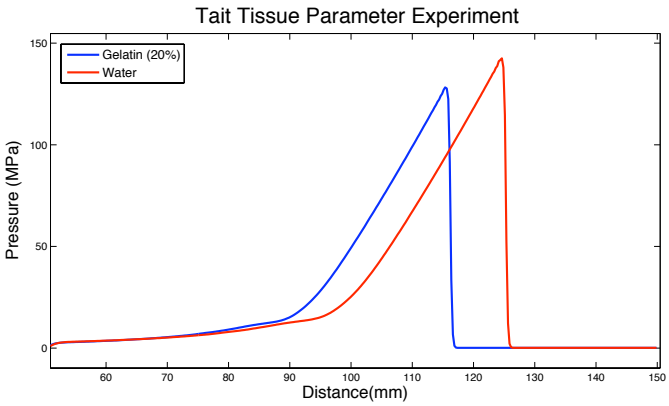

Figure 10.18: Comparison of a wave propagating through water (blue curve) and tissue (red curve). The wave propagating through tissue was both attenuated and moved at a slower speed as we would expect from the form of the sound speed.

In this series of calculations I compared the focal region and pressure waveform measured near F2 to what would be obtained using pure water. I varied the thickness of the tissue region and in one calculation included a wall with the material parameters of bone. These calculations were all performed using the axisymmetric form of the Lagrangian Euler equations. The maximum expected pressure at F2 in just water is 18 MPa and the maximum compression region should contain F2.

One conclusion from this series of experiments is that the material properties used for the tissue do have an effect on the wave propagation, but not as much as the bone material. This is due to the relative difference in material properties. The difference between tissue and water is not as great as the difference between tissue and bone, therefore the wall will have a larger effect on the focal region and therefore, a larger effect on our modeling efforts.

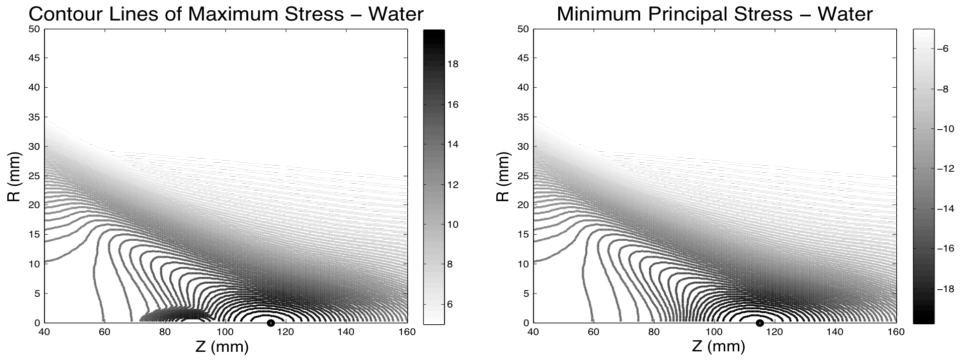

Figure 10.19: Included for ease of comparison. The calculated focal regions for maximum compression and tension in water alone. Note that maximum principal stress corresponds to maximum negative pressure and minimum principal stress corresponds to maximum positive pressure.

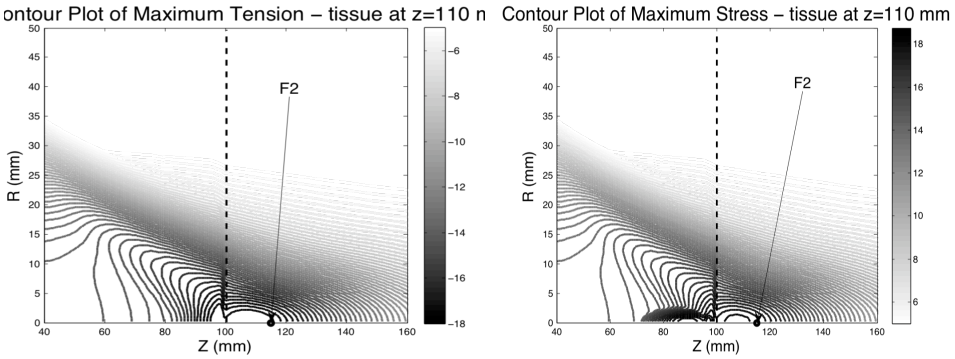

Figure 10.20: The material is water to the left of z=100 and tissue-like gel to the right. We use the parameters for the Tait equation of state from Nakahara 2008 for 20% gel.

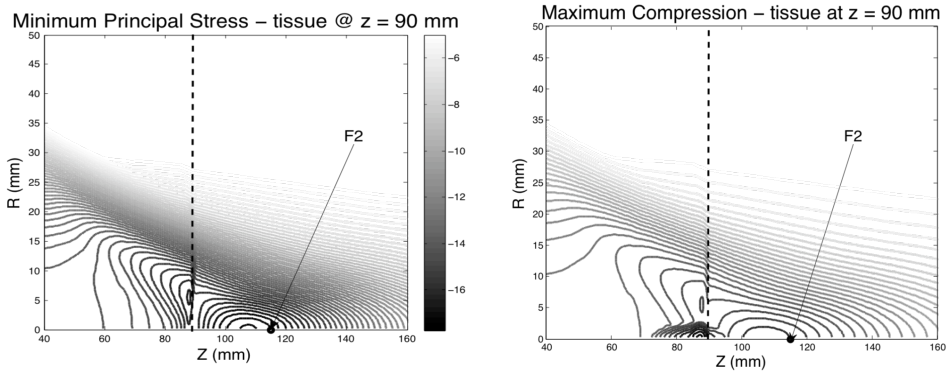

Figure 10.21: The material is water to the right of z=90 and tissue-like gel to the left. We use the parameters for the Tait equation of state from Nakahara 2008 for 20% gel.

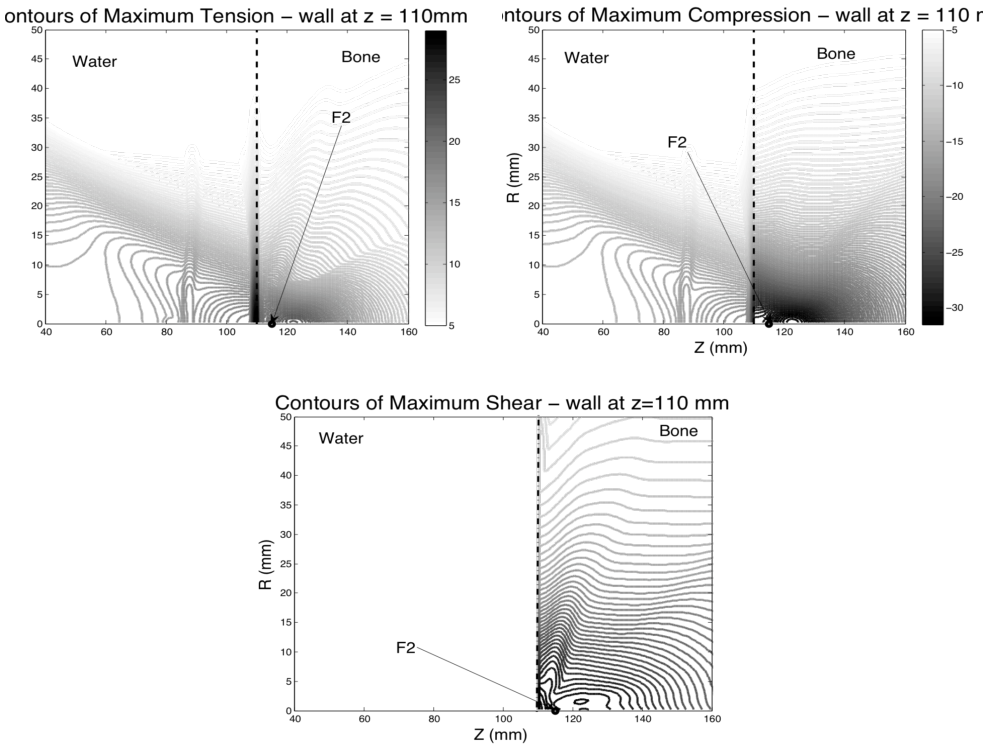

Figure 10.22: The material is water to the right of z=110 and isotropic homogeneous bone to the left. The parameters for cortical bone can be found in Table 9.1. Since bone has a non-zero shear modulus, we also calculate the contours of maximum shear stress.

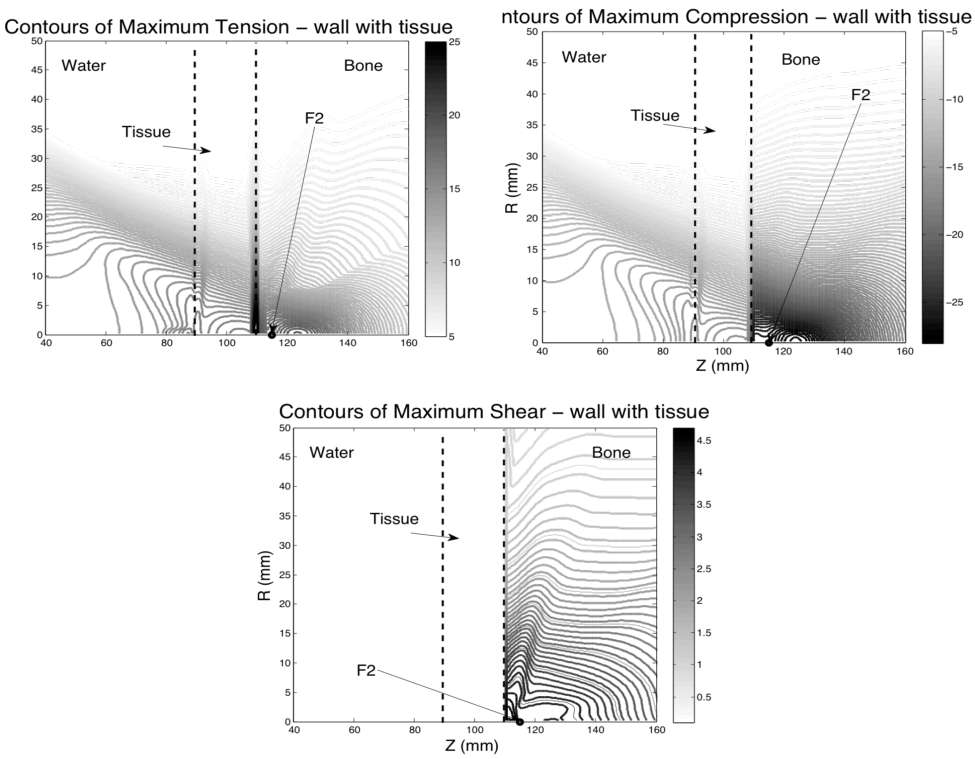

Figure 10.23: The material is water to the right of z=90, tissue between z=90 and z=110, and bone to the right of z=110. We performed this calculation in order to investigate the effect of tissue on maximum, compression, tension and shear.

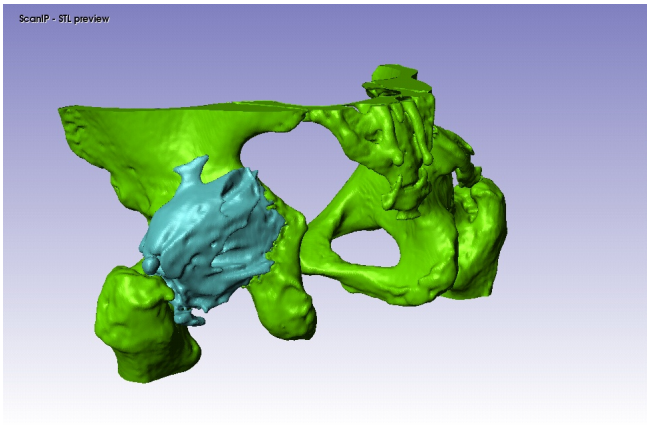

Figure 10.24: Hip heterotopic ossification

10.3 Heterotopic Ossification

We have obtained 3D bone geometry data from Dr. Michael Chang that contains a hip bone and ossification, we used our code to look at the difference in maximal stresses when the ossification is treated at two different angles. In the first few figures we show the calculation performed on the actual ossification geometry reconstructed from CT data, as seen in Figure 10.24. The experiments show that the two treatments have different locations of maximal stress deposition, but this is dependent upon the geometry of the ossification.

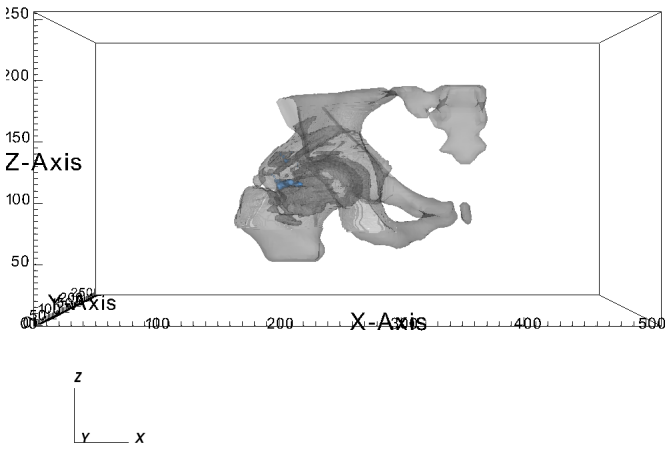

a)

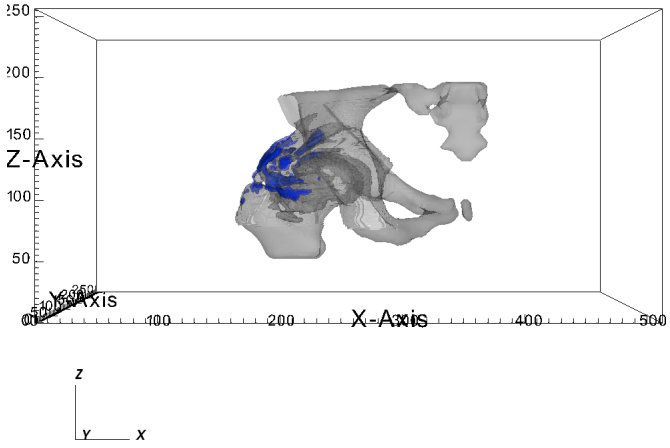

b)

Figure 10.25: Isosurface of a) Maximum Compression and b) Maximum Tension in the HO shot directly.

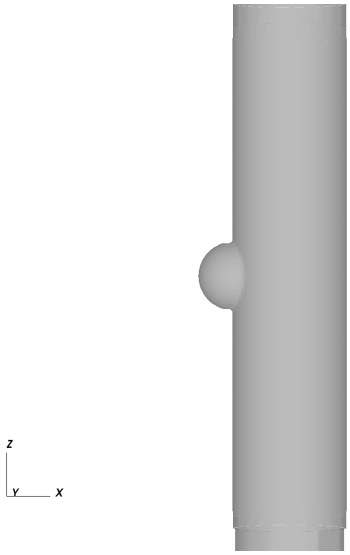

Figure 10.26: Idealized ossification - sphere embedded in a cylinder

10.3.1 Idealized Ossification

In order to better understand the implications of the composition of the heterotopic ossification as well as the strength in attachment to the hip bone on the regions of maximum stress, we also performed three idealized calculations. In these calculations, the heterotopic ossification is represented by a sphere embedded into a cylindrical bone. Using this simplified geometry, we can easily vary the material properties of the sphere, as well as its attachment to the cylinder by the introduction of a gap between the two objects. The use of this idealized geometry also allows for straight-forward comparison with the cylindrical geometry considered in the nonunion experiments. We should note here that these are just one set of calculations performed on one idealized geometry. For completeness, subsequent experiments should be performed on geometries with ossifications that vary in size and shape.

The presence of the ossification had a greater effect on the region of maximum tension, which makes sense because the greatest tensile stresses are present at the first interface between the bone and fluid. The compressive stresses were less affected, but there was an additional small region of compressive stress that was concentrated at the corners where the sphere intersects the cylinder.

The strength of attachment to the bone is important in predicting where the maximum stresses will be deposited. It is interesting to note that in the case of maximum tension, the gap created a buffer region where there was less tensile stress. On the other hand, larger compressive stresses were generated within the gap. The presence of the gap had very little affect on the shape of the shear stress region and location. The magnitudes of all stresses were decreased by the presence of the gap.

Changing the material properties of the ossification had small effect on the location and shape of the maximum shear and compressive stresses, but a large effect on the location of the maximum tensile stress. In the case of maximum tension, the stress in this case is concentrated at the interface between the ossification and bone, as opposed to the interface between the ossification, bone and water. This has to do with the relative strength in impedance mismatch between the two materials.

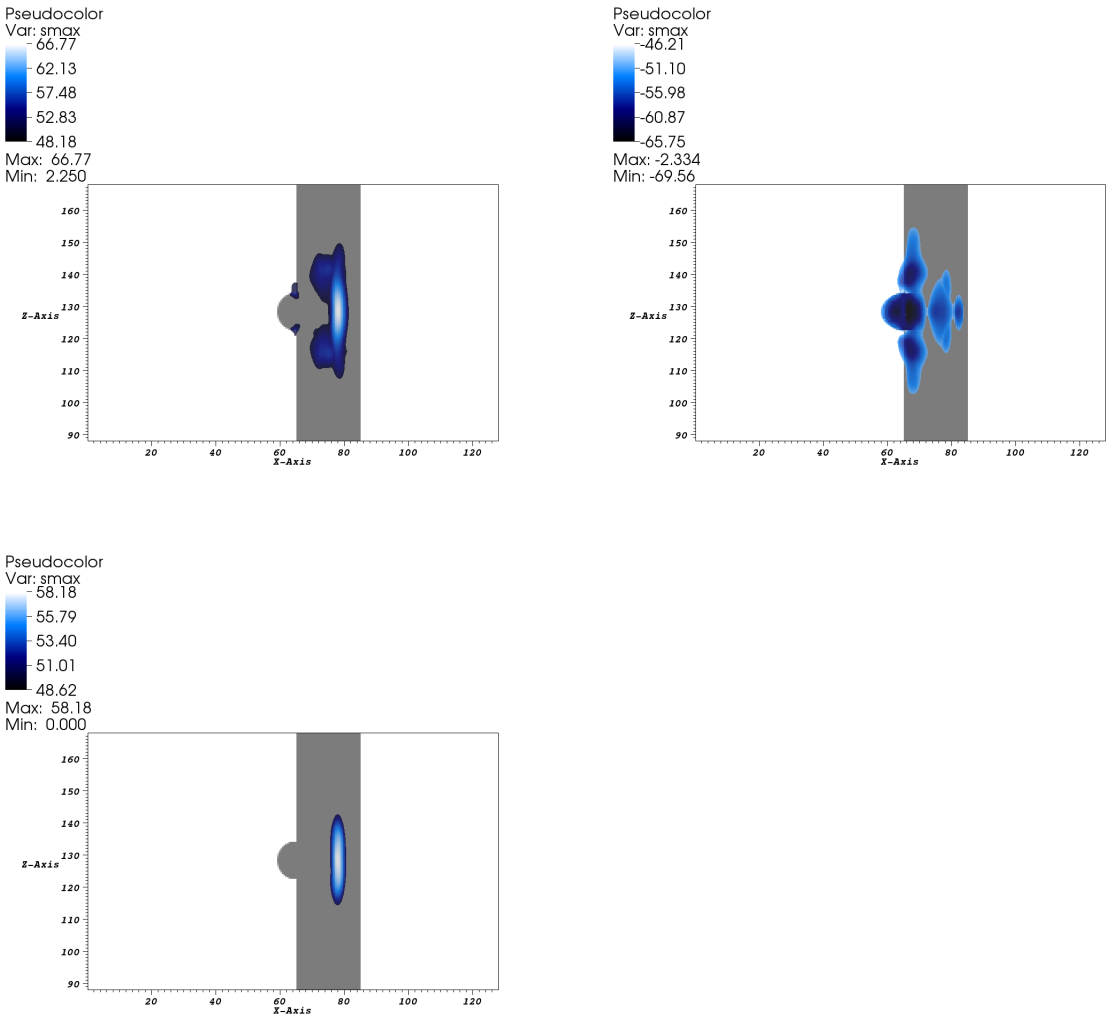

Figure 10.27: Idealized ossification - Isosurface of Max Compression, Tension and Shear

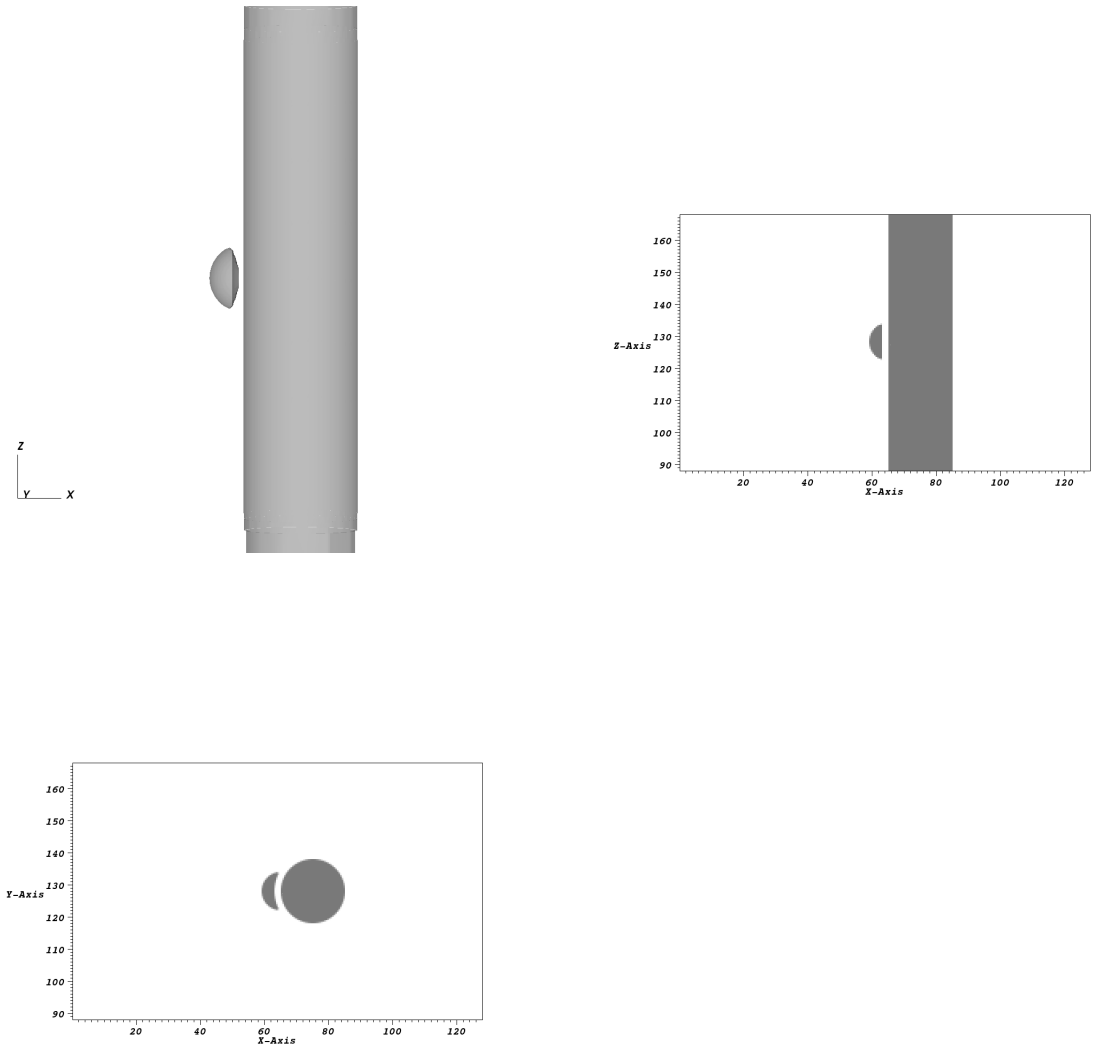

Figure 10.28: Idealized ossification with a gap between the ossification and the bone.

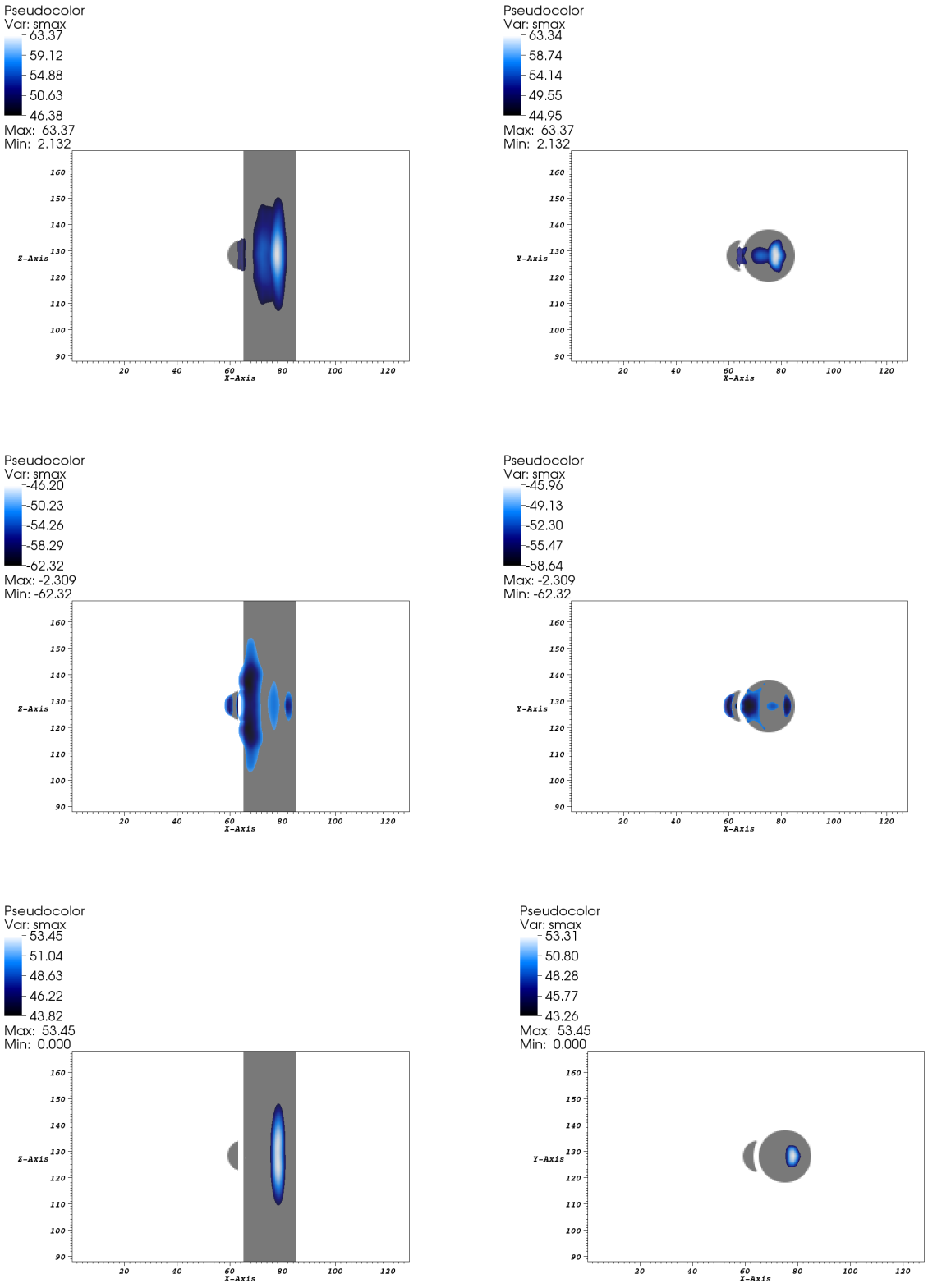

Figure 10.29: Idealized ossification with a gap - Isosurface of Max Compression, Tension and Shear

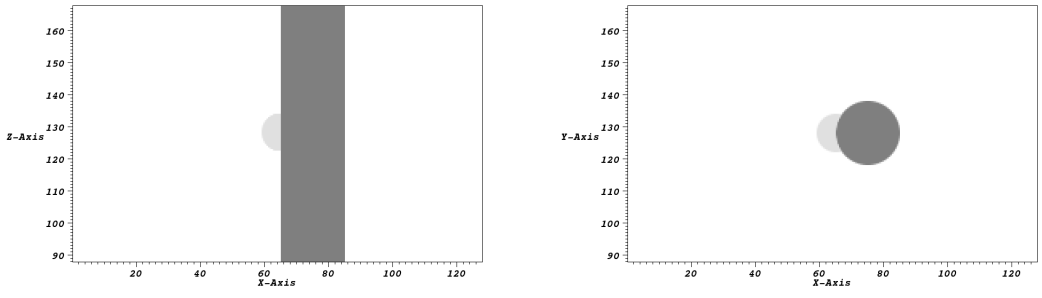

Figure 10.30: Idealized ossification where the ossification has different material properties from the bone cylinder.

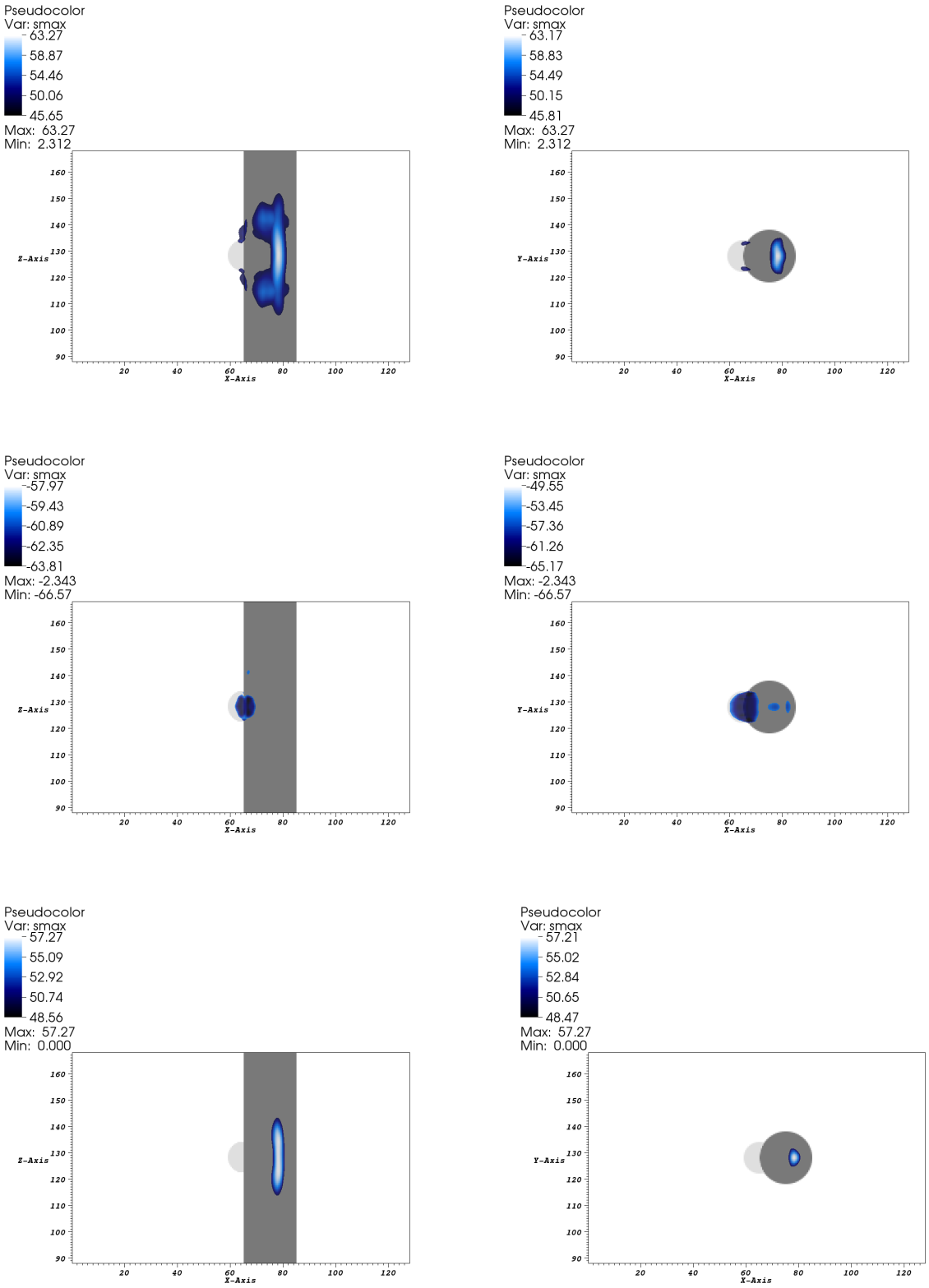

Figure 10.31: Two-dimensional slices of heterotopic ossification with material properties that differ from the bone cylinder.

Chapter 11

CONCLUSIONS

11.1 Summary

In this work we have developed a mathematical model and numerical scheme for the simulation of extracorporeal shock wave therapy. We have taken the Euler equations with the modified Tait equation of state in a Lagrangian frame. This form of the equations allows us to model the wave motion in the solid and fluid with the same set of equations by varying the stress-strain relationship.

In Chapter 2, we provided background on the physics of shock wave therapy and mathematical models for biological tissues. In Chapter 3 we provided details on the numerical solution of hyperbolic systems of partial differential equations using finite volume methods. As a specific example we include a detailed solution of the one-dimensional acoustic equations in heterogeneous materials. Then in Chapters 4 and 5 we provide background on the Euler equations and linear elasticity as both are used in the model of ESWT.

Details are provided on the system of equations for the Lagrangian form of the Euler equations in Chapter 6. We demonstrate that assuming that the displacements in the calculation are small, the density in each grid cell will remain nearly constant, and this form of the Euler equations is equivalent to the elasticity equations.

Further details on the numerical methods used to solve these equations are included in Chapter 7. We also provide the motivation for using adaptive mesh refinement by considering the effect of grid size on resolution of the pressure wave. A minimum grid of 0.25mm is required in order to resolve the shock wave. This would be computationally intractable without the use of a refined grid only near the pressure wave and a coarse grid in the rest of the domain. There is a clear region for refinement near the shock, so we use error in the pressure as our refinement criteria. Furthermore, by using ChomboClaw, we are able to run three-dimensional calculations in parallel.

The connection between birefringence, photoelasticity and laboratory experiments is introduced in Chapter 8. We also include the derivation of the photoelastic equations that describe changes in the polarization of the electric vector upon passing through a birefringent material. These equations are solved numerically using the stresses calculated in our simulation of ESWT and used to obtain the fringe patterns observed in laboratory experiments. We validated our calculations using the analytic expression for stress in a diametrically compressed disc. This is a well-known case that is typically used for the calibration of photoelastic experiments. It is interesting to note that numerical integration of this system has some challenges because the eigenvalues are purely imaginary and can be on the order of $100i$, so the stability region for the method must contain the entire imaginary axis.

In Chapter 9 we provide results that validate our model and numerical approach. We provide gauge calculations validating that we obtain the correct pressure wave form at F2. We also keep track of the maximum compression, tension and shear for comparison with published data regarding the focal region of the HM3 Dornier lithotripter[14]. The three-dimensional results clearly show that we obtain the correct focal region about F2. In this chapter we also validated the shock wave propagation by calculating the pressure wave propagation in a cylinder and comparing the results with laboratory experiments. We were able to use our photolelastic post-processing technique to produce plots that agree reasonably well with the photographs.

In addition to these validation techniques we compared calculations on a symmetric geometry,

the sphere, in order to verify that the focal regions are the same in both cases. We found that the focal regions were essentially identical, but the values for maximum peak over and under pressure were not the same. This is due to some attenuation caused by rotation of the initial condition. For this reason we did not compare maximal stress values as we varied the angle of treatment, but we were able to compare the various focal regions in order to draw conclusions about the treatment. of non-unions.

In Chapter 10 we used the code that we have developed to make predictions about the treatment of non-unions using ESWT. Clinicians have a certain amount of freedom when applying shock waves using a hand-held ESWT device. The angle of application as well as the location of the focus relative to the break will influence the amount of energy that is deposited and the location. We found that there is a corresponding shift in the maximal stress deposition when the device is shifted laterally, as indicated by moving the bone in the positive or negative x-direction relative to the focus.

When the angle of treatment is varied by rotation about the y-axis, the location of the maximum stresses will change relative to the z-axis. When the bone is broken, there is an interface separating the two halves of the bone that causes the stress to be deposited primarily in the lower half, except in the case of maximum tension. The location of maximum tension will change depending upon the lateral and angular shift, and more of the stress may be deposited in the upper half of the bone.

One of the benefits of our model is the incorporation of different materials through the stress-strain relationship. Parameters for the Tait equation of state have been measured in the laboratory for different biological-like materials. We have incorporated these tissue parameters into our model and studied the subsequent changes on the pressure wave form. We found that the amplitude of the wave is decreased and is slightly slower in arrive at F2, which corresponds well to measurements taken in a pig liver[15]. We then used this model to examine changes in the stress distribution when the bone from the nonunion is surrounded by soft tissue and found that the tissue had a much smaller effect on the pressure distribution than the bone. This may indicate that the tissue modeling is less important when considering the pressure distribution at the bone-fluid interface. However, it may be much more important for obtaining the correct attenuation within a more accurate model of the bone containing fluid-filled cavities.

In the case of heterotopic ossifications, a great deal is still unknown about their composition and attachment to the bone surface. Our preliminary calculations indicate that treatment from different angles will induce stresses at different locations in the HO, which is due to the different geometry and interfaces encountered by the wave. In order to better understand the importance of the attachment strength and material properties, we performed experiments where these properties were varied. We found that the location of the maximum tensile stress was greatly affected by the change in material properties. The gap influenced the location of both the maximum tensile and compressive stresses. A secondary region of compressive stress was deposited within the gap, which was devoid of strong tensile stresses. We also found that in all cases, the maximum shear stress was largely unaffected. However, if you remove shear stresses from the model, the overall magnitude of compressive and tensile stress in the system is weakened, as seen in the work of Sapozhnikov [72]. Therefore, shear stresses do play a fundamental role in these calculations and should be included.

The results from this thesis and subsequent work done using the model we have presented will help provide insight to clinicians as they consider ways to optimize ESWT treatments.

11.2 Future Work

11.2.1 Application to additional treatments

One common use for ESWT is the treatment of plantar fasciitis [63]. It would be interesting to obtain a CT scan of the calcaneous in order to investigate the treatment of the plantar fascia from two different angles. This is also a treatment with only a small amount of soft tissue between the

treatment area and the skin, but the the treatment is thought to have the largest effect in the soft tissue [64, 63], so it would be interesting to combine this with a better model for thick tendon [33].

Traumatic brain injury (TBI) is the result of head trauma that causes damage to the brain, usually after repeated exposure to explosions or concussive events[34]. It has the potential to cause symptoms slowly over the period of months, the cause of which is not yet well-understood. Some proposed mechanisms of this delay are axonal damage to the brain and intracranial bleeding [26, 34]. If left untreated, it can cause severe limitations in a persons physical and cognitive abilities. TBI has become a prevalent problem as more military personnel are exposed to improvised explosive devices (IEDs) in the field, and as the survival rate increases. Researchers would like to better understand the effect of blast waves and repeated collisions on the brain in an effort to protect soldiers and athletes from TBI. Numerically there are issues with modeling the air/skull interface present in modeling blast waves originating from an IED. However, our code could be used to model the interaction of a shock wave at the brain-skull interface, which is also important for understanding TBI.

11.2.2 Model Improvements

There are a wide variety of material properties for tissue that are available in the literature, but it is unclear what the effect is on the wave propagation. We used published data for our calculations, but it would be interesting to know how sensitive our results are to perturbations in these data. In the case of the heterotopic ossification, we tested two different cases where the material properties in the bone and ossification were the same, and where the two were significantly different. This did not have a large effect on the location of shear and compressive stress deposition in the calculation, but with a larger object, such as the actual heterotopic ossification, the different properties could have a greater impact.

We have considered three different treatment angles in our model for a non-union. We found that this has a strong effect on the deposition stresses in the calculation. Using this as an optimization criteria, we could set up our code in such a way that we could determine the optimal angle for treatment.

As discussed in Chapter 2, the structure of bone is highly heterogeneous in nature. We have access to some trabecular bone segments that have been scanned by researchers in the Mechanical Engineering department at UC Berkeley. It would be interesting to take an averaged value of the material properties of bone, determined through a homogenization procedure, and use that for a homogeneous segment of bone. Then we could compare results from that experiment to modeling the a wave propagating through the porous bone structure. Our model for ESWT enables us to model the bone and fluid in the same model, but care must be taken to accurately model the fine-scale structures.

11.2.3 Additional applications

We have developed a three-dimensional code for modeling wave propagation in fluids and solids in the event that the displacements in each case are small. The applications mentioned above are biological in nature, but there many potential projects that we yet to consider. The software, experimental data and documentation for this work will be available online [29], so it can be used by anyone interested in solving a problem of this nature.

BIBLIOGRAPHY

[1] Hillar Aben. *Integrated Photoelasticity.* McGraw-Hill, 1979.

[2] S. Amsel, A. Maniatis, M. Tavassoli, and W.H. Crosby. The significance of intramedullary cancellous bone formation in the repair of bone marrow tissue. *The Anatomical Record*, 164(1):101–111, 1969.

[3] M.A. Averkiou and R.O. Cleveland. Modeling of an electrohydraulic lithotripter with the KZK equation. *Journal for the Acoustical Society of America*, 106(1):102–112, 1999.

[4] Shock Wave Therapy BC. `http://www.shockwavetherapy.ca/about_eswt.htm`, 2010.

[5] M. J. Berger and P. Colella. Adaptive mesh refinement for hyperbolic partial differential equations. *Journal of Computational Physics*, 53:484–512, 1984.

[6] M. J. Berger and R. J. LeVeque. Adaptive mesh refinement using wave-propagation algorithms for hyperbolic systems. *SIAM J. Numer. Anal.*, 35:2298–2316, 1998.

[7] R. Biedermann, A. Martin, G. Handle, T. Auckenthaler, C. Bach, and M. Krismer. Extracorporeal shock waves in the treatment of nonunions. *Journal of Trauma*, 54(5):936–42, 2003.

[8] L.V. Bossche and G. Vanderstraeten. Heterotopic ossification: A review. *Journal of Rehabilitation Medicine*, 37:129–136, 2005.

[9] C.-J.Wang, H.-S. Chen, C.-E. Chen, and K. Yang. Treatment of nonunions of long bone fractures with shock waves. *Clinical Orthopaedics and Related Research*, 387:95–101, 2001.

[10] D. Calhoun. `http://www.amath.washington.edu/~calhoun/ChomboClaw`, 2004.

[11] M. Castro, J.M. Gallardo-Molina, J.A. Lopez-Garcia, A. Pardo, and C. Pares. Finite volume methods for nonconservative hyperbolic systems: Application to shallow flows. *Communications to SIMAI Conference*, 1, 2006.

[12] M. Castro, P. LeFloch, M. Munoz-Ruiz, and C. Pares. Why many theories of shock waves are necessary: Convergence error in formally path-consistent schemes. *Journal of Computational Physics*, 227, 2008.

[13] R.P. Ching and M. Ganter. Personal communication, 2007.

[14] T. Christopher. Modeling the Dornier HM3 lithotripter. *Journal of the Acoustical Society of America*, 96(5):3088–3095, 1994.

[15] R.O. Cleveland and J. McAteer. *Physics of Shock Wave Lithotripsy*, chapter 38. Quality Medical Publishing, 2007.

[16] R.O. Cleveland and O. Sapozhnikov. Modeling elastic wave propagation in kidney stones with application to shock wave lithotripsy. *Journal of the Acoustical Society of America*, 118(4):2667–2676, 2005.

[17] Gary Cloud. *Optical Methods of Engineering Analysis*. Cambridge University Press, 1995.

[18] R. H. Cole. *Underwater Explosions*. Princeton University Press, 1948.

[19] P. Colella. Personal communication, 2009.

[20] A.J. Coleman, J. Saunders, R. Preston, and D. Bacon. Pressure waveforms generated by a Dornier extra-corporeal shock-wave lithotripter. *Ultrasound in Medicine and Biology*, 13:651–657, 1987.

[21] R. Courant and R.O. Friedrichs. *Supersonic Flow and Shock Waves*. Springer-Verlag, 1948.

[22] W.Y. Crutchfield and M. Welcome. Object-oriented implementation of adaptive mesh refinement algorithms. *Scientific Programming*, 2(4):145–156, 1993.

[23] J.W. Dally and W.F. Riley. *Experimental Stress Analysis*. McGraw-Hill, New York, 1991.

[24] K. Deisseroth and H. Hogan. Three dimensional modeling and analysis of haversian systems in compact bone tissue. In *Biomedical Engineering Conference*, 1995.

[25] M. Delius. Medical applications and bioeffects of extracorporeal shock waves. *Shock Waves*, 4(2), 1994.

[26] D.E. Erb and J.T. Povlishock. Axonal damage in severe traumatic brain injury: an experimental study in a cat. *Acta Neuropathologica*, 76(4):347–358, 1988.

[27] R.J. LeVeque et. al. `http://www.clawpack.org`, 2006.

[28] F. Gaynor Evans. *Mechanical Properties of Bone*. Charles C. Thomas, 1973.

[29] K.M. Fagnan. Code for ESWT examples, 2010.

[30] K.M. Fagnan, R.J. LeVeque, T.J. Matula, and B. MacConaghy. High-resolution finite volume methods for extracorporeal shock wave therapy. In Sylvie Benzoni-Gavage and Denis Serre, editors, *Hyperbolic Problems: Theory, Numerics, Applications*, pages 503–510. Springer, 2006.

[31] J. Freund, T. Colonius, and A. Evan. A cumulative shear mechanism for tissue damage initiation in shock-wave lithotripsy. *Ultrasound in Medicine and Biology*, 33:1495–1503, 2007.

[32] H.M. Frost. *Bone Remodeling Dynamics*. Charles C. Thomas, 1963.

[33] Y.C. Fung. *Biomechanics: Mechanical Properties of Living Tissues*. Springer, 1993.

[34] J. Ghajar. Traumatic brain injury. *The Lancet*, 356:923–929, 2000.

[35] S.K. Godunov. A difference method for numerical calculation of discontinuous solutions of the equations of hydrodynamics. *Mat. Sb. (N.S.)*, 47(89):271–306, 1959.

[36] A.B. Gojani, K. Ohtani, K. Takayama, and S.H.R. Hosseini. Shock Hugoniot and equations of states of water, castor oil, and aqueous solutions of sodium chloride, sucrose and gelatin. *Shock Waves*, Online 2009.

[37] The HDF5 Group. `http://www.hdfgroup.org/HDF5/`, Version 1.6.10.

[38] Y.M. Haddad. *Viscoelasticity of Engineering Materials*. Chapman and Hall, 1995.

[39] M. Hamilton. Transient axial solution for the reflection of a spherical wave from a concave ellipsoidal mirror. *Journal of the Acoustical Society of America*, 93(3):1256–1266, 1993.

[40] J.G. Harris. *LInear Elastic Waves*. Cambridge University Press, 2001.

[41] M.V. Hillsley and J.A. Frangos. Review: Bone tissue engineering: The role of interstitial fluid flow. *Biotechnology and Bioengineering*, 43:573–581, 1994.

[42] R. Hoebrecht. A finite volume approach to modeling injury mechanisms of blast-induced traumatic brain injury. Master's thesis, University of Washington, 2009.

[43] M.J. Ivings, D.M. Causon, and E.F. Toro. On Riemann solvers for compressible liquids. *International Journal for Numerical Methods in Fluids*, 28:395–418, 1998.

[44] H.T. Jessop and F.C. Harris. *Photoelasticity: Principals and Methods*. Dover, New York, 1949.

[45] Robert A. Riehle Jr. *Principles of Extracorporeal Shock Wave Lithotripsy*. Church Livingstone, 1987.

[46] M. Käser, M. Dumbser, J. De la Puente, and H. Igel. An arbitrary high order discontinuous Galerkin method for elastic waves on unstructured meshes III: viscoelastic attenuation. *Geophysical Journal International*, 142, 2000.

[47] K.Kerbl, J.Rehman, J. Landman, D. Lee, C. Sundaram, and R. V. Clayman. Current management of urolithiasis: Progress or regress? *Journal of Endourology*, 16(2):281–288, 2002.

[48] Applied Numerical Algorithms Group (ANAG) Lawrence Berkeley National Laboratory. `https://seesar.lbl.gov/ANAG/chombo/`, 2009.

[49] VisIt Lawrence Livermore Natural Laboratory. `http://wci.llnl.gov/codes/visit/`, 2000.

[50] P. LeFloch. Shock waves for nonlinear hyperbolic systems in nonconservative form. *Institute for Math. and its Appl., Minneapolis, preprint*, 1989.

[51] Randall. J. LeVeque. *Finite Volume Methods for Hyperbolic Problems*. Cambridge University Press, 2002.

[52] R.J. LeVeque. Finite-volume methods for non-linear elasticity in heterogeneous media. *International Journal for Numerical Methods in Fluids*, 40(1-2):93–104, 2001.

[53] J.E. LIngeman, J.A. McAteer, S.A. Kempson, and A.P. Evan. Bioeffects of extracorporeal shock-wave lithotripsy. *Journal of Endourology*, 1(2):89–98, 1987.

[54] H.-M. Liu, C.-M. Chao, J.-Y. Hsieh, and C.-C. Jiang. Humeral head osteonecrosis after extracorporeal shock-wave treatment for rotator cuff tendinopathy. *The Journal of Bone and Joint Surgery*, 88:1353–1356, 2006.

[55] R. Bruce Martin, David B. Burr, and Neil A. Sharkey. *Skeletal Tissue Mechanics*. Springer, 1998.

[56] T.J. Matula, P.R. Hilmo, and M.R. Bailey. A suppressor to prevent direct wave-induced cavitation in shock wave therapy devices. *Journal of the Acoustical Society of America*, 118(1):178–185, 2005.

[57] M.Chang. Personal communication, 2009.

[58] G. Mouzopoulos, M. Stamatakos, D. Mouzopoulos, and M. Tzurbakis. Extracorporeal shock wave treatment for shoulder calcific tendonitis: a systematic review. *Skeletal Radiology*, 36(9):803–811, 2008.

[59] C.D. Munz. On Godunov-type schemes for Lagrangian gas dynamics. *SIAM Journal on Numerical Analysis*, 31(2):17–42, 1994.

[60] M. Nakahara, K. Nagayama, and Y. Mori. Shockwave dynamics of high pressure pulse in water and other biological materials based on Hugoniot data. *Japanese Journal of Applied Physics*, 47:3510–3517, 2008.

[61] M. Nakahara, K. Nagayama, and Y. Mori. Shockwave dynamics of high pressure pulse in water and other biological materials based on Hugoniot data. *Japanese Journal of Applied Physics*, 47, 2008.

[62] T. Nishida, H. Shimokawa, K. Oi, H. Tatewaki, T. Uwatoku, K. Abe, Y. Matsumoto, N. Kajihara, M. Eto, T. Matsuda, H. Yasui, A. Takeshita, and K. Sunagawa. Extracorporeal cardiac shock wave therapy markedly ameliorates ischemia-induced myocardial dysfunction in pigs in vivo. *Circulation*, 110:3055–3061, 2004.

[63] J.A. Ogden, R. Alvarez, R. Levitt, L.G. Cross, and M. Marlow. Shock wave therapy for chronic proximal plantar fasciitis. *Clinical Orthopaedics and Related Research*, 387:47–59, 2001.

[64] J.A. Ogden and R.R. Alvarez. Extracorporeal shock wave therapy in orthopaedics. In *Written symposium*. Lippincott, Williams and Wilkins, 2001.

[65] J.A. Ogden, A. Toth-Kischkat, and R. Schultheiss. Principles of shock wave therapy. *Clinical Orthopaedics and Related Research*, 387:8–17, 2001.

[66] P.K. Rastogi. *Photomechanics (Topics in Applied Physics)*. Springer, 2000.

[67] P.L. Roe. Approximate Riemann solvers, parameter vectors and difference schemes. *Journal of Computational Physics*, 135(2):250–258, 1997.

[68] J.D. Rompe, C. Hopf, K. Kullmer, J. Heine, and R. Burger. Analgesic effect of extracorporeal shock-wave therapy on chronic tennis elbow. *Journal of Bone and Joint Surgery, British Volume*, 78-B:233, 1996.

[69] P.L. Sachdev. *Shock Waves and Explosions*. Chapman and Hall/CRC, 2004.

[70] T. Saito, M. Marumoto, H. Yamashita, S.H.R. Hosseini, A. Nakagawa, T. Hirano, and K. Takayama. Experimental and numerical studies of underwater shock wave attenuation. *Shock Waves*, 13:139–148, 2003.

[71] O. Sapozhnikov, M. Bailey, and R.O. Cleveland. The role of shear and longitudinal waves in the kidney stone comminution by a lithotripter shock pulse (a). *Journal of the Acoustical Society of America*, 115:2562–2562, 2004.

[72] O. Sapozhnikov, A.D. Maxwell, B. MacConaghy, and M. Bailey. A mechanistic analysis of stone fracture in lithotripsy. *Journal of the Acoustical Society of America*, 121(2):1190–1202, 2007.

[73] L.I. Sedov. *Similarity and dimensional methods in mechanics*. CRC Press, 1993.

[74] A. Sems, R. Dimeff, and J. P. Iannotti. Extracorporeal shock wave therapy in the treatment of chronic tendinopathies. *Journal of the American Academy of Orthopaedic Surgeons*, 14(4):195–204, 2006.

[75] M. Shashkov and B. Wendroff. A composite scheme for gas dynamics in Lagrangian coordinates. *Journal of Computational Physics*, 150:502–517, 1999.

[76] J.V. Subbarao and S.J. Garrison. Heterotopic ossification: diagnosis and management, current concepts and controversies. *Journal of Spinal Cord Medicine*, 22(4):273–83, 1999.

[77] M. Tanguay. *Computation of bubbly cavitating flow in shock wave lithotripsy*. PhD thesis, California Institute of Technology, 2004.

[78] G.I. Taylor. The formation of a blast wave by a very intense explosion. I. Theoretical discussion. *Proceedings of the Royal Society of London. Series A, Mathematical and Physical Sciences*, 201(1065):159–174, 1950.

[79] Philip. A. Thompson. *Compressible Fluid Dynamics*. McGraw-Hill, 1972.

[80] C.-J. Wang, F.-S. Wang, J.-Y. Ko, H.-Y. Huang, C.-J. Chen, Y.-C. Sun, and Y.-J. Yang. Extracorporeal shockwave therapy shows regeneration in hip necrosis. *Rheumatology*, 47(4):542–546, 2008.

[81] C.-J. Wang, F.-S. Wang, K.D. Yang, L.-H. Weng, C.-C. Hsu, C.-S. Huang, and L.-C. Yang. Shock wave therapy induces neovascularlization at the tendon-bone junction. A study in rabbits. *Journal of Orthopaedic Research*, 21:984–989, 2006.

[82] Wikipedia. Photoelasticity. http://en.wikipedia.org/wiki/Photoelasticity, 2010.

[83] X. Xi and P. Zhong. Dynamic photoelastic study of the transient stress field in solids during shock wave lithotripsy. *Journal of the Acoustical Society of America*, 109(3):1226–1239, 2001.